PLEASE NOTE

The negative microfilm copy of this dissertation was prepared and inspected by the school granting the degree. We are using this film without further inspection or change. If there are any questions about the content, please write directly to the school.

INFORMATION TO USERS

The following explanation of techniques is provided to help clarify markings or notations which may appear on this reproduction.

1. The sign or "target" for pages apparently lacking from the document photographed is "Missing Page(s)". If it was possible to obtain the missing page(s) or section, they are spliced into the film along with adjacent pages. This may have necessitated cutting through an image and duplicating adjacent pages to assure complete continuity.

2. When an image on the film is obliterated with a round black mark, it is an indication of either blurred copy because of movement during exposure, duplicate copy, or copyrighted materials that should not have been filmed. For blurred pages, a good image of the page can be found in the adjacent frame. If copyrighted materials were deleted, a target note will appear listing the pages in the adjacent frame.

3. When a map, drawing or chart, etc., is part of the material being photographed, a definite method of "sectioning" the material has been followed. It is customary to begin filming at the upper left hand corner of a large sheet and to continue from left to right in equal sections with small overlaps. If necessary, sectioning is continued again—beginning below the first row and continuing on until complete.

4. For illustrations that cannot be satisfactorily reproduced by xerographic means, photographic prints can be purchased at additional cost and inserted into your xerographic copy. These prints are available upon request from the Dissertations Customer Services Department.

5. Some pages in any document may have indistinct print. In all cases the best available copy has been filmed.

University
Microfilms
International

300 N. Zeeb Road
Ann Arbor, MI 48106

Herzog, Siegfried

THE LARGE SCALE STRUCTURE IN THE NEAR-WALL REGION OF
TURBULENT PIPE FLOW

Cornell University   PH.D.   1986

University
Microfilms
International. 300 N. Zeeb Road, Ann Arbor, MI 48106

THE LARGE SCALE STRUCTURE IN THE NEAR-WALL REGION
OF TURBULENT PIPE FLOW

A Thesis

Presented to the Faculty of the Graduate School

of Cornell University

in Partial Fulfillment of the Requirements for the Degree of

Doctor of Philosophy

by

Siegfried Herzog

January 1986

BIOGRAPHICAL SKETCH

The author was born in 1944 in Hamburg, West Germany. He finished school in 1960 and concluded an apprenticeship as general machinist in 1963. In the same year S.Herzog obtained his high-school diploma and started in 1967 at the Technische Hochschule in Munich, West Germany obtaining his Diplom-Ingenieur in 1972. In 1975 S.Herzog enrolled as a graduate student in The Pennsylvania State University and transferred to Cornell University in 1978.

to my dear wife Jane,

my parents,

and my friends Tom and Lavonne

ACKNOWLEDGEMENTS

the good offices of Gary T. Chapman.

4) The NASA-Langley Research Center and

5) The U.S. Air Force Office of Scientific Research,

Aerospace Science Directorate, Michael Francis Program Manager.

TABLE OF CONTENTS

LIST OF TABLES

-viii-

LIST OF FIGURES

-xi-

Chapter I

INTRODUCTION

Beginning in the middle 1940's, experiments were performed that
brought to light the presence of organization and structure in many
turbulent flows. These experiments culminated in the work of Kline
et al. (1967) who observed a recurring coherent pattern of events in
the near-wall region of a turbulent channel flow. Visual studies
revealed the presence of surprisingly well-organized motions with
the now classical elongated, low-speed streaks in the viscous
sublayer. These streaks were seen to interact with the outer portion
of the flow through a process of gradual lift-up, sudden oscillation
followed by a break-up into chaotic motion being ejected into the
outer flow region. They referred to this three stage process as
bursting.

The work of Kline et al. marked not only the onset of intensive
research into quasi-deterministic structures in turbulent flows but
lead to a renewed emphasis on visual techniques, which proved to be
not only powerful but sometimes lead to misinterpretation. With
their combined dye and hydrogen-bubble visualization plus hot-wire
measurements they were able to estimate various scales of motion
associated with the streaks and bursts. They obtained an average
spanwise spacing of the randomly occuring low-speed streaks of about

100 wall-units and observed that the streaks initially drift slowly away from the wall to about $y^+ = 10$. Here the streaks began to oscillate which terminated in an uprupt break-up in the region of $10 < y^+ < 30$. After the break-up the remnants of the streaks continued to stretch and to move outwards.

Corino and Brodkey (1969) essentially confirmed these findings but noted that the break-up was preceeded by the formation of an intense shear-layer between the low-speed region close to the wall and the high-speed fluid entering from the upstream outer flow region. They could not find any evidence though that the developing oscillation lead, by some instability mechanism, to the observed ejection process. Rather, most often they observed that the interaction between low-speed and high-speed fluid occured only after the ejection had begun. Corino and Brodkey added to the sequence of bursting a fourth major event, called the sweep, which encompasses the entry of a mass of fluid from upstream moving almost parallel to the wall with a velocity profile close to that of the mean velocity. Investigating a range of Reynolds numbers of their pipe flow from 5300 to 52000 Corino and Brodkey found that the frequency of occurences increased significantly with Reynolds number and that it should be normalized with inner variables.

Rao et al. (1971) measured the bursting frequency in the near-wall region of turbulent boundary layers over a wider range of Reynolds numbers and incorporated the results of other authors. They found that the mean burst period scales with outer

variables (free stream velocity and boundary layer thickness) and that the dimensionless time between bursts is given by:

$$\frac{U_\infty T}{\delta} = 6$$

The inner layer is seen by them as the place of turbulent energy production, but interacting strongly with the outer layer.

The view that the bursting period scales with outer variables was subsequently supported by a variety of investigators such as Kim et al. (1971), Laufer and Narayanan (1971), Sabot and Comte-Bellot (1976), although some investigator still feel that a scaling with inner variables is more appropriate, Hussain (1983).

Equally controversial opinions can be found concerning the observed slow-speed streaks and their connection with streamwise and spanwise vorticity features.

Brodkey (1978), in summarizing and interpreting the results of past studies conducted at Ohio State University, states that "the streamwise and transverse vortical motions in the wall region appear to be the result of the shear zone at the front between the wall-ward moving high-speed fluid and the trapped, but outflowing, low-speed fluid."

On the other side, Wallace (1982) explains the entire sequence of bursting governed by vorticity. Transverse lines of vorticity diffuse away from the wall and are randomly kinked by small scale pressure fluctuations. Kinked loops pointing upstream will move back to the wall and diffuse while those pointing downstream will rise

because of their induced velocities. As they rise, their legs will intensify due to vortex stretching and increase their induced upward velocity. These hair-pin like vortices are responsible for the large local momentum transport and create high shear layers. In addition these vortices are responsible for much of the large pressure variations at the wall giving rise to new contorted vortex lines entering the flow.

Smith (1984) also sees these hair-pin vortices as a dominant structure in the wall region of turbulent boundary layers, but explains their generation very differently. The interface between low-speed streaks and high-speed fluid gives rise to a three-dimensional inflectional profile. The breakdown of this inflectional profile is suggested to result in a series of vortex roll-ups leading to the formation of a number of hairpins (between two and five). As these hairpin loops are convected away from the surface, vortex stretching in the streamwise direction occurs intensifying the vorticity within the legs of the hairpins which reinforces the slow-speed streak. As the low-speed streak is lifted up by the counter-rotating legs the cycle renews itself through interaction with the outer fluid. Also, parts of these vortices may sometimes survive the break-up and participate in the rejuvenation of remnants of the previous low-speed streak or development of a new streak.

There are at least two different reasons which can be given for such a variety of opinions even after almost 40 years of intense

research effort into the structures of the near-wall region of turbulent flows. Firstly, the dominant structures are imbedded into incoherent or less coherent background (velocity fluctuations which are not participating in the organization) which is of equal intensity to the structures themselves. The structures furthermore undergo significant temporal development which scatters widely about some average development. Secondly, despite much progress in the field of flow visualization and combination therof with hot-wire anemometry and recently in combination with image processing the individual experiments still yield only partial information about the 3-D flow field. This leaves open a wide margin for individual interpretation leading to the wrong conclusions based on correct observations and measurements.

In contrast to that stands a method first proposed by Lumley (1976), which has been applied already by a small number of researchers: Payne (1966), Bakewell (1967), Lemmerman (1976) and Moin (1984). Its major draw back is the vast amount of experimental data which has to be supplied. The method is based on looking at a turbulent flow field as a statistical realization of a random vector field with a possibly present dominant structure. One way to test for such a suspected structure, described in terms of its velocity field in space and time, is to correlate the proposed structure in the mean square sense with an ensemble of realizations of the flow field. Maximizing this correlation leads to a well-defined eigenvalue problem in terms of a linear integral equation involving

the symmetric cross-correlation tensor of the velocity field as kernel. Solutions to this equation are governed by the theorems of the classical Hilbert-Schmidt theory. These solutions provide a representation of each realization of the flow field in terms of orthogonal eigenfunctions of its correlation tensor and allow an unambiguious determination of the contributions of the individual eigenmodes to the kinetic energies and Reynolds stresses. A kinematic description of the dominant eigenmode in physical space is hampered by the fact that Lumley's orthogonal decomposition reduces to the classical Fourier-decomposition for the homogeneous coordinates. Although the magnitude of the constituent Fourier-components can be determined using the shot-noise decomposition of Rice (1944), their relative phase cannot be determined from second order statistics.

Theoretical aspects of Lumley's orthogonal decomposition and the recovery of phase-information based on the requirements of real-valuedness and symmetry of the dominant structures and from higher order statistics are discussed in chapter IV of this study.

The experimental part of this study consisted of measuring the velocity field in the near-wall region of a turbulent pipe flow from which we determined the complete space-time cross-correlation tensor.

Measurements were conducted in the boundary layer research facility in the Applied Research Laboratory at The Pennsylvania State University. The facility utilizes the high viscosity of

glycerine to enhance the physical size of the near-wall region so that the measurements could be conducted with conventional hot-film anemometry. Details of the experiments and data aquisition are described in chapter II. The data reduction process leading to the recovery of the velocity time series is detailed in chapter III. Single point statistics of the flow field under investigation and the results pertaining to the application of the orthogonal decomposition are brought in chapter V. A comparison of the extracted typcial eddy with information from the relevant literature is included in chapter VI.

Chapter II

EXPERIMENTAL FACILITY AND METHOD

2.1 GENERAL DESCRIPTION

In most ordinarily occurring flow situations the viscous boundary
layer region is confined to such a small physical size that detailed
measurements are extremly difficult to perform. For turbulent pipe
flow the viscous length can be expressed in terms of the pipe
diameter D and the Reynolds number Re.

$$L_\nu = 5.03 \; D \; Re^{-7/8} \tag{2.1}$$

with

$$Re = \frac{U_m \; D}{\nu} \tag{2.2}$$

Because the Reynolds number has a lower bound given by the condition
to obtain fully developed turbulent flow the viscous length can be
influenced significantly only by choosing a large pipe diameter. But
this means having the mean velocity at a low value which leads to
severe measurement problems in hotwire anemometry due to natural
convection effects. A working fluid with a high kinematic viscosity
has the desired effect of allowing a low Reynolds number, relatively
high mean velocity and large pipe diameter to obtain a large viscous
length. Fluids with high kinematic viscosity fall into one of three

distinct groups: firstly, the group of gases with low molecular weight (hydrogen or helium), secondly ordinary gases at low pressures and thirdly high molecular-weight liquids like oils, etc.

For our experiments we obtained a viscous length of 0.538 mm by using almost pure glycerine as working fluid. The experimental facility used was the same as described by Bakewell (1967); some important characteristics are summerized in Table (1) and a schematic view is given in Figure (1).

The closed-circuit facility consisted of a 100 hp centrifugal pump, a settling section with a built-in honeycomb followed by a 16 to 1 contraction to the test-pipe diameter of D=0.285 m. The test facility contained some 1800 gallons of glycerine which could be emptied into storage tanks which were covered by swimming floats to reduce entrapment of air.

The test section was located twenty-five diameters downstream of the contraction which was equipped with a serrated trip-ring to fix the location of transition to a turbulent wall boundary layer.

From pressure measurements along the pipe axis we concluded that this boundary layer then grew rapidly into the core region of the pipe, see Figure (2). The linearity of the pressure drop over seventeen pipe diameters upstream of the measurement section convinced us us that at least in the wall region of the measurement section the flow could be considered fully turbulent. Since we were interested only in the near-wall region we may expect higher order moments also to have come to equilibrium (Comte-Bellot 1963).

A constantly occuring problem with the facility which subsequently caused us much work in sifting through all obtained velocity time-series was the entrapment of air. Unfortunately new air was introduced into the system when installing new probes, when replacing glycerine lost through the pump bearings, and each day when introducing the probes into the test section.

Due to the high viscosity of glycerine air bubbles rise slowly and we needed hours of running at higher temperatures to reduce the air bubble content to an acceptable level. But still, particularly at sensor positions furthest away from the wall, air bubbles frequently got stuck on the sensor, enlarged rapidly and sometimes stayed for minutes. Large bubbles could be detected easily because of the reduction of heat transfer from sensor to fluid and a corresponding drop in the mean voltage of the anemometers. But many smaller events escaped undetected until after digitization of the data.

2.2 GLYCERINE AS WORKING FLUID

Table (2) summarizes the physical properties of glycerine. Except for the viscosity, all properties change only insignificantly with temperature. In addition to the strong temperature dependency of the viscosity of glycerine, Figure (3), its hygroscopic character has to be mentioned, because of capture of moisture from the ambient air.

Like many liquids, the viscosity-temperature dependency can be empirically described by a simple exponential law. From independent

measurements of density, kinematic and dynamic viscosity at different temperatures we found:

$$\nu = -0.7 + \exp\left(\left[\frac{T+273}{462.319}\right]^{-4.107793}\right) \qquad (2.3)$$

for ν in Centi-Stokes and T in degree Celsius. The change of ν with temperature is then

$$\frac{1}{\nu}\frac{d\nu}{dT} = -0.0691 \; 1/°C \qquad (2.4)$$

at 35°C.

Because the viscosity directly influences the size of the viscous sublayer a temperature control is necessary. The facility had to be run at a constant temperature during the course of the measurements which was in general different from the ambient temperature. To avoid temperature gradients near the wall, the entire test facility, particularly upstream of the measurement section, was insulated. This in turn necessitated the installation of a by-pass loop with heat-exchanger to compensate for most of the 100 hp constantly introduced into the system by the driving pump. The cooled glycerine was reintroduced into the tunnel just upstream of the pump where it mixed thoroughly with the warm glycerine.

2.3 VELOCITY SENSORS

2.3.1 General Description

In order to evaluate the complete space-time cross-correlation
tensor as needed for Lumley's orthogonal decomposition scheme, it is
sufficient to measure just two velocity components at two different
points in the flow simultaneously and then perform the measurements
for different locations of the two probes over and over again.

We measured the streamwise and circumferential velocity component
with two commercially available, single-ended hot-splitfilm sensors
simultaneously at two different locations in the test-section of the
facility. The sensors consisted of a cylindrical, single-ended
quartz body with its axis oriented roughly perpendicular to the pipe
wall. Each sensor carried two separate films consisting of two
patches. Each patch covered about 1/4 of the circumference of a
cylindrical carrier body. For each film the electric current flowed
from the direction of the sensor holder through one patch towards
the tip of the sensor, through a gold-plated connector to the other
patch through which the electric current then returned back towards
the sensor holder. Each of the two hot-films was operated by a
single constant-temperature anemometer unit. A cross-sectional view
of the quartz body and hot-film patches is given in Figure (4) and
some physical data are collected in Table (3).

The size of the sensing element is about 1/2 of the viscous
length perpendicular to and 1/4 parallel to the wall. No attempts
were made to compensate for any errors associated with the spatial

averaging due to the finite size of the probes. Similarly, we did not
try to compensate for any wall-sensor interference concerning heat
flux from sensor to wall nor any blockage effects due to the mere
presence of the sensor. In our initial single-sensor investigations
concerning single point moments and spectra we could not find any
reason to do otherwise.

2.3.2 Steady-State Response of Hot-Film Sensors

Several potential problems have to be addressed to insure proper
working conditions for the sensors.

Since glycerine is electrically non-conductive, uncoated hot-film
sensors have to be used. Using coated sensors in an electrically
non-conductive medium may cause electro-static built-up. On the
other hand, glycerine is slightly aggressive chemically to most
metals particularly in the presence of air. We observed products of
chemical reaction with aluminum, brass and steel. Immediate,
thorough cleaning of the sensors after taking them out of the
glycerine held the problems to an acceptable level.

For measurements within the viscous sublayer with its linear mean
velocity profile, the probe Reynolds number based on sensor diameter
and local mean velocity reads:

$$Re_s = \frac{D_s \, y^+}{L_\nu} \tag{2.5}$$

with y^+ being the wall distance in terms of inner variables. For $y^+\approx1.25$, our closest wall distance, we obtain

$$Re_s = 0.34 \qquad (2.6)$$

which grows to about $Re_s\approx5$ at the measurement point furthest away from the wall. In this Reynolds number range no vortex shedding is expected and none was encountered.

Because no calibration data for hot-splitfilm probes in glycerine were available we built a small calibration station, inserting the probe into stationary, laminar pipe flow. Figure (5) shows the total energy output and Figure (6) the differential energy output of the two anemometer units as function of angle of attack, see Figure (4), with the effective velocity as parameter. Energy output is here defined as the squared voltage output of each of the involved anemometer units. Different definitions which mostly take into account the mismatch between the two films and scaling parameters did not change the basic characteristics of the observed dependencies.

Two main features are immediately apparent. First, the angular sensitivity is strongly dependent on the effective velocity which differs quite significantly from similar calibration data obtained from measurements in air and water, Olin (1970) and Blinco (1973). We were not able to derive any simple scaling law for this behavior and representing the ratio of voltage output instead of their difference did not bring about any improvement. Second, both their

differential and the total energy output show non-linearities which seem to be systematic in occurrence. We attribute these to the high Prandtl number of glycerine and geometric imperfections of the sensors. The high Prandtl number of glycerine, see Table (2), causes the temperature field around the sensor to behave like a thin thermal boundary layer. The heat transfer from the films to the fluid is thus very much influenced by local imperfections, particularly the axial cuts through the quartz carrier body made to separate the individual film patches, see Figure (4).

The best way to display the calibration characteristics we found is one like Figure (7), with curves of constant effective velocity and curves of constant angle of attack in the V_1^2-V_2^2 plane.

Generally speaking we found operating a hot-splitfilm sensor extremely difficult. The adjustment of the operational resistances of the two anemometer units with respect to each other was a very time consuming task. A fast method which we employed, giving nice symmetric sensor behavior, is to try to keep the ratio of the two voltages as independent of effective velocity as possible.

We chose to operate the films at an overheat-ratio of about 1.08, which corresponded to a sensor-fluid temperature difference of about 35°C. Raising the overheat ratio further increased the spectral density at higher frequencies only insignificantly, but led to much shorter life span of the sensors. This latter point was somewhat crucial because the life span was limited mostly by slowly progressing sensor burnout. This always started at the rear

stagnation point of the sensor and occurred even at unacceptably low overheat ratios. The above mentioned thermal boundary layer around the sensor, due to the high Prandtl number of glycerine, was probably responsible for this.

2.3.3 Frequency Response of Hot-Film Sensors

In the field of anemometry, the term constant-temperature anemometer (CTA) can be seriously misleading because the very function of such an anemometer unit is only to hold the overall electrical resistance of the hot-film or wire constant, leaving the actual temperature distribution subject to the local, instantaneous heat fluxes from the film to surrounding fluid and into the substrate body. Although this is generally known, detailed investigations of probe frequency response are scarce.

In order to evaluate the frequency response of our probes we developed a computer code to simulate the thermophysical and electrical properties of a hot-splitfilm sensor.

The starting point of our interest was a simple thought-model. Two electric resistors ($i=1,2$), the resistances of which vary with temperature

$$R_i = R_0 + S\,T_i \qquad (2.7)$$

are connected electrically parallel and operated upon by a single CTA-unit holding the overall resistance constant. For each resistor the internally generated heat is balanced by losses to its

surrounding with a certain heat-transfer coefficient H_i and temperature difference T_i. For overheat-ratios close to one we obtain in first approximation

$$H_i \ T_i \ = \ constant \tag{2.8}$$

Tranferred to our cylindrical hot-film sensors this means that in areas of low heat-transfer coefficient, (for example at the rear stagnation point), the film temperature will be high and vice versa. We believe this is the reason why our sensors always started to show first signs of burn-out at the rear stagnation point.

The heat-transfer coefficient distribution around a heated cylinder at low Reynolds number flow is instantaneously varying with flow velocity and angle of attack. The poor heat-conductivity of our working fluid makes it likely that the heat-losses from the film to the fluid are of equal order as those from the film into the substrate body. Thermal events inside the substrate body have a characteristic frequency of $\alpha/D_s^2 = 36$ Hz. More detailed investigation were in order.

On the basis of numerical calculations of the flow field around circular cylinders at low Reynolds numbers one can develop easily corresponding, simple heat-transfer models for high Prandtl number fluids.

In a small computer program we represented the heat-transfer within the substrate body by a simple lumped-node model, neglecting any axial effects. The anemometer units were reduced to black boxes,

the function of which was to hold the overall resistance of their respective films constant.

With the physical properties of the sensor according to Table (3), cross-sectional view of sensor see Figure (4), we obtained a circumferential temperature distribution as shown in Figure (8). The two distributions shown are stationary solutions obtained at angle of attack equal to zero for Renolds numbers of Re=1 and Re=3. The operational electric resistance of the two films were selected to give a nominal temperature difference, film to fluid of 40°C.

As expected, the heat fluxes inside the substrate body were of the same order as those from the film to the fluid, damping considerably the temperature extrema at the stagnation points. Associated with variations in the instantaneous temperature distribution is a thermal inertia. The transient response of our sensor-model to step functions in external flow conditions is an exponentially decaying approach to the new steady state with an associated time-constant of approximately

$$T^{-1} = \frac{50\,\alpha}{D_s^2} = 1800 \text{ Hz} \tag{2.9}$$

for a step in angle of attack and

$$T^{-1} = \frac{30\,\alpha}{D_s^2} = 1080 \text{ Hz} \tag{2.10}$$

for a step in Reynolds number.

Expected frequencies relevant to large scale structure investigation range from zero to about 200-300 Hz for our experiment, see Bakewell (1967). Hence the frequency response of the selected sensors was judged to be adequate.

2.4 MEASUREMENT SECTION OF FACILITY

The measurement section of the facility, located about twenty-five times the pipe diameter downstream of the trip-ring, consisted of a T-section in the straight pipe with the glycerine flowing through the 'horizontal' crossbar of the T. The 'vertical' stem of the T-section was closed off by a gate during warm-up period when the entire facility was brought up to operating temperature. The T-stem enclosed a cylindrical body tightly which, after opening the gate, could be moved inward until its curved proximal surface was flush with the inside wall of the pipe. At this position the cyclindrical body was then solidly arrested and measurements could be taken with the two probes protruding through the curved proximal surface of the cylinder.

We employed two different types of probe holders. The first was a straight and needle-like probe holder, projecting into the flow along a diameter of the pipe with the sensor at its very tip. Although several openings in the curved proximal surface as well as two holes well upstream of the T-section (to realize large streamwise spacings) were available for this probe, we will refer to it as the fixed probe. Its task was essentially to move its sensor

to and away from the wall. This probe was always located upstream of the second probe. In order to minimize flow disturbances which affect the downstream probe, it was kept as slender as possible and the hole through which it protruded was equipped with spring activated miniature sliding doors which always closed in on the tapered probe shaft.

The second, downstream probe, which we will refer to from now on as the moveable probe, was bent forward and then back toward the wall so that the sensor, at the very tip of this hook, was pointing towards the wall and was not affected by flow disturbances due to the double bend and probe holder shaft.

Originally this probe shaft was able to move around rather freely in the streamwise and circumferential direction because of a large square opening in the curved proximal surface of the cylinder. With it the probe shaft carried a thin plate which covered the square hole at all times. This design was abandoned because the frictional forces acting on the plate when moving it about were so large that the entire traversing mechanism for this moveable probe and the cover plate deformed elastically and made it impossible to achieve accurate probe positions.

The second, successful design consisted of replaceable plastic inserts secured in the square hole. Each carried a slit in circumferential direction at a particular downstream location so that the moveable probe could travel only in the circumferential direction and change the wall distance of the its sensor. To

minimize flow disturbances, the slit was filled with plastic foam glued to its upstream and downstream rim. The foam was then cut along the center of the slit allowing the probe shaft to move freely in the circumferential direction. With that plastic insert in place, which carried its slit in the most upstream position, we performed some preliminary measurements with the fixed probe. Then we replaced this insert with one having no slit at all. No difference in the flow field could be observed. With this design streamwise separations from 0 to 12.8 inches and circumferential from zero to three inches could be realized corresponding to a maximum of 600 and 136 times the viscous length scale, respectively. Figure (9) summarizes the positions the two probes assume with respect to each other. The homogeneity in the streamwise and homogeneity and symmetry in the circumferential direction greatly reduces the number of needed constellations. Nevertheless the entire scanning matrix contains 6*6*7*6=1512 entries. For each entry data were taken for a duration of 3 minutes which corresponds about to 7000 integral time scales of the streamwise velocity component.

As shown in Figure (9) the probe movements were executed in a cartesian frame of references. Because we measured only very close to the wall (maximum wall-distance/pipe radius = 0.151) all calculations can be performed in cartesian coordinates with one exception. When assigning coordinate values to the probe positions shown in Figure (9) to evaluate the correlation tensor as function of the circumferential coordinate we used a cylindrical coordinate

system. The need for this becomes apparent if one considers a case where one probe is near the wall, point A in Figure (9) and the other furthest away from it, point B. In cylindrical coordinates they have no circumferential spacing (maximum correlation) while in cartesian coordinates we still have non-zero spacing. The difference in counting is small in absolute value because of the wall-proximity but large enough in comparison to the width of the maximum of the correlation functions, particularly that of the circumferential velocity component.

2.5   SENSOR CALIBRATION FACILITY

At an early stage during the present project it became obvious that due to slowly progressing burn-out and leaching our sensors would loose their calibration characteristics rather rapidly and would have to be recalibrated frequently. Calibrating for change in velocity and angle of attack was a time consuming task and it was decided to do most of our measurements with uncalibrated probes. We obtained the sensor characteristics to convert anemometer output voltages back into velocities by a procedure we will refer to as Inverse Calibration. It is described in section 3.4 . To apply this method, one must know single point characteristics of the turbulence well, including higher order moments. Such a method offers itself in an experiment where the turbulence is stationary and homogeneous in two spatial directions.

To obtain these data we calibrated a sensor of the fixed probe design rather carefully in a specially designed calibration facility.

The calibration facility consisted essentially of a 25 mm diameter straight pipe in which we established laminar pipe flow. This pipe was part of a bypass-loop of the general facility with a 20 ft long feeding section ahead of the calibration pipe and a smooth transition from the 3 inch feeder pipe to the 1 inch calibration pipe. The velocity in the calibration pipe was deduced from the pressure drop in the axial direction. This pressure drop was measured at several locations and found to be linear to within measurement accuracy. In addition, we verified this method by measuring the centerline velocity with a miniature Pitot-tube and found satisfactory agreement at all velocities.

When removing the thus calibrated probe from the calibration station to install it into the measurement section, we never disconnected the probe from its anemometer unit, continously using the same probe holder and connecting leads.

2.6 DATA AQUISITION SYSTEM

Throughout our investigation we used standard DISA-equipment (55M10) as anemometer units with great satisfaction. The output signals were sent through a signal conditioner (DISA 55D26) to remove high frequency noise and the DC-component and to amplify the fluctuating component. Removal of the DC-part was done with the offset facility of the signal conditioners rather then with a high-pass filter.

The data were recorded in analog form on a Bell & Howell, VR3700B, tape-recorder, because no on-site digitization equipment was available. We used the tape-recorder in FM-mode,Wideband Group I, at a tapespeed of 3 3/4 IPS. This gave us a frequency response which was flat from DC to 2.5 KHz. Several calibrated DC-signals and sine-waves were recorded ahead of and after those experiments which served to obtain single point turbulent characteristics. This allowed us to relate output-voltage of the signal conditioner units to digital numbers in a rather simple fashion incorporating offset and gain of the recording tape-recorder, playback tape-recorder and digitization facility all at once.

Digitization of the analog signals was performed by the staff of the Data Reduction and Transcription Facility of the National Aeronautics and Space Administration, Langley Research Center. At a digitization rate of 2000 Hz all four channels were digitized simultaneously and the data stored on about 300 magnetic tapes at 1600 BPI. NASA also provided us with a program to read these tapes on the PDP 11/70 at the Department of Chemical Engineering, Cornell University.

With a special reduction program we deleted all of the unnecessary tracking information on these primary tapes, organized their data into files each of which was associated with a particular spatial constellation of the two probes, and eliminated data which were obviously in error. The resulting 125 tapes were written in a special format so that we could read them at our departmental computers, a PDP 11/34 and an IBM 4341 for further analysis.

Chapter III

DATA REDUCTION

We define data reduction as the entire process leading from digital time series representing the voltage output signals of the anemometer units to digital time series representing the corresponding velocity time series. From the latter one, moments and spectra of the velocity fluctuations are obtained.

The data reduction process involves several steps. With a computer program written in Fortran, we read the voltage time series from magnetic tapes and wrote them to disk and then back to new tapes. During the transfer to disk, we performed a quality investigation on the data and compressed the time series to keep only the lower frequencies relevant to large scale structure investigation. On the basis of the information of this quality investigation for each individual experiment we rejected either all or parts of the time series and transfered only the acceptable data to tape. During this process we lost about 25% of all the experimental data, mostly by cutting the length of each experiment. During the transfer back to tape the moments of the voltage time series were obtained. They served as input to the inverse calibration procedure for those data which were obtained with uncalibrated probes.

On these improved, compressed data we then performed the conversion to velocity space and extraction of moments and/or spectra.

3.1 QUALITY INVESTIGATION

When processing time series on the computer the data are organized into records, each containing a subset of the data. The length of these records is chosen to be about 30-40 integral time scales of the turbulent signal to facilitate the later calculation of spectral estimator. This length is the result of a compromise between two factors: for a given length of the experiment the length of each record and the number of records are inversely proportional to each other. Both, length and number of records are to be kept as large as possible, the one reducing the distortion of the obtained spectra due to the weighting function, the other reducing the expected statistical error. Storage capability of the computer was not a deciding factor in our investigation.

Choosing a record length of 30-40 integral time scales is a fairly good compromise from the above point of view. At this length one can regard the individual records as statistically independent of each other. This fact we made the basis for a major portion of our quality investigation.

As said earlier, our measurements were negatively influenced by the persistently occuring problem of suspended air bubbles in the working fluid. These often attached themselves to the sensors for an

arbitrary length of time until being swept away by a fortunate velocity fluctuation. On the digital time series this appeared then as reduction of the mean and/or RMS-value of the voltage fluctuation for one or several records. A similar effect was caused by a sump pump operating intermittently in the building and reducing, upon start-up, the line voltage in the entire experimental facility. Other high-voltage electric motors, running at low RPM, sometimes seemed to cause low frequency (<1 Hz) disturbances in our recorded signals.

If one considers the series of record means for an individual experiment as a sequence of independent random variables (each experiment consisted of 100 - 300 such records) with identical Gaussian probability distribution one can easily make probabilistic statements about the occurrence of drift, periodicity and deviation of individual records from the mean for a given sequence. If the probability of an observation to occur under the assumption of statistical indepence of the records is below a set threshold, the particular record or entire experiment was rejected.

As an example let us consider a sequence of record means, $\xi_i, i=1,N$. A drift in this sequence can be calculated by:

$$D = \frac{12}{N(N^2-1)} \sum_{i=1}^{N} (i*(\xi_i - <\xi_i>)) \qquad (3.1)$$

D will be non-zero in general. Let σ_ξ^2 be the observed variance of the sequence with respect to their linear regression and let the ξ_i

have a Gaussian probility distribution. Then the drift D given by
equation (3.1), being the weighted sum of independent Gaussian
random variables has a Gaussian distribution with a variance of

$$\sigma_D^2 = \sigma_\xi^2 \frac{4N + 2}{N(N-1)} \qquad\qquad (3.2)$$

and the probability that for example $|D| > 1.645*\sigma_D$ is only 0.1
according to standard tables and we may reject the time series if
$|D|$ is observed to be larger than this value. A similar derivation
can be made for the probability of observed periodicities in the
data. Such spectral probabilities lead then to CHI-square random
variables and their derivation is rather straight forward.

In addition to this probabilistic approach our quality assurance
program gave a variety of additional information about each sequence
of record characteristics, like the 10 records with the highest or
lowest mean or RMS-value. The probability that the records with the
3 or 4 largest values are adjacent is very small and these records
were rejected. Similarily, if a particular record carries the lowest
mean of all records on all four channels we assumed that this was
due to some non-turbulent event (line-voltage drop for example).

In addition we obtained printout about the joint probability
distribution between the two time signals of each sensor. On a few
time series we discovered amplifier clipping which had occured
somewhere in the analog recording chain.

Our basic philosophy during the quality assurance phase was that the deletion of a few improbable events from the time signals with a length of a few thousand integral time scales will not do any harm to the turbulent characteristics measured, even if some of the deleted sections were truly due to turbulent events.

3.2 COMPRESSION AND LOW-PASS FILTERING

Extracting large scale structures from turbulent measurements allows one to neglect to a certain extent the high frequency components of measured time series. Originally, our data were digitized and low-pass filtered at 2000 Hz. In Figure (10) we show as an example the power spectrum of the streamwise and lateral velocity fluctuation for frequencies up to 1000 Hz which were taken at a wall-distance of $y^+\approx20$. The spectra show the expected high anisotropy at low frequency and the convergence at smaller scales. It could be shown that the subsequent divergence at higher frequencies is entirely due to the FFT-method employed to calculate the spectra. Remember that the spectral estimator obtained via FFT-methods is:

$$S(f) = \int_{-T}^{+T} (1- \frac{|\tau|}{T}) R(\tau) \, d\tau \qquad (3.3)$$

with T=record length. The weighting function in front of the autocorrelation function not only averages over neighboring

frequencies but also shifts energy from high spectral density to low spectral density. The amount of energy shifted depends on the frequency range as well as the ratio of energy densities. The latter makes this shift occur much more drastically in the lateral than in the streamwise velocity component. On our computer we had almost unlimited memory space available and we could show that indeed the spectra of both velocity components converge at higher frequencies as record length increases.

No clear guidelines can be set as to where a high frequency cut-off should be set. On one side one likes to retain as much information as possible; on the other side a high computational efficiency is desired. We decided to set the cut-off frequency such that the energy contained at all frequencies below the cut-off was always equal to or larger than 98% of the energy of the respective full-frequency spectrum. This condition was satified for all measured autospectra for a uniform cut-off frequency of 170 Hz.

We deleted the high frequency content from our digital time series by first low-pass filtering the original time series and then retaining only every 1000/170=6th time step. Low-pass filtering is necessary to avoid aliasing at the high-frequency end of the obtained spectra. As a digital low-pass filter we employed a recursive filter of the class of trigonometric filters as advanced by Otnes (1968). In particular we chose a sine-filter with

a transfer function given by:

$$H(f) = \cfrac{1}{1 + \left[\cfrac{\sin(\pi f)}{\sin(\pi f_H)}\right]^{2P}} \qquad (3.4)$$

At a degree P=3 such a filter has a steep roll-off and its phase-shift is still linear in the low-pass region, see Figure (11) and Figure (12) respectively. Filters of higher degree loose the characteristic of linear phase-shift. In both figures f_H is the half-power or cut-off frequency.

Problems of phase-shift can be avoided with non-recursive symmetric digital filters but a decent roll-off necessitates so many calculations per time step that it would not have warranted the effort in our investigation. The above sine-filter needs only P+1=4 multiplications per original time step. It was used for all our data at the same setting of the cut-off frequency f_H. The thus obtained power spectra, after filtering and keeping only every 6th time step, looked like the original extended spectra, Figure (10), being abruptly truncated at the cut-off frequency.

3.3 CONVERSION FOR CALIBRATED SENSORS

The experimental part consisted of obtaining the voltage-outputs of the two anemometer units of a single sensor for a discrete set of effective velocities and angles of attack, as shown in Figure (7).

Generally, an analytic representation of their functional dependencies is not available and one tries to develop an analytical representation starting from first principles and continues with educated guesses. Customarily, one tries to obtain a function for the effective velocity which contains the angle of attack as a weak parameter and a function for the angle of attack which, in our case would include the effective velocity as a strong parameter. A first approximation is obtained by solving for the effective velocity assuming zero angle of attack. Then one calculates a first approximation for the angle of attack and converges iteratively towards a (hopefully) unique solution. This method is rather time consuming.

In our investigation we tried successfully another approach in finding an analytic expression representing the effective velocity and angle of attack directly as a function of the output voltages of the two driving anemomenter units, eliminating any form of iteration.

Usually one starts with King's law in finding analytic expressions for the sensor response:

$$U^{1/2} = A + B \, V_s^2 \qquad\qquad (3.5)$$

> U = effective velocity
> V_s = output voltage of anemometer unit(s)

which holds strictly only for Reynolds Numbers less than one. At higher Reynolds numbers the exponent in equation (3.5) is varied depending on the range of Reynolds numbers one wishes to represent.

For a large range in Reynolds number (in our investigation from 0.3 to 5) such variations of exponent is cumbersome at best. A novel variation of King's law is:

$$U^{1/2} = A + B \, V_s^2 + C \, (V_s^2)^6 \tag{3.6}$$

Initially the exponent of 6 of the 3rd term on the right hand side of equation (3.6) was varied and the coefficients A,B and C were determined by least-mean-square fit to experimental data. The quality of the approximation was fairly independent of the exponent in a range from 4 to 8 with a very flat optimum at 6. For a two-film sensor it is appropriate to interpret the term V_s^2 as a weighted sum of the squared voltages of the anemometer bridges:

$$V_s^2 = V_1^2 + f_s \, V_2^2 \tag{3.7}$$

For ideally matched films and anemometer units the matching factor f_s is unity. Unfortunately equation (3.6) with (3.7) does not hold accurately enough for all angles of attack when working in glycerine. The weighted difference of the squared voltage output of the anemometer units

$$V_d^2 = V_1^2 - f_d \, V_2^2 \tag{3.8}$$

is a rough indicator of the change in angle of attack.

First we determined the constants A,B,C and f_s for equation (3.6) by linear regression on all experimentally obtained calibration points for all angles of attack. We then plotted the

error between experimental data and prediction as function of V_d^2. For our circumstances the equation:

$$U^{1/2} = \frac{A + B\, V_s^2 + C\, (V_s^2)^6}{1 - D\, \dfrac{|V_d^2|}{V_s^2}} \tag{3.9}$$

was very satisfactory giving a standard deviation of 0.04 m/sec for the entire range of velocities and angle of attack as shown in Figure (7). The observed deviations between experimental data and prediction after optimizing for A, B, C, f_s and f_d were scattered randomly over the entire domain and probably were due to statistical measurement errors.

In a similar systematic way we found a representation for the angle of attack as function of the anemometer outputs. With the definition of equation (3.7) and (3.8) we obtained:

$$\theta = \frac{V_d^2}{V_s^2}\, (\, B_1 + B_2\, V_s^2 + B_3\, V_s^4 \,) \tag{3.10}$$

with an average error in prediction of 0.6 degrees for the entire domain depicted in Figure (7).

There is no solid reason why the matching factors f_s and f_d used for equation (3.9) and (3.10) to determine V_s^2 and V_d^2 should be identical and slight improvement could be achieved when optimizing for their values separately.

The results obtained with the above calibration scheme are those which are presented in this thesis as single-point turbulent characteristics.

3.4   CONVERSION FOR UNCALIBRATED SENSORS

3.4.1   Outline of Method

As explained earlier, we could not possibly conduct the majority of our velocity measurements with calibrated sensors. However, two conditions were rather fortunate in our investigation. Firstly, the experimental conditions were nominally constant throughout our investigation and secondly, the turbulent characteristics in fully developed turbulent pipe flow depend only on the wall distance. It thus seemed possible to obtain the calibration characteristics of a sensor by performing a transformation on the two voltage time series such that its 2nd and higher order moments correspond to the turbulent flow characterisitics at the wall distance of the sensor in the flow field.

We will refer to the procedure of obtaining the calibration characteristic of an uncalibrated sensor by this matching of moments as inverse calibration. We tested the quality of the procedure using measurements made with calibrated sensors and compared moments higher than those used for the inverse calibration procedure, autocorrelation functions and randomly selected section of the velocity time series. The comparison was performed for all wall-distances of concern from $y^+=1.25$ to $y^+=40$.

3.4.2 The Linear Model

Assuming for the moment that the turbulent intensities of the flow field are so small that the sensor response is linear in both hot-films, equation (3.11) will hold:

$$u(t) = \alpha_1 a(t) + \beta_1 b(t)$$

$$w(t) = \alpha_2 a(t) + \beta_2 b(t)$$

(3.11)

with t=time, u(t)=streamwise velocity , w(t)=lateral velocity, and a(t) and b(t) the voltage time series of the two hot-films of the sensor. The coefficients $\alpha_1, \beta_1, \alpha_2$ and β_2 are to be determined. From the general operating principle of the sensors we know already that:

$$\alpha_1 > 0 \qquad \beta_1 > 0 \qquad \alpha_2 \beta_2 < 0$$

(3.12)

Whether α_2 or β_2 is negative here depends only on which direction we want to count w(t) positive.

Four conditions are needed to find the coefficients of equation (3.11). Note that if a(t) and b(t) have zero mean (which can be arranged always) then u(t) and w(t) also will have zero mean. We further will assume that all desired moments, including mixed moments, of a(t) and b(t) are known. Satisfying the 2nd order velocity moments:

$$\sigma_u \ , \ \sigma_w \ , \ \rho_{uw}$$

leaves us with one degree of freedom. Leaving α_1 for the time as free parameter one can express the remaining three coefficients as function of α_1 and the second order moments of the velocity and

voltage time series. The equations connecting second order moments are quadratic in nature and can be solved for the other coefficients explicitly. Sign ambiguities are resolved by taking the inequalities (3.12) into account.

For a sensor with perfectly matched hot-films one expects α_1 to be equal to β_1 and we hence investigated this region by looking at the higher order moments of the velocities to find out which of them would give a good indication for a rule to choose a value for α_1. One would expect that higher order moments might give some indication. But surprisingly, there is little variation for a range of α_1 much larger than we would expect for even a grossly mismatched sensor. Furthermore, if one plots velocity time series obtained by inverse calibration and compares them to the original velocity time series, they match to an extraordinarily high degree regardless of choice of α_1. This was totally surprising because of the high turbulent intensities in the near-wall region ($\approx 30\%$) and the strong dependency of the angular sensitivity on the effective velocity. Lacking any hints from higher order moments as to what the best choice for α_1 might be we finally decided to impose the following condition in addition to satisfying all 2nd order moments:

$$\frac{\beta_2}{\alpha_2} = -\frac{a'}{b'} \tag{3.13}$$

with a' and b' being the standard deviations of a(t) and b(t) respectively. This choice for β_2/α_2 is based on the following

thought: Because the flow under consideration is symmetric in the w-velocity component the joint probability distribution of $u(t)$ and $w(t)$ is symmetric with respect to $w=0$ also. A linear tranformation into $a(t)-b(t)$ domain will result in a joint probability distribution which is symmetric w.r.t. the line given by

$$\alpha_2 a(t) + \beta_2 b(t) = 0 \tag{3.14}$$

On a number of time series we actually calculated the jpdf in the a-b domain and found the above suggestion well confirmed although the sensor response is certainly non-linear. Experience then showed too that the symmetry line could be found in very good approximation by equation (3.13).

3.4.3 Non-linear Model

The success of the linear model did encourage us to seek further improvements, using the linear transformation given by (3.11) with (3.13) as pre-transformation into a preferred coordinate system. Let us rewrite:

$$\eta(t) = a(t) + \delta_1 \ b(t)$$

$$\xi(t) = a(t) + \delta_2 \ b(t) \tag{3.15}$$

$$\delta_1 > 0 \qquad \delta_2 < 0$$

From experimental calibration data we know that the streamwise velocity is only in first approximation a linear function of $\eta(t)$ and we included a quadratic term, see equation (3.16).

Also, the proportionality factor from $\xi(t)$ to $w(t)$ depends on the instantaneous effective velocity which we might approximate for the correction as being proportional to $\eta(t)$. Removing means appropriately to obtain $<u(t)>$ and $<w(t)>$ equal to zero we obtain:

$$u(t) = u' \gamma_1 (\eta + \epsilon_1(\eta^2 - <\eta^2>))$$

$$w(t) = w' \gamma_2 (\xi + \epsilon_2(\eta\xi - <\eta\xi>))$$

(3.16)

With δ_2 given by:

$$\delta_2 = - \frac{a'}{b'}$$

(3.17)

in analogy to equation (3.13). We define u' and w' as the standard deviations of the respective velocities at the location of the probe at which the voltage time series $a(t)$ and $b(t)$ were taken. We need 5 conditions to find the coefficients:

$$\delta_1 , \gamma_1 , \gamma_2 , \epsilon_1 , \epsilon_2$$

From experimental data we know that γ_1, ϵ_1 and ϵ_2 are positive quantities, the sign of γ_2 determines the direction of positive $w(t)$, and five conditions can be found by satisfying all second order moments and the third moment $<u^3>$ and $<uw^2>$. The choice for these two third order moments was made because $<u^3>$ varied most rapidly with ϵ_1 while all other third order moments were almost unaffected by it. Changes in ϵ_2 affected dominantly $<uw^2>$.

The relationships between second and third order moments of velocities and voltages can be obtained by introducing equation (3.15) into (3.16) and taking the square (cube) of both sides of the resulting equations. After taking the ensemble average the time-dependent terms are replaced by their corresponding central moments of velocity and voltage fluctuations. The resulting equations are highly non-linear because the 5 coefficients to be determined appear in forms of up to triple products. Under the assumption of ϵ_1 and ϵ_2 equal to zero the system can be solved, satisfying only the second order moments. Then one finds a first approximation to ϵ_1 and ϵ_2 from the 2 third order equations and enters with them the equations for the second order moments to find better values for δ_1, γ_1, and γ_2. The iteration converges after a few cycles.

The above scheme worked exceptionally well except for the largest wall-distance. There the autocorrelations obtained with indirectly calibrated sensors deviated slightly from those obtained with directly calibrated sensors. Discrepancies occured most strongly in the w-component. In addition the iteration scheme did not always converge which we attributed to a lack of freedom in the proposed equation system and inability to represent the nonlinearities in the sensor response.

We extended the w(t)-component of equation (3.16) to:

$$w(t) - w' \; \gamma_2 \left[\begin{array}{l} \xi + \epsilon_2(\eta\xi - \langle\eta\xi\rangle) \\ + \epsilon_3(\xi^2 - \langle\xi^2\rangle) \\ + \epsilon_4(\eta^2 - \langle\eta^2\rangle) \end{array} \right] \tag{3.18}$$

With two new constants all second and third order velocity moments can now be identically matched to the experimental values. The autocorrelations obtained with the inverse calibration were correct to within 10^{-3} [$R(\tau=0)=1$]. Plots of velocity time series and Reynolds stress brought agreement to within plotting accuracy, see Figure (13).

Chapter IV

ORTHOGONAL DECOMPOSITION

4.1 INTRODUCTION

To extract possibly present structures from a random vector field $U_i(-)$ Lumley (1967) suggests to consider the squared modulus of the correlation in ensemble mean between $U_i(-)$ and a candidate $\psi_i(-)$ for the structure:

$$\lambda = \frac{< \left[\int \psi_i(-) \, U_i^*(-) \, d(-) \right] \left[\int \psi_j(+) \, U_j^*(+) \, d(+) \right]^* >}{\int \psi_k(,) \, \psi_k^*(,) \, d(,)} \tag{4.1}$$

The dimensionality of the integration may be less than or equal to dimensionality of the space in which U_i is measured, in general three spacial coordinates and time. The operator $< \ >$ denotes here the ensemble average. Extremizing λ can be done by classical methods of variational calculus and leads to the well-known eigenvalue problem:

$$\psi_i(-) = \int R_{ij}(\ (-),(+) \ ) \ \psi_j(+) \ d(+) \tag{4.2}$$

with the velocity correlation tensor:

$$R_{ij}(\ (-),(+) \ ) = < U_i(-) \ U_j^*(+) \ > \tag{4.3}$$

-42-

For incompressible flow we have on the basis of the continuity equation:

$$\frac{\partial R_{ij}}{\partial x_i} = 0 \tag{4.4}$$

which when used in conjunction with equation (4.2) gives:

$$\lambda \frac{\partial \psi_i}{\partial x_i} = 0 \tag{4.5}$$

We define now a variety of coordinate vectors. Let $\underline{y}$ contain all those coordinates for which the random vector field is either stationary or homogeneous,

$$\underline{y} = (\; x_1 \; x_3 \; t \;) \tag{4.6}$$

The vector $\underline{x}$ contains all those coordinates for which we have inhomogeneity:

$$\underline{x} = (\; x_2 \;) \tag{4.7}$$

Furthermore:

$$\underline{r} = \underline{y} - \underline{y}' = (\; x_1 - x_1' \;,\; x_3 - x_3' \;,\; t - t' \;) \tag{4.8}$$

with a corresponding wave-number vector:

$$\underline{k} = (\; k_1 \;,\; k_3 \;,\; f \;) \tag{4.9}$$

The dimensionality of integration in equation (4.2) can be reduced by the number of stationary/homogeneous coordinates. One way to do this is to propose a solution to equation (4.2) of the form:

$$\phi_i(\underline{x}\ \underline{k}) = \psi_i(\underline{x}\ \underline{r})\ e^{-2\pi i \underline{kr}}\ d\underline{r} \tag{4.10}$$

With the spectral tensor defined by:

$$S_{ij}(\underline{x}\ \underline{x}'\ \underline{k}) = \int\limits_{-\infty}^{+\infty} R_{ij}(\underline{x}\ \underline{x}'\ \underline{r})\ e^{-2\pi i \underline{kr}}\ d\underline{r} \tag{4.11}$$

equation (4.2) reduces to:

$$\lambda(\underline{k})\ \phi_i(\underline{x}\ \underline{k}) = \int\limits_{\Omega} S_{ij}(\underline{x}\ \underline{x}'\ \underline{k})\ \phi_j(\underline{x}'\ \underline{k})\ d\underline{x}' \tag{4.12}$$

the wave-number $\underline{k}$ appearing only as parameter.

The integration domain Ω in the space of inhomogeneous coordinates is, at least in our investigation, finite and the spectral tensor $S_{ij}(\underline{x}\ \underline{x}'\ \underline{k})$ is square-integrable. Because the original correlation tensor $R_{ij}()$ is symmetric as can be seen from equation (4.3), $S_{ij}()$ is hermitian. Solutions to equation (4.12) are then governed by the theorems of the Hilbert-Schmidt theory of linear integral equations.

a) There exist a denumerable set of eigenvalues $\lambda^{(n)}$ satisfying equation (4.12).

b) All eigenvalues are real-valued.

c) The corresponding eigenfunctions are othogonal and can be normalized:

$$\int_{\Omega} \phi_i^{(m)}(\underline{x} \; \underline{k}) \; \phi_i^{(n)*}(\underline{x} \; \underline{k}) \; d\underline{x} = \delta_{mn} \qquad (4.13)$$

d) There exists a bilinear representation of the kernel in terms of the orthonormal eigenfunctions:

$$S_{ij}(\underline{x} \; \underline{x}' \; \underline{k}) = \sum_n \lambda^{(n)}(\underline{k}) \; \phi_i^{(n)}(\underline{x} \; \underline{k}) \; \phi_j^{(n)*}(\underline{x}' \; \underline{k}) \qquad (4.14)$$

e) At least any random function which belongs to the set of functions generating the kernel S_{ij} can be represented in terms of the eigenfunctions:

$$u_i(\underline{x} \; \underline{k}) = \sum_n a^{(n)}(\underline{k}) \; \phi_i^{(n)}(\underline{x} \; \underline{k}) \qquad (4.15)$$

and the random coefficients of different orders are uncorrelated and their variance equals the eigenvalue of equal order.

$$< a^{(m)}(\underline{k}) \; a^{(n)*}(\underline{k}) > = \lambda^{(n)}(\underline{k}) \; \delta_{mn} \qquad (4.16)$$

f) For any realization of the random vector field we obtain the random coefficients by:

$$a^{(n)}(\underline{k}) = \int_{\Omega} u_i(\underline{x} \; \underline{k}) \; \phi_i^{(n)*}(\underline{x} \; \underline{k}) \; d\underline{x} \qquad (4.17)$$

Because $S_{ij}()$ is positive-definite, see Lumley (1970), all eigenvalues of equation (4.13) are positive. $\lambda^{(n)}(\underline{k})$ is associated with the energy density of the n-th order eigenfunction at wave-number $\underline{k}$.

Solutions for the eigenfunctions are only unique to within an arbitrary phase-factor, that is, if $\phi_i^{(n)}(\underline{x}\ \underline{k})$ is a solution of the eigenvalue problem then

$$\phi_i^{(n)}(\underline{x}\ \underline{k})\ e^{i\theta(\underline{k})}$$

is a solution also, satisfying not only the original eigenvalue equation, (4.12), but also equations (4.13) to (4.17). The function $\theta(\underline{k})$ is not determinable from second order statisitics. It depends only on the wave-number vector $\underline{k}$ which is associated with the homogeneous/stationary coordinates.

Having $S_{ij}()$ available from experimental measurements or numerical simulation the determination of the eigenvalues and functions as function of wave-number $\underline{k}$ is straight forward and usually done numerically. The recovery of the eigenfunctions in physical space needs to be addressed separately.

4.2 EIGENFUNCTIONS IN PHYSICAL SPACE

Using equation (4.15) and (4.10) we may recreate any realization of the random vector field in physical space in terms of the eigenfunctions. The part thereof associated with the largest eigenvalue, say $\lambda^{(1)}$, which we identify with the "timetrace" of the random occurrence of typical eddies is:

$$U_i^{(1)}(\underline{x}\ \underline{y}) - \int_{-\infty}^{+\infty} a^{(1)}(\underline{k})\ \phi_i^{(1)}(\underline{x}\ \underline{k})\ e^{-2\pi i\underline{k}\underline{y}}d\underline{k} \qquad (4.18)$$

Equation (4.18) though is simply a Fourier-mode description of the flow field and although we may suspect that a typical eddy can be obtained by replacing $a^{(1)}(\underline{k})$ in equation (4.18) by

$$\left[\lambda^{(1)}(\underline{k})\right]^{1/2} \qquad (4.19)$$

additional information is needed about the phase relation between the contributions to the typical eddy from different wave-numbers.

Following Lumley (1967) any stationary random function can be written in the form:

$$U_i^{(1)}(\underline{x}\ \underline{y}) - \int_{-\infty}^{+\infty} F_i(\underline{x}\ \underline{y}-\underline{y}')\ G(\underline{y}')\ d\underline{y}' \qquad (4.20)$$

in which $F_i()$ is a deterministic function representing the typical eddy in physical space. $G()$ is a stochastic function describing the occurrence and individual magnitude of the typical eddies.

We equate the representation of a realization of the random vector field from equation (4.18) with that from (4.20) and take the Fourier transform using the convolution theorem. We obtain:

$$f_i(\underline{x}\ \underline{k})\ g(\underline{k}) - a^{(1)}(\underline{k})\ \phi_i^{(1)}(\underline{x}\ \underline{k}) \qquad (4.21)$$

in which $g(\underline{k})$ is the Fourier transform of $G(\underline{y})$ and $f_i(\underline{x}\ \underline{k})$ the Fourier transform of the deterministic function $F_i(\underline{x}\ \underline{y})$ with respect to $\underline{y}$. Multiplying equation (4.21) by its conjugate complex and taking the ensemble average results in:

$$f_i(\underline{x}\ \underline{k})\ f_j^*(\underline{x}\ \underline{k})\ S_G(\underline{k}) = \lambda^{(1)}(\underline{k})\ \phi_i^{(1)}(\underline{x}\ \underline{k})\ \phi_j^{(1)*}(\underline{x}\ \underline{k}) \qquad (4.22)$$

with $S_G(\underline{k})$ being the spectrum of the stochastic function $G()$. From this we immediately obtain:

$$f_i(\underline{x}\ \underline{k}) = \left[\frac{\lambda^{(1)}(\underline{K})}{|S_G(\underline{k})|}\right]^{1/2} \phi_i^{(1)}(\underline{x}\ \underline{k})\ e^{i\theta(\underline{k})} \qquad (4.23)$$

And the typical eddy in physical space is described by:

$$F_i(\underline{y}) = \int\limits_{-\infty}^{+\infty} f_i(\underline{x}\ \underline{k})\ e^{2\pi i \underline{k}\underline{y}}\ d\underline{k} \qquad (4.24)$$

The phase angle $\theta(\underline{k})$ is still undetermined. As far as equation (4.22) is concerned it may be a function of the inhomogeneous coordinates $\underline{x}$ as well and may be even different for each component of the typical eddy. We require though that each wave number component, $f_i()$, of the typical eddy satisfies the original eigenvalue equation (4.12) and the continuity equation, (4.5). This demands the proposed form of $\theta()$. Note that $\phi_i(\underline{x}\ \underline{k})$ as solution of equation (4.12) is in general complex valued containing relative phase-shift information in the direction of the inhomogeneous

coordinates. It is only the phase relation among the eigenfunctions at different wave-numbers which is incorporated into $\theta()$ and which is undetermined.

Using equation (4.21) again we obtain in similar way as above for the spectra, a bi-spectral relationship:

$$f_i(\underline{x}\ \underline{k}')\ f_j(\underline{x}\ \underline{k}'')\ f_k^*(\underline{x}\ \underline{k}'+\underline{k}'')\ B_G(\underline{k}'\ \underline{k}'') = \tag{4.25}$$

$$<a^{(1)}(\underline{k}')\ a^{(1)}(\underline{k}'')\ a^{(1)*}(\underline{k}'+\underline{k}'')>\ \phi_i^{(1)}(\underline{x}\ \underline{k}')\ \phi_j^{(1)}(\underline{x}\ \underline{k}'')\ \phi_k^{(1)*}(\underline{x}\ \underline{k}'+\underline{k}'')$$

The bi-spectrum $B_G(\underline{k}_1\ \underline{k}_2)$ of the stochastic function $G(\underline{y})$ is here defined as Fourier transform of its triple auto-correlation function:

$$B_G(\underline{k}'\ \underline{k}'') = \int\limits_{-\infty}^{+\infty}\int R_G(\underline{y}'\ \underline{y}'')\ e^{-2\pi i(\underline{k}'\underline{y}'+\ \underline{k}''\underline{y}'')}\ d\underline{y}'\ d\underline{y}'' \tag{4.26}$$

see also Hasselmann et al. (1962) and Rosenblatt (1966). Introducing equation (4.23) into equation (4.25) we obtain an implicit equation for the phase angle $\theta(\underline{k})$:

$$e^{i(\ \theta(\underline{k}')\ +\ \theta(\underline{k}'')\ -\ \theta(\underline{k}'+\underline{k}'')\ )} = \tag{4.27}$$

$$\frac{<a^{(1)}(\underline{k}')\ a^{(1)}(\underline{k}'')\ a^{(1)*}(\underline{k}'+\underline{k}'')>}{B_G(\underline{k}'\ \underline{k}'')}\ \left[\frac{|S_G(\underline{k}')|\ |S_G(\underline{k}'')|\ |S_G(\underline{k}'+\underline{k}'')|}{\lambda^{(1)}(\underline{k}')\ \lambda^{(1)}(\underline{k}'')\ \lambda^{(1)}(\underline{k}'+\underline{k}'')}\right]^{1/2}$$

We are now in the position of solving (4.27) for the phase angle $\Theta(\underline{k})$ and then determine the form of the typical eddy by using equation (4.24) with (4.23), provided that power and bi-spectrum of $G(\underline{y})$ are available.

A specialization of Lumley's (1967) approach is to suppose that $G(\underline{y})$ is an infinite sum of δ-functions with random amplitude A_i and random occurrences, $\underline{y}_i$, in the space of the homogeneous/stationary coordinates.

$$G(\underline{y}) = \sum_i A_i \, \delta(\underline{y} - \underline{y}_i) \qquad\qquad (4.28)$$

A similar form was already proposed by Goldshtik (1982).

Assuming now that adjacent occurrences are uncorrelated and that the duration, $\underline{y}_i - \underline{y}_{i+1}$, between occurrences and their amplitudes A_i are uncorrelated as well, equation (4.28) can be evaluated to give the power-spectrum of $G(\underline{y})$

$$S_G(\underline{k}) = \mu_G^{-1} < A_i^2 > \qquad\qquad (4.29)$$

and its bi-spectrum

$$B_G(\underline{k}_1 \; \underline{k}_2) = \mu_G^{-1} < A_i^3 > \qquad\qquad (4.30)$$

The average sojourn "time" μ_G between occurrences of the typical eddy is unknown.

The above assumptions produced the result that the power- and bi-spectrum of the stochastic function are real-valued and independent of wave-number vector $\underline{k}$. Introducing equation (4.29) and (4.30) back into (4.27) and considering for the moment only the norm of both sides of the resulting equation, we obtain:

$$\frac{| < a^{(1)}(\underline{k}') \; a^{(1)}(\underline{k}'') \; a^{(1)*}(\underline{k}'+\underline{k}'') > |}{\left[\lambda^{(1)}(\underline{k}') \; \lambda^{(1)}(\underline{k}'') \; \lambda^{(1)}(\underline{k}'+\underline{k}'') \right]^{1/2}} = \qquad (4.31)$$

$$= \mu_G^{1/2} \; \frac{< A_i^3 >}{\left[< A_i^2 > \right]^{3/2}} = \text{constant}$$

The left-hand side of equation (4.31) is solely determined by the turbulent flow under consideration and it is doubtful that its outcome is indeed constant for all wave-number pairs $\underline{k}_1$ and $\underline{k}_3$.

One way to remedy this situation is to drop some of the assumptions about the lack of correlations among adjacent occurrences in order to obtain spectra of the stochastic function $G(\underline{y})$ which do depend on wave-number $\underline{k}$. In a certain sense it is actually quite well-come, that experimental results prescribe some of the properties of $G(\underline{y})$.

We feel though, that the problem here is more general in nature and it is not confined to the approach of shot-noise effect expansion at all.

Basically, what we are trying to do is to find some sort of simple model to represent the random coefficient $a^{(1)}(\underline{k})$ utilizing informations from its power spectrum $<a^{(1)}() \; a^{(1)*}()>$ and its

bi-spectrum $\langle a^{(1)}(\underline{k}') \, a^{(1)}(\underline{k}'') \, a^{(1)*}(\underline{k}'+\underline{k}'') \rangle$. Although present knowledge indicates that the dominant eigenmode represents randomly sprinkled eddies, their individual sizes and shapes vary considerably. We cannot expect that these random variations could be expressed by a single amplitude variable as in equation (4.28) to such a degree, that all aspects of the power- and bi-spectrum are satisfied simultaneously. This has to be expected even if these eddies occur in a completely uncorrelated fashion.

Another problem associated with equation (4.27), and which again is by no means confined to the shot-noise effect approach is that of the availibility of higher order statisitics of the random coefficients.

To determine the statistics of the $a^{(1)}(\underline{k})$ we have to start with equation (4.17). An individual realization of the random coefficient can be obtained by Fourier transforming a realization of the complete flow field with respect to the homogeneous/stationary coordinates to obtain $u_i(x_2 \, \underline{k})$ in equation (4.17). Obviously this is not feasible when starting from experimentally obtained data. Even the simpliest case, with only the time as homogeneous coordinate (so that the problem of the Fourier transform is solvable), still requires to measure simultaneously at several values of the inhomogeneous coordinate x_2 in order to perform the integration as required by equation (4.17).

An alternate way is to use equation (4.17) to derive first closed expressions for the desired statistic. For the bispectrum

$$B(\underline{k}' \, \underline{k}'') = \langle a^{(1)}(\underline{k}') \, a^{(1)}(\underline{k}'') \, a^{(1)*}(\underline{k}'+\underline{k}'') \rangle \qquad (4.32)$$

we obtain with the aid of equation (4.17) immediately:

$$
B(\underline{k}' \ \underline{k}'') = \iiint\limits_{\Omega} < u_i(x_2 \ \underline{k}') \ u_j(x_2' \ \underline{k}'') \ u_l(x_2'' \ \underline{k}'+\underline{k}'') >
$$

$$
\phi_i^{(1)*}(x_2\underline{k}') \ \phi_j^{(1)*}(x_2' \ \underline{k}'') \ \phi_l^{(1)}(x_2'' \ \underline{k}'+\underline{k}'') \ dx_2 dx_2' dx_2''
$$

(4.33)

(Summation over i j and l)

The required bi-spectrum of the flow field can be measured by three probes only which have to be moved over all permutations of x_2, x_2' and x_2'' in order to perform the triple integration of equation (4.33).

Such measurements are order of magnitudes more extensive than obtaining the usual spectral tensor. We have measured only with two probes at a time and therefor cannot evaluate equation (4.33). Note that we are not able to integrate equation (4.33) with respect to wave-number $\underline{k}$ because the bi-spectrum and the eigenfunctions cannot be separated.

At this state of the affair any type of approximation to the bi-spectrum of the dominant eigenmode however crude is welcome. We will assume that the representation of a "typical" eddy of equation (4.23) and (4.24) holds. In the two following sections of this chapter we derive restrictions on the functional form of the phase-shift function $\theta(\underline{k})$ of equation (4.23) and the symmetry properties of the eigenfunctions in $\underline{k}$-space.

4.3 STRUCTURE OF SOLUTIONS IN WAVE-NUMBER SPACE

Valuable information concerning characteristics of the typical eddy
and the phase-shift function $\theta(\underline{k})$ of equation (4.23) can be obtained
by taking into account properties of the flow under consideration
exceeding those we used sofar in the discussion of the proper
orthogonal decomposition scheme.

We specifically will address the following points:

a) The original correlation tensor R_{ij}, equation (4.3),
   as well as the function $F_i()$, equation (4.24), describing
   the typical eddy are real-valued.

b) The flow field is symmetric with respect to the spanwise
   coordinate x_3 in addition to being homogeneous.

c) The influence of the incompressibility condition, equation
   (4.4) and (4.5).

d) The typical eddy in physical space is to be symmetric
   in spanwise direction.

Furthermore we eliminate time as independent variable from our
consideration, that is we consider the correlation tensor R_{ij} only
for $t-t'=0$. This means that we will obtain an average, in the sense
of equation (4.1), of all eddies as they appear in "snap-shots"
taken of the flow field.

Let x_1 be the streamwise and x_3 the spanwise coordinate with an
associated wave-number vector $\underline{k}=(k_1,k_3)$. x_2 is the wall-normal
coordinate. The eigenvalue equation, (4.12), becomes then:

$$\lambda(\underline{k})\ \phi_i(x_2\ \underline{k}) = \int_0^B S_{ij}(x_2\ x_2'\ \underline{k})\ \phi_j(x_2'\ \underline{k})\ dx_2' \qquad (4.34)$$

$$B = \text{maximum wall-distance}$$

For the incompressibility condition we obtain:

$$2\pi i \left[k_1 \, \phi_1(x_2 \, \underline{k}) + k_3 \, \phi_3(x_2 \, \underline{k}) \right] + \frac{\partial \phi_2(x_2 \, \underline{k})}{\partial x_2} = 0 \tag{4.35}$$

Subsequent discussion is greatly facilitated by looking at the discretized counterparts of equation (4.34) and (4.35).

Let $(x_2(q), q=1, N)$ be the set of wall-distances for which data of the spectral tensor are available. An integration from the wall outwards of an arbitrary function $h(x_2)$ can be defined by:

$$H(p) = \sum_q D_{pq} \, h(q) \tag{4.36}$$

The N*N matrix D_{pq} is zero in its upper triangle and in the case of equi-distant spacing of unity it is 1/2 on the main diagonal and unity in its lower triangle. Differentiation, as inverse operation to equation (4.36), is then simply:

$$h(q) = \sum_p D_{qp}^{-1} \, H(p) \tag{4.37}$$

Equation (4.34) can now be rewritten in the form

$$\lambda \, \phi_i(p) = \sum_{j,q} S_{ij}(p \, q) \, \phi_j(q) \, D_{Nq} \tag{4.38}$$

and equation (4.35) becomes:

$$2\pi i \left[k_1 \, \phi_1(p) + k_3 \, \phi_3(p) \right] + \sum_q D_{pq}^{-1} \, \phi_2(q) = 0 \tag{4.39}$$

Equation (4.38) is a 3*N by 3*N matrix eigenvalue problem and we hence expect 3*N eigenvalues with associated eigenfunctions. The system is overdetermined though because of the incompressibility condition imposed on the spectral tensor. We use equation (4.39) to eliminate ϕ_2 from (4.38):

$$\lambda \; \phi_1(p) - \sum_q A_{11}(p \; q) \; \phi_1(q) \; + \; \sum_q A_{13}(p \; q) \; \phi_3(q)$$

$$\lambda \; \phi_3(p) - \sum_q A_{31}(p \; q) \; \phi_1(q) \; + \; \sum_q A_{33}(p \; q) \; \phi_3(q)$$

(4.40)

with the matrices A_{ij} defined as:

$$A_{11}(p \; q) - \left[\; S_{11}(p \; q) \; - \; 2\pi i k_1 \sum_m S_{12}(p \; m) \; D_{mq} \right] \; D_{Nq}$$

$$A_{13}(p \; q) - \left[\; S_{13}(p \; q) \; - \; 2\pi i k_3 \sum_m S_{12}(p \; m) \; D_{mq} \right] \; D_{Nq}$$

$$A_{31}(p \; q) - \left[\; S_{31}(p \; q) \; - \; 2\pi i k_1 \sum_m S_{32}(p \; m) \; D_{mq} \right] \; D_{Nq}$$

$$A_{33}(p \; q) - \left[\; S_{33}(p \; q) \; - \; 2\pi i k_3 \sum_m S_{32}(p \; m) \; D_{mq} \right] \; D_{Nq}$$

This equation system yields now only 2*N eigenvalues.

We invoke now the fact that the boundary layer flow is symmetric in the spanwise direction. In terms of the correlation tensor R_{ij} this means, that it is an even function of x_3 for all cases when neither subscript i nor j are equal to three or when i=j=3. All

other components of the correlation tensor are odd functions of x_3.
It is worthwhile, to recall that the Fourier transform of an even/odd
(complex valued) function results in a function in wave-number space
which is even/odd again in its real and imaginary part. The same is
of course true for the inverse transform.

With that it is now easy to see that the complex valued
coefficients A_{11} and $\dot{A}_{33}$ are even functions and A_{13} and A_{31} odd
functions of wave-number k_3.

Let $\left[\alpha_1(q), \alpha_3(q) \right]$ now be the values of the solution to the
equation system (4.40) at some $k_3=b>0$. By inspection, under
consideration of the even/oddness behaviour of the A_{ij}, we see that
there are two possible solutions at $k_3=-b$, namely:

$$\left[\alpha_1(q), -\alpha_3(q) \right] \tag{4.41}$$

and

$$\left[-\alpha_1(q), \alpha_3(q) \right] \tag{4.42}$$

On first sight the distinction between the two forms seems to be
superflous because they differ only by an irrelevant phase-factor of
-1. But by considering the special case of $k_3=0$ we arrive at the
condition of

$$\alpha_3(q)=-\alpha_3(q)=0 \ , \quad \alpha_1(q)\neq 0$$

for the first form and

$$\alpha_1(q)=-\alpha_1(q)=0 \ , \quad \alpha_3(q)\neq 0$$

for the second, which cannot be recovered from each other by multiplying with any phase-factor.

This special behaviour at $k_3 = 0$, that either $\alpha_1(q) = 0$ or $\alpha_3(q) = 0$, can be explained directly with equation (4.40). At $k_3 = 0$ we have $A_{13} = A_{31} = 0$ for all values of p and q. The system decouples into separate eigenvalue problems for $\phi_1(q)$ and $\phi_3(q)$. Each system yields N eigenvalues and in general these two sets are distinct, forcing $\phi_3 = 0$ at an eigenvalue of the ϕ_1-system and vice-versa.

Which of the total of 2*N eigenvalues are associated with which type of eigenfunction is a matter of the actual values of the matrices A_{11} and A_{33}. Because A_{11} is dominated by the streamwise velocity component and A_{33} by the spanwise velocity component the largest eigenvalue goes with an eigenfunction of the type as indicated in equation (4.41). Our experimental data indicate that the 3. largest eigenvalue solution complies with the type of equation (4.42), for almost all wave-numbers investigated.

Although there certainly is no symmetry in the flow with respect to any value of x_1 we might ask ourselves how the values of a solution at some $k_1 = -a < 0$ are related to $\left[\alpha_1(q), \alpha_3(q) \right]$ at $k_1 = a > 0$. The obvious answer that they are conjugate complex of each other is wrong.

To show this, we start with the correlation tensor R_{ij}. Because it is real-valued and has the indicated special symmetry properties its Fourier transform with respect to x_3 will be a real-valued function for

$$i,j = 11 \ 12 \ 21 \ 22 \text{ and } 33 \qquad (a)$$

and for

$$i,j = 13 \ 31 \ 23 \ \text{and} \ 32 \qquad (b)$$

the outcome will have purely imaginary values. Fourier transforming

now with respect to x_1 presents immediately the relationships:

$$S_{ij}(k_1 = -b) = S_{ij}^*(k_1 = b) \quad \text{for i,j = (a)}$$

$$S_{ij}(k_1 = -b) = -S_{ij}^*(k_1 = b) \quad \text{for i,j = (b)}$$

From this we obtain for the matrices of equation system (4.40) :

$$A_{11}(k_1 = -b) = A_{11}^*(k_1 = b)$$

$$A_{33}(k_1 = -b) = A_{33}^*(k_1 = b)$$

$$A_{13}(k_1 = -b) = -A_{13}^*(k_1 = b)$$

$$A_{31}(k_1 = -b) = -A_{31}^*(k_1 = b)$$

By inspection of the matrix system, equation (4.40), we see now that

if $\left[\ \alpha_1(q), \alpha_3(q) \ \right]$ are the values of the solution at some $k_1 = a > 0$

then:

$$\left[\ \alpha_1^*(q), -\alpha_3^*(q) \ \right]$$

is obtained at $k_1 = -a$. No splitting into two branches due to

decoupling occurs at $k_1 = 0$ because none of the A_{ij} vanishes.

The following Figure (14) summarizes our findings for the

solution type for our dominant eigenvalue. ϕ_2 follows exactly the

pattern of ϕ_1 as can be best seen by considering equation (4.35) and

is included. The eigenvalue itself is a symmetric function with

respect to k_1 as well as k_3.

$$\begin{array}{c|c} & \Big|\, k_3 \\ \phi_1^* \;,\; \phi_2^* \;,\; -\phi_3^* & \Big|\; \phi_1 \;,\; \phi_2 \;,\; \phi_3 \\ \hline & \Big|\quad\qquad\qquad k_1 \\ \phi_1^* \;,\; \phi_2^* \;,\; \phi_3^* & \Big|\; \phi_1 \;,\; \phi_2 \;,\; -\phi_3 \\ & \Big| \end{array}$$

Figure 14: Structure of solutions in wave-number space

The shown pattern is not unique of course but can be obtained always and will prove to be of advantage when defining the phase-shift function $\Theta(\underline{k})$ with respect to it. An infinity of such patterns exists though for a given spectral tensor S_{ij} because of the ambiguity in defining zero phase shift. In our computer code we chose for example to have ϕ_1 at the wall-furthest x_2 be purely real-valued and negative at some k_1,k_3 and observed continuity in said ϕ_1 and its derivative with respect to k_1 and k_3. Except for the continuity requirement (to obtain later a continous function for the phase-shift) our choice is completely arbitrary.

4.4   STRUCTURE OF SOLUTIONS IN PHYSICAL SPACE

We include now the requirement that the functional description of a typical eddy in physical space has to be real-valued and symmetric in ϕ_1 and ϕ_2 and antisymmetric in ϕ_3. We combine equations (4.23) and (4.24) setting the undetermined spectrum $S_G(\underline{k})$ equal to one, which we can do because it is only an irrelevant scaling factor. We obtain:

$$F_i = \int\!\!\int_{-\infty}^{+\infty} \left[\lambda^{(1)}(\underline{k})\right]^{1/2} \phi_i^{(1)}(x_2\ \underline{k})\ e^{i\theta(\underline{k})}\ e^{2\pi i(k_1 x_1 + k_3 x_3)}\ dk_1 dk_3 \qquad (4.43)$$

$\phi_i(x_2\ \underline{k})$ is complex valued and depending on x_2 while the phase-shift function $\theta(\underline{k})$ does not. Hence we cannot expect an annihilation of the imaginary parts in general. Only one method is available: the contributions to the integral from each of the four quadrants at a given $|k_1|$-constant, $|k_3|$-constant mutually cancel their imaginary parts. $\lambda(\underline{k})$ has no influence because of its overall symmetric behaviour.

The restrictions this imposes on $\theta(\underline{k})$ can be derived easily if we decompose $\theta(\underline{k})$ into four functions, the first being an even function of k_1 and k_3, the second an odd functions of both wave-numbers, the third even in k_1 but odd in k_3, and the fourth function finally odd in k_1 and even in k_3. Let M_{ee}, M_{oo}, M_{eo}, and M_{oe} be now their respective values at some arbitrary $k_1=a>0$ and $k_3=b>0$. Summing up the contributions of the four points $|k_1|=a$, $|k_3|=b$ for the spanwise velocity component, $i=3$, of equation (4.43) we obtain:

$$I = \phi_3\ e^{+2\pi i k_1 x_1}\ e^{+2\pi i k_3 x_3}\ e^{iM_{ee}}\ e^{+iM_{oo}}\ e^{+iM_{oe}}\ e^{+iM_{eo}}$$

$$- \phi_3^*\ e^{-2\pi i k_1 x_1}\ e^{+2\pi i k_3 x_3}\ e^{iM_{ee}}\ e^{-iM_{oo}}\ e^{-iM_{oe}}\ e^{+iM_{eo}}$$

$$+ \phi_3^*\ e^{-2\pi i k_1 x_1}\ e^{-2\pi i k_3 x_3}\ e^{iM_{ee}}\ e^{+iM_{oo}}\ e^{-iM_{oe}}\ e^{-iM_{eo}}$$

$$- \phi_3\ e^{+2\pi i k_1 x_1}\ e^{-2\pi i k_3 x_3}\ e^{iM_{ee}}\ e^{-iM_{oo}}\ e^{+iM_{oe}}\ e^{-iM_{eo}}$$

or:

$$I = e^{iM_{ee}} \; e^{iM_{oo}} \; 2 \; \text{Real}\left[\phi_3 \; e^{2\pi i k_1 x_1} \; e^{+2\pi i k_3 x_3} \; e^{iM_{oe}} \; e^{+iM_{eo}}\right]$$

$$- e^{iM_{ee}} \; e^{iM_{oo}} \; 2 \; \text{Real}\left[\phi_3 \; e^{2\pi i k_1 x_1} \; e^{-2\pi i k_3 x_3} \; e^{iM_{oe}} \; e^{-iM_{eo}}\right]$$

Because ϕ_3 depends on x_2 but M_{ee} and M_{oo} do not, we arrive at the condition:

$$e^{iM_{ee}} \; e^{iM_{oo}} - e^{iM_{ee}} \; e^{-iM_{oo}} = \pm 1$$

With that we can proceed now and obtain:

$$I = \pm \; \text{Real}\left[\phi_3 \; e^{2\pi i k_1 x_1} \; e^{iM_{oe}} \; 2i \left[\begin{matrix} \cos(2\pi k_3 x_3) \; \sin M_{eo} \\ +\sin(2\pi k_3 x_3) \; \cos M_{eo} \end{matrix}\right] \right]$$

The condition that this be now an odd function of x_3 requests that $M_{eo} = 0$.

The only term remaining is M_{oe} which says that $\theta(k_1 \; k_3)$ is strictly an odd function of k_1 and an even function of k_3. Expanding the phase-shift function in terms of a polynomial we obtain:

$$\theta(k_1 \; k_3) = \sum_{p,q=0..} a_{pq} \; k_1^{2p+1} \; k_3^{2q} \tag{4.44}$$

with an ambiguity in sign for $e^{i\theta(k_1 \; k_3)}$. The other two components of ϕ_i of equation (4.43) can be treated in analog fashion leading to the same requirements. Of course, equation (4.44) is only valid if

one chooses a pattern for the eigenfunctions in the k_1-k_3 plane as shown in Figure (14). For the eigenfunctions which show an anti-symmetric pattern but which are not relevant for our investigations, a similar derivation can be made.

The restricted functional form of the phase-shift function allows us to look at some of the properties of the typical eddy in physical space without making any statements concerning the values of the coefficients a_{pq} of equation (4.44).

We may ask ourselves how the typical eddy looks if we integrate in the streamwise direction. Integrating $F_i()$ over x_1 is equivalent to taking the Fourier transform of equation (4.43) with respect to x_1 at k_1=0.

$$\int_{-\infty}^{+\infty} F_i() \; dx_1 = \int_{-\infty}^{+\infty} \left[\lambda^{(1)}(k_3,k_1=0)\right]^{1/2} \phi_i^{(1)}(x_2 k_3, k_1=0) \; e^{-2\pi i k_3 x_3} \; dk_3 \qquad (4.45)$$

The phase-shift function is here identically zero because k_1=0 and equation (4.45) can be directly integrated. This is the reason why previous investigators, Bakewell (1967) and Moin (1984), obtained convincing pictures of counter-rotating structures when assuming zero phase-shift.

One step further would be to integrate the typical eddy over the complete k_1-k_3 plane for each value of x_2. We obtain:

$$\iint_{-\infty}^{+\infty} F_i() \; dx_1 \; dx_3 = \left[\lambda^{(1)}(\underline{k}=0)\right]^{1/2} \phi_i^{(1)}(x_2 \; \underline{k}=0) \qquad (4.46)$$

From Figure (14) we see that $\phi_3^{(1)} = 0$ at $k_1=k_3=0$ and that $\phi_1^{(1)}$ is strictly real-valued. From the incompressibility condition we obtain furthermore that $\phi_2^{(1)}$ vanishes too. This confirms what one might expect on more physical grounds, that in each wall-parallel plane, x_2-constant, the typical eddy experiences on the average no span-wise motion and has no net-velocity in the wall-normal direction. The mean of the streamwise velocity component as a function of x_2 can be directly obtained from equation (4.46), setting i=1.

We conclude this section by rewriting equation (4.43). After making use of the derived properties the integration can be restricted to just the first quadrant in k_1-k_3 space.

$$F_i(\underline{x}) = +4 \int\!\!\int_0^{+\infty} \cos(2\pi k_3 x_3) \left[PR_i \cos(2\pi k_1 x_1) - PI_i \sin(2\pi k_1 x_1) \right] dk_1 \, dk_3$$

$$\text{for} \quad i=1,2 \tag{4.47}$$

and

$$F_3(\underline{x}) = -4 \int\!\!\int_0^{+\infty} \sin(2\pi k_3 x_3) \left[PR_3 \sin(2\pi k_1 x_1) + PI_3 \cos(2\pi k_1 x_1) \right] dk_1 \, dk_3$$

for i=3, with

$$PR_i = \text{Real}\left(\left[\lambda^{(1)}(\underline{k})\right]^{1/2} \phi_i^{(1)}(x_2 \, \underline{k}) \, e^{i\theta(\underline{k})} \right)$$

$$PI_i = \text{Imag}\left(\left[\lambda^{(1)}(\underline{k})\right]^{1/2} \phi_i^{(1)}(x_2 \, \underline{k}) \, e^{i\theta(\underline{k})} \right)$$

The desired symmetry property with respect to x_3 is clearly visible.

Chapter V

RESULTS AND DISCUSSION

5.1 SINGLE-PROBE MEASUREMENTS

With a calibrated hot-splitfilm probe, as described earlier, we measured single-point statistics. The results presented here were obtained in individual experiments of 9 minutes duration each. After passing through the quality investigation procedure the obtained time series were partioned into 3 data sets of equal length. The deviations of the statistics among the members of each triplet were within expected statistical errors, except for one experiment which was partly destroyed by amplifier clipping.

Except for Figure (15) all data presented are normalized by scales based on the kinematic viscosity

$$\nu - 202.8 \ 10^{-6} \ m^2/sec$$

and a wall-shear velocity

$$u_\tau - 0.377 \ m/sec$$

The shear velocity was obtained from pressure drop measurements along the pipe axis. Length and time scales can be derived from these in traditional fashion.

The Reynolds number based on mean velocity, pipe diameter and kinematic viscosity was

$$Re - 8750$$

-65-

Figure (15) shows the mean velocity normalized by the center-line velocity as function of the wall-distance normalized by the pipe radius. Entered are the near-wall region measurements performed with hot-splitfilm sensors as well as data obtained with a 0.065" diameter pitot-tube. For comparison some data obtained by Bakewell (1967) in the same facility at almost the same Reynolds number are entered as well. In Figure (16) only the near-wall region is depicted in terms of inner variables. At small values of the normalized wall-distance x_2^+ the data converge nicely to the $u^+ = x_2^+$ line.

The standard deviation of the streamwise velocity fluctuation and the spanwise component are shown in Figure (17). To within experimental error they decrease linearly to zero for small values of x_2^+. The spanwise velocity fluctuations increase monotonously with increasing x_2^+ while the streamwise show the expected maximum at about $x_2^+ = 17$. In Table (4) we compare some characteristics of these data with values found in the literature. In general excellent agreement is found. The streamwise velocity fluctuations as measured by Bakewell (1967) though fall off much more rapidly than our data, although we expected the highest agreements with his values. Our results are more in accordance with results obtained by other researchers.

The results of our measurements for normalized third, fourth and fifth order central moments are shown in Figures (18) through (20). Table (5) and (6) show comparison with the literature for some

significant features in their respective dependencies on the wall-distance x_2^+. The agreement is very satisfactory in all aspects. All higher order central moments with an odd power component in the spanwise velocity component were found to be zero to within acceptable limits.

Spectral measurements are displayed in Figure (21) through (26) for the streamwise and spanwise fluctuating velocity component. We used here the two-sided power spectrum and cyclic frequency, defining the spectrum as Fourier transform in the following way:

$$S_{ij}(f) = \int_{-\infty}^{+\infty} R_{ij}(\tau) \, e^{-2\pi i f \tau} \, d\tau$$

The data agree well with traditional values. Close to the wall the spectra for each velocity component can be unified into a universal spectrum defined as:

$$S_{uni}(f^+) = \frac{S(f)}{y^2 \, f}$$

with the Strouhal number

$$f^+ = \frac{f \, \nu}{u_\tau^2}$$

For the streamwise velocity component Bakewell's (1967) data show that the universal spectrum is applicable up to $x_2^+ = 5$. Our data show this to hold not only for the streamwise component, Figure (25), but for the spanwise component as well, Figure (26). The spectra shown were obtained numerically from the digital time series using a standard FFT-algorithm.

5.2 CORRELATION MEASUREMENTS

All results presented in the following section were obtained by solving the eigenvalue problem with the wave-numbers k_1 (associated with the streamwise direction) and k_3 (associated with the spanwise, wall-parallel coordinate) as parameters.

Hence, we used from our experimentally obtained data only the small portion with zero time-lag $(t-t'=0)$.

The spectral tensor as function of k_1 and k_3 was obtained by first curve-fitting each component of the correlation tensor R_{ij} as function of x_1 and x_3. The analytical functions chosen to represent the correlation tensor were of the form:

$$\text{polynomial}(\ x_1\ x_3)\ *\ e^{-|x|_1/s_1\ -|x|_3/s_3}$$

for $|x_1|>s_1$ and $|x_3|>s_3$ and simple polynomials for small values of x_1 and x_3 with continuity up to the first derivative at $|x_1|=s_1$ and $|x_3|=s_3$.

The polynomial coefficients and the scales s_1 and s_3 are different for each measured component of the correlation tensor and wall-distance and were obtained by least mean square error method. We do not claim any physical significance to this form, it was more by trial and error that we found these functions to reflect the measured data nicely. In addition their Fourier-transform with respect to both wave-numbers can be obtained analytically in general form.

The advantage of using an analytical representation for the correlation tensor is that the problems of missing values and random errors inherent to experimental data are solved elegantly. In addition we avoided taking the Fourier transform with respect to x_1 and x_3 on a low number (7 and 6 respectively) of unequally spaced support points.

Figure (27) to (32) show some of the experimental correlation functions compared with their analytical representations which were the input to the eigenvalue problem. Shown are the correlations as function of the spanwise coordinate with those streamwise spacings as parameter at which measurements were performed. For each of the figures both probes assume identical wall-distance.

5.3 DISTRIBUTION OF EIGENVALUES IN WAVE-NUMBER SPACE

Integrating the bilinear representation of the spectral tensor equation (4.14), over the inhomogeneous, wall-normal coordinate we obtain:

$$\int_{\Omega} S_{ij}(\underline{k}\ x_2)\ dx_2 = \sum_{n} \lambda^{(n)}(\underline{k})$$

The overall energy density (per unit wave-number squared) is represented as the sum of all eigenvalues. In the wave-number space, k_1-k_3, each $\lambda^{(n)}(\underline{k})$ is an even function in both k_1 and k_3. Figure (33) displays the largest eigenvalue (=dominant mode) as a surface in the k_1-k_3-λ space for $k_1 > 0$ and $k_3 > 0$. The first mode is extremely dominant in the low wave-number range in comparison to the next 2

largest eigenvalues. With increasing wave-numbers the first three modes become more and more equal. Figure (34) for $k_3=0$ and (35) for $k_1=0$ show this most clearly.

The higher order eigenmodes show a global maximum at $k_1=k_3=0$, while the dominant mode has its global maximum at $k_1=0$ and $k_3=0.0035$. For each $k_1=$constant the dominant eigenvalue shows such an off-center maximum when considered as function of k_3. This appears as a ridge-like feature in Figure (33). The maximum of this ridge (for fixed k_1) changes only mildly as function of k_1 as shown in Figure (36) but becomes stronger when compared to the same value of k_1 but $k_3=0$, see Figure (37).

We were tempted to associate the wave-number $k_3=0.0035$, at which the global maximum of $\lambda^{(1)}$ lies, with the spacing of two counter-rotating rolls of a single eddy. The centers would be then about $1/(2*0.0035) = 143$ viscous lengths apart which is almost a factor of two larger then the value given by Bakewell (1967). We will resume the discussion of this point later on in this chapter.

The range of wave-numbers taken into consideration for later analysis was bounded upwards by the occurrence of relatively strong negative eigenvalues. Negative eigenvalues appeared practically at all wave-numbers and were already encountered by previous researchers when applying the orthorgonal decomposition scheme to experimental data, see Payne (1966) for example. The negative eigenvalues occured to large extent because of errors in the 2-2 component of the spectral tensor. Its entries are derived from the

measured data by using the incompressiblity condition on the spectral tensor twice, each time integrating from the wall outwards. In Table (7) we show the ratio of the sum of negative eigenvalues to the sum of all eigenvalues, at the same wave-number. For all of the wave-numbers investigated the absolute value of the sum of the negative eigenvalues never exceeded 1% of the maximum of the dominant eigenvalue.

5.4 KINETIC ENERGIES AND SHEAR STRESS OF EIGENMODES

We again may start with the bilinear representation of the spectral tensor in terms of the eigenfunctions. Considering the case of $\underline{k}=\underline{k}'$ and $x_2=x_2'$ in equation (4.14) and integrating over all wave-numbers we obtain the stress tensor:

$$T_{ij}(x_2) = \sum_n \iint_{\underline{k}} \lambda^{(n)} \phi_i^{(n)}(\underline{k}\, x_2)\, \phi_j^{(n)*}(\underline{k}\, x_2)\, d\underline{k} \qquad (5.1)$$

The double integral on the right hand side can be evaluated for each eigenmode using the obtained eigenvalues and eigenfunctions.

In Table (8) we compare the contributions from n=1 (the dominant eigenmode), the sum of n=1 and n=2, and the sum of the first three eigenmodes with the total amount for the three normal stresses (variances) and the wall-parallel shear stress. The remaining components of the stress tensor T_{ij} are identically zero.

The listed values for the variances of the streamwise and spanwise velocity component, $\langle u_1^2 \rangle$ and $\langle u_3^2 \rangle$ respectively, are on

the average 20% lower than the originally measured values, see Figure (36). Principle cause is the leakage effect associated with replacing the integration in equation (5.1) by a finite sum over the low wave-number range to which the analysis of our experimental data had to be restricted. This leakage effect is particularly pronounced for the shear stress which should be about -0.9 at $x_2^+ \approx 40$ where viscous shearing is almost negligible, see Schubauer (1954). Because the shear stress is associated with higher frequencies than the normal stresses (break-up) this stronger deviation was expected. In Figure (38) to (41) the contributions of the first three eigenmodes to the total stresses are displayed on a percentage basis.

For the variance of the three velocity components as well as for the shear stress the first three eigenmodes capture essentially the entire flow field, with the largest deficits occuring close to the wall.

The dominant eigenmode has a streamwise velocity component which represents about 50% of the kinetic energy at the wall, rises to 90% at $x_2^+ \approx 20$ and decreases to 60% at the outer edge of our measurement volume, $x_2^+ \approx 40$, see Figure (38). A similar behavior is observed for the Reynolds shear stress as function of wall-distance, Figure (41). The second and third eigenmode make contributions to the shear stress of varying sign depending on the wall-distance.

The variance of the wall-normal velocity component is comprised to 50% of the first eigenmode and the next two higher modes split the remainder, except close to the wall.

Only about 80% of the variance of the spanwise velocity
component, Figure (40), are are produced by the first three
eigenmodes, decreasing to about 70% at $x_2^+=40$.

In Table (8) the numerical data underlying Figure (38) to (41)
are summerized.

5.5 STREAMWISE INTEGRAL OF DOMINANT EDDY

In this section we assume that in physical space an eddy typical for
the dominant eigenmode can be described as Fourier transform of its
weighted eigenfunctions $\phi_i^{(1)}(x_2 \; \underline{k})$. The weighting function is
assumed to be complex-valued with an amplitude equal to the square
root of its eigenvalue but undetermined phase-factor, see equation
(4.43). The phase-shift function $\Theta(\underline{k})$, as investigated in section
4.4, is an odd function in wave-number k_1 and even function in the
spanwise wave-number k_3 as a result of the requirements for the
typical eddy to be real-valued and symmetric with respect to the
spanwise coordinate.

As explained in section 4.4, we can integrate the equation
describing the velocity field of this eddy over the streamwise
coordinate. The outcome of this integration is independent of the
phase-shift function because of its special form, see equation
(4.45).

In Figure (42) the resulting velocity field is displayed for
$x_3>0$, its mirror image for $x_3<0$ is omitted. The bottom picture
represents the projection of the velocity vector $u_i(x_2 \; x_3)$ onto the

x_2-x_3 plane with the length of the arrows indicating the magnitude of the local velocity vector. Arbitrariness in sign exists and having positive u_2 between the counterrotating rolls is our choice.

The centers of the two rolls, defined by the points of u_2=u_3=0, are 67 viscous length scales apart and located at $x_2^+ \approx 40$, which agrees very well with the values found by Bakewell (1967). Beyond $x_3^+ > 80$ the u_1 component is practically zero indicating that fluid particles move downstream with the local mean velocity for all wall-distances but have a noticable inward velocity component. The fluid is slowly drawn under the roll were it accelerates in spanwise direction but decelerates in streamwise direction under action of the wall friction. As the fluid particles are being pushed upwards in between the rolls they at first maintain there low streamwise velocity leading to large velocity defects with respect to the mean velocity. The velocity defect is largest around $x_2^+ \approx 20$ above which it becomes smaller again, see Figure (42). Notice in Figure (42) the spanwise and wall-normal velocity component are of the same order while the streamwise component is larger by an order of magnitude.

In Figures (43) to (45) the eigenfunctions weighted by the square root of their respective eigenvalues are shown for various wave-numbers k_3 as function of wall-distance x_2^+. For k_1=0 the 1 and 2 component of the eigenfunctions are strictly real-valued while the spanwise velocity component is purely imaginary. For all wave-numbers k_3 the flow is retarded at all wall-distances, with a maximum of retardation at $x_2^+ \approx 20$ for the low wave-numbers. For the

highest wave-number investigated the maximum of retardation lies at $x_2^+ \approx 10$, they are adjusting faster to the local mean velocity.

From Figure (44) and (45) we can easily see that in the x_2-x_3 plane each wave-number contribution constitutes an infinite series of alternately rotating rolls with the distance of their centers from the wall given by the zero crossing of the ϕ_3-component, Figure (45). The spanwise distance between two adjacent rolls is $0.5/k_3$. The two rolls to the left and right of $x_3^+ = 0$ rotate in the same sense as the composite structure in Figure (42) because of the identical sign of ϕ_2 for all wave-numbers k_3 investigated, Figure (44).

In summary, the integrated form of the typical eddy is a result of supercomposition of wave-number components each of which is an infinite series of alternately rotating rolls, their center being about 40 viscous lengths away from the wall at low wave-numbers and about 27 at the highest wave-number investigated. The composite of these contributions, Figure (42), is periodic in the spanwise direction when computed as Fourier series, with a periodicity according to the lowest non-zero wave-number chosen.

5.6 THE UNIVERSAL STRUCTURE OF THE DOMINANT FOURIER MODES

The result of the previous section that the x_1-integrated Fourier modes of the dominant eigenfunctions are counter-rotating rolls at all wave-numbers raises the question whether all Fourier modes independent of the wave numbers k_1 and k_3 have a universal shape.

Under the same conditions as in the previous section concerning symmetry etc. and adding the contributions with $|k_1|$-constant, $|k_3|$-constant from each of the four quadrants in the k_1-k_3 plane, we arrive at a description of the velocity field generated by an individual Fourier mode:

$$f_i(\underline{x}) = \cos(2\pi k_3 x_3) [\ \phi_i^r(x_2\ \underline{k})\ \cos(2\pi k_1 x_1 + \theta)$$

$$-\phi_i^i(x_2\ \underline{k})\ \sin(2\pi k_1 x_1 + \theta)\ ] \tag{5.2}$$

for $i=1,2$ and

$$f_3(\underline{x}) = -\sin(2\pi k_3 x_3) [\ \phi_3^r(x_2\ \underline{k})\ \sin(2\pi k_1 x_1 + \theta)$$

$$+ \phi_3^i(x_2\ \underline{k})\ \cos(2\pi k_1 x_1 + \theta)\ ] \tag{5.3}$$

for the spanwise velocity component, see also equation (4.47). We introduced here $\phi_i^r()$ for the real part and $\phi_i^i()$ for the imaginary part of the eigenfunction under consideration. The undetermined phase function $\theta(\underline{k})$ appears now as a mere shift in the streamwise coordinate, x_1, and is irrelevant and set to zero.

Equations (5.2) and (5.3) represent a velocity field which is periodic in x_1^+ direction with period $1/k_1$ and in the spanwise direction with period $1/k_3$. A single member thereof is represented in Figure (46) in a sequence of cross-sectional cuts taken at successive values of the streamwise coordinate. $k_1 x_1^+ = 0.0$ is the most upstream position showing two counter-rotating rolls with high speed fluid being pushed towards the wall in between them.

Marching downstream (increasing x_1^+) the center of the rolls start to move away from the wall with increasing spanwise velocity beneath their center due to high speed fluid particles being drawn under them from larger wall-distances. For $k_1 x_1^+=0.15$ and 0.20 the velocity field is almost wall-parallel and only on the symmetry line and edges (in x_3^+-direction) a slight vertical motion is descernible. At $k_1 x_1^+=0.25$ the presence of a secondary pair of very weak rolls rotating in the opposite sense to the primary rolls is apparent. As we go further downstream the secondary rolls become more and more pronounced and their centers move away from the wall. The velocity field at $k_1 x_1^+=0.5$ is then finally identical to that at 0.0 but for a sign change. The secondary rolls have become primary and they in turn will generate a pair of rolls rotating then in the same way as at $k_1 x_1^+=0$.

The centers of the rolls are always located at $k_3 x_3^+=\pm 1/4$ as can be seen from equation (5.2), because here the wall-normal velocity component vanishes. The streamwise velocity component is zero also in this plane; in other words, all fluid particles in these two planes move along with the (wall-distance dependent) mean velocity and have only a spanwise velocity component.

From equation (5.3) follows immediately that the spanwise velocity component at $k_3 x_3^+=\pm 1/4$ is zero along a line given by:

$$\phi_3^r(\underline{k}\; x_2) \; \sin(2\pi k_1 x_1) + \phi_3^i(\underline{k}\; x_2) \; \cos(2\pi k_1 x_1) = 0 \tag{5.4}$$

Figure (47) shows this wall-normal location of the center of the rolls (defined by $f_2=f_3=0$) as function of downstream location for a variety of wave-numbers k_1 and k_3. We shifted the x_1^+-origin such that the "root" of the first roll is located at $k_1 x_1^+=0$. The rolls rotating in the opposite direction have their roots at $k_1 x_1^+=0.5$.

At the root, the rolls are first perpendicular to the wall with a stagnation point like flow ahead of it. The rolls bend over rather quickly though in downstream direction and are in physical space almost parallel to the wall. As we can see from Figure (47), the angle between axes of the rolls and the wall changes with the spanwise and streamwise wave-number. We could not detect a simple scaling law concerning this aspect.

The term counter-rotating rolls is somewhat misleading when describing the fundamental block of the Fourier-modes, because one thinks then of the centerlines of the two rolls (defined by $f_2=f_3=0$) being parallel to the local vorticity vector which is far away from the truth. We will discuss this topic in the next section of this chapter. It should be mentioned though, that the local vorticity vector derived from equation (5.2) and (5.3) has only a spanwise component at $x_3^+=0$ (plane of symmetry) and only a streamwise and wall-normal component in the two planes containing the center lines of the two rolls.

In what way, if at all, the two rolls of the Fourier-mode building block connect away from the wall is a matter of conjecture because our measurement volume did not extend far enough away from the wall.

We like to add, that above description of a Fourier mode of the dominant eddy was found, without any exception, at all wave-numbers we investigated numerically.

Although it is very suggestive indeed, that each pair of rolls creates another pair downstream with opposite sense of rotation, a warning is in order. Any type of Fourier mode inherently creates structures with alternating sign and the periodicity in the Fourier modes does not necessarily mean that the composite thereof, the typical eddy in the near-wall region, occurs in such a periodic fashion. In fact, periodicities in either spanwise or streamwise direction should result in "spikes" in the energy density, which is $\lambda^{(1)}(k_1\ k_3)$. Hence, if at all, the weak maximum of the dominant eigenvalue at non-zero k_3 indicates a weak periodicity in the spanwise direction with a period of about 1/0.004=250 viscous length scales, see Figure (36).

5.7 THE TYPICAL EDDY

The big obstacle in defining a composite eddy at this stage is the ambiguity in the absolute phase between the Fourier-modes as exposed in section 4.4. If the absolute phase were known we simply would have to evaluate equation (4.43) for the velocity field $F_i(\underline{x})$ of the dominant eddy.

Even the restrictions placed on the functional form of the phase shift function due to the requirement of real-valuedness and symmetry of the resulting velocity field of the dominant eddy, see equation (4.44), leaves still too much freedom.

Nevertheless we are able to represent in this section a typical eddy which we believe is of importance to the large scale structures present in turbulent boundary layers. The results are displayed in Figure (48) through (52) and to facilitate better understanding some introductory remarks are in order.

The typical eddy in physical space was calculated as a finite sum of its Fourier-modes. The description of its velocity and vorticity field was calculated inside a box extending from the wall to the outer limit of $x_2^+=40$ at which measurements were taken. The length and width of this box is given by the period of the lowest non-zero wave-number in streamwise and spanwise direction, respectively, included in the calculations. As it turns out the typical eddy occupies only a small portion of this box as far as its streamwise and spanwise extend is concerned, indicating that the typical eddy is indeed an isolated structure uncorrelated to its surrounding.

In order to display detailed features of the typical eddy we could zoom in to any desired part of this box. For purpose of orientation the streamwise and spanwise coordinate, x_1^+ and x_3^+, in the Figures (48) through (52) have identical origin which for the spanwise coordinate lies between the counter-rotating rolls of the typical eddy. The figures contain vectorial descriptions of either the velocity or the vorticity field in the plane shown in each particular graph. Displayed are only the two vector components lying in the plane, the component perpendicular to the plane of display is surpressed. The magnitude and direction of the arrows correspond

exactly to the velocity (or vorticity) vector at the location of the tail of the arrow under consideration. In each graph the largest arrow has the same length if measured with a ruler and correponds to the largest velocity (vorticity) vector encountered for that particular graph.

The plane which is perpendicular to the wall and which lies in between the counter-rotating rolls will be referred to as the plane of symmetry. Another plane which lies parallel to this but contains the centerline of the roll at positive x_3^+ is called the centerline plane.

We return now to the problem of the determination of the absolute phase. Writing out equation (4.44) we obtain:

$$\theta(k_1 k_3) = a_{00}k_1 + a_{10} k_1^3 + a_{20} k_1^5 + a_{11}k_1 k_3^2 \cdots \tag{5.5}$$

The linear term represents a mere shift in streamwise direction and is therefor irrelevant; we set $a_{00}=0$.

In a first attempt we set all coefficients in equation (5.5) to zero except a_{10} which we use as parameter to study the effect of the absolute phase.

In Figure (48) we display the velocity field in the symmetry plane for different values of $a_{10}=A$. The four pictures of Figure (48) extend in streamwise direction over the full period of the lowest wave-number of the constituent Fourier-modes. At $A=-3.E+9$ we see a series of eddies of alternating sign with the view box shifted such that the strongest eddy (which draws fluid away from the wall

in between the counter-rotating rolls) appears roughly in the center of each picture. As the parameter A approaches zero the upstream "shadows" start to disappear (their velocities fall beneath a certain threshold) and the downstream "shadows" become weaker. The two cases of A=-1.E+9 and A=+1.E+9 are symmetric in the sense that they produce no upstream and a very weak downstream "shadow" and vice-versa.

At the moment we do not know why the case of zero phase-shift, A=0, produces the most compact form. Small changes in A are certainly possible without affecting the compactness of the structure, but these changes, as well as inclusion of higher order terms in equation (5.5), do not change the principle features of what we will refer to as the typical eddy.

Below we desribe the velocity and vorticity field of the typcial eddy.

A close-up look at the velocity field in the plane of symmetry of the typcial eddy is shown in the top picture of Figure (49) which is followed by a series of six cross-sectional cuts at successive downstream locations. Each of these cross-cuts shows a pair of counter-rotating rolls with their centers (defined by zero wall-normal and spanwise velocity) at increasing wall-distance as we take cuts further downstream. Note that in these cross-cuts we restricted the spanwise viewing area only to a small section around the rolls. Their velocity field decreases rapidly for larger values of the spanwise coordinate.

The strength of such a typical eddy and its sense of rotation are, as explained earlier, not determinable from the orthogonal decomposition procedure itself, and showing a typical eddy with fluid being pushed away from the wall inbetween the counter-rotating rolls is an arbitrary choice.

The two center lines of the rolls are inclined towards the wall by about 5 degrees, except a short region near the upstream "root". They spread slightly in spanwise direction by about 3 degrees, as shown in Figure (50), with increasing wall-distance in downstream direction. We only can estimate the total streamwise extent of the typical eddy from our investigations because of the low maximum wall-distance attained. Figure (49) indicates a value of maybe 800 wall units as a minimum estimate.

Again, we have to emphasize that the center lines of the two rolls as defined as locations of zero velocity are not at all parallel to the local vorticity vector. Figure (51) and (52) depict the vorticity field of the typical eddy. The two figures are identically structured and the vorticity fields shown have the same characteristics, the difference being that they refer to different streamwise locations $x_1^+ \approx 3800$ for Figure (51) and 4020 for Figure (52), respectively.

The spanwise vorticity component is relatively small in the plane containing the centerline of each roll, because here the streamwise and spanwise velocity components vanish and so do their derivatives w.r.t. x_2^+ and x_1^+. The distribution of the wall-normal and spanwise

vorticity component in the centerline plane of the roll rotating clockwise when looking downstream are shown in Figure (51) around the center portion and in Figure (52) around the downstream end of the typical eddy. Close to the wall the vorticity vector is parallel to the wall pointing upstream. It is due solely to the gradient of the negative, spanwise velocity component beneath the rolls center. The magnitude of this streamwise vorticity directly at the wall is zero at either end of the eddy. At a fixed streamwise location this streamwise, negative vortivity component becomes zero as the wall-distance is increased due to the fact that the spanwise velocity has to have a minimum somewhere between wall and center of the roll. Simultaneously, the spanwise gradient of the wall-normal velocity becomes more and more negative as one approaches the roll's center from beneath.

Together with the increase, from negative through zero to positive values of the streamwise vorticity component, we see a steady increase of the wall-normal component with increasing wall-distance, which is entirely due to the spanwise gradient of the streamwise velocity component. (The spanwise velocity component is zero). Above the level of the centerline the resulting vorticity vector is tilted downstream under about 45 degrees, resulting in maximum vortex stretching by the mean velocity profile.

A side-view of the vorticity field in the plane of symmetry is not shown here. For reasons of symmetry of the velocity field the wall-normal and streamwise vorticity component are zero in this

plane. The distribution of the spanwise vorticity as function of wall-distance can be seen easily from the cross-sectional views in Figure (51) and (52).

In these cross-sectional views, the planes containing the roll's centers are indicated by the two arrows at $x_3^+=\pm30$. Vortex lines (lines which are locally parallel to the vorticity vector) appear as closed, concentric ovals.

So far we have discussed only the vorticity field of the typical eddy alone as obtained from the correlation function of the fluctuating velocity field. A more appropriate view which corresponds to a laboratory frame of reference is to superimpose this typical eddy onto the background of the mean-velocity profile which we have done in view (C) of Figure (51) and (52). The vorticity of the mean velocity field has only a spanwise component which is negative in our chosen coordinate system. Hence, close to the wall the vorticity of the typical eddy and that of the mean velocity are counteractive, but reinforce each other at higher wall-distances. The strength of the typical eddy is arbitrary from the point of view of the orthogonal decomposition. In Figure (51) we chose its strength such that the wall-normal gradient of the combined streamwise velocity vanishes at the wall; in Figure (52) the typical eddy is some 20% weaker. It is obvious that regardless of chosen strength the appearing vortex lines have now a strong resemblence to those of a horseshoe vortex.

It has to be pointed out immediately that there is no concentration of these vortex lines present, rather the typical eddy is almost uniform in streamwise direction. Hence, an experimentalist watching a typical eddy being convected along by the mean velocity would not be able to make out the existence of a horseshoe vortex, except at the downstream end of the typical eddy.

Chapter VI

SUMMARY AND CONCLUSIONS

The experimental part of this work consisted of measuring time series of the velocity in the near-wall region of turbulent pipe flow. At a Reynolds number of about 8500 and with the highly viscous glycerine as working fluid the near-wall region could be investigated in detail as close to the wall as 1.25 and as far away as 40 wall-units.

Two hot-splitfilm probes, each measuring the two velocity components parallel to the wall, were moved around independently in all spatial directions. We determined from the measured velocity signals the complete space-time correlation function at discrete values of timelag (6 msec resolution), streamwise spacing $(\Delta x_1^+ = 0, 19, 38, 75, 150, 300, 600)$, spanwise spacing $(\Delta x_3^+ = 0, 8.5, 17, 34, 68, 136)$ and six different wall-distances $(\Delta x_1^+ = 1.25, 2.5, 5, 10, 20, 40)$ for each of the two probes.

Although only four components of the correlation tensor were measured directly the remaining five components and the values of the tensor at negative streamwise and spanwise spacing could be determined utilizing general symmetry properties of the correlation tensor and the incompressibility condition of the flow field.

-87-

Only a small subset of the obtained data, the correlation tensor at zero timelag, was used to decompose the 3-D fluctuating velocity field into a series of eigenfunctions employing Lumley's orthogonal decomposition procedure.

The eigenfunctions corresponding to the largest eigenvalue is associated with the large scale structure of the near-wall region of turbulent boundary layer flow.

The streamwise integral ("average") of the basic building block ("typical" eddy) of this large scale structure can be obtained uniquely to within an arbitrary scaling factor of the strength of its velocity field. In a cross-sectional view this streamwise integral shows a pair of counter-rotating vortices about 65 wall-units apart and about 35 to 40 wall-units above the wall. This picture agrees in all aspects with that obtained by Bakewell (1967) who measured just the streamwise velocity component and applied Lumley's orthogonal decomposition procedure together with a mixing length approximation for the remaining velocity components.

Solving the time-dependent Navier-Stokes equation averaged over small scales which were simulated by an appropriate small-scale stress model Moin (1984) obtained enough numerical data support for the near-wall region of a turbulent channel flow to apply Lumley's orthogonal decomposition to all three velocity components. Variation in the streamwise direction and temporal developmemt were not considered. Again a pair of counter-rotating vortices was obtained, their centers about 65 wall-units apart but located at about 65

wall-units above the wall which is about 50% higher than the value

found by Bakewell (1967) and the present author. We assume that

Moin's data are in error due to inaccurate modelling of the

fine-scale in the near-wall region; this is further substantiated by

Moin's location of the maximum turbulent intensity for the

streamwise velocity which lies almost twice as far away from the

wall as generally accepted.

Lumley's orthogonal decomposition yields unambiguiously also the

contributions of the different eigenmodes to the Reynolds stress

$<u_1 u_2>$ as well as to the variances of all fluctuating velocity

components. The percentage contributions of the first three

eigenmodes as function of wall-distance are displayed in Figure (38)

to (41) and show that the first eigenmode represents between 50 and

90% of all stresses.

Because Lumley's orthogonal decomposition reduces to the

classical Fourier decomposition with a continous spectrum for the

homogeneous coordinates (streamwise and spanwise direction) only

these Fouriercomponents themselves are uniquely determined. The

velocity field associated with an indiviual Fouriermode is of course

complex valued but by summing up the four modes for each of which

the absolute values of their streamwise and spanwise wave-numbers

are equal, a real-valued velocity field is obtained. This property

is not trivial but a consequence of the requirement of

real-valuedness of the composite typical eddy in connection with the

fact that the eigenfunctions are complex-valued functions of

wall-distance, while their phase relation is just a function of wave-number.

The velocity fields of such composite Fouriermodes were found to be geometrically similar and can best be described as counter-rotating rolls originating upstream at the wall. Their centerlines, defined as the location of zero spanwise and wall-normal velocity, point in streamwise direction, their spanwise separation is inversely proportional to the spanwise wave-number and their distance from the wall increases at the upstream end upruptly from $x_2^+=0$ to 5-10 and then linearly until they vanish through the top of our measurement domain at $x_2^+=40$. The angle between wall and centerlines for the linear part depends strongly on the spanwise and streamwise wave-number, Figure (47).

In order to obtain the velocity field of the typical eddy in physical space the contributions of the composite Fouriermodes have to be summed up. Their magnitude was determined using the "shot-noise" effect expansion which is due to Rice (1944), their phase relation being unobtainable from second order statistics. We could show furthermore, that within the domain of the shot-noise expansion, there does not exist a description of a typical eddy and its distribution of strength in space and time which represents all third order statistics (bi-spectrum, Rosenblatt (1966)) of the random coefficients associated with the dominant eigenmode. Hence, even higher order statistics will not allow us to determine a typical eddy and its occurence statistic uniquely, rather, the

description of its velocity field depends on which aspects of the bi-spectrum, for example, are to be reflected truthfully.

Nevertheless, requirements of real-valuedness and symmetry of the typical eddy in spanwise direction place such a severe restriction on the functional form of the phase-relation among the composite Fouriermodes that we could easily calculate the velocity fields of eddies resulting from different phase-relationships and investigate its influence.

To our surprise the assumption of zero phase lead to the most compact form of the velocity field. The typical eddy occupied then only a small fraction of the computational box. Any introduction of a moderate phase-shift among the Fouriermodes lead immediately to an attenuation of this eddy (without changing its geometric shape) and the occurence of weak shadow eddies of opposite sign. Small changes in the phase-relationship did not cause any changes in the basic features of the typical eddy.

It comes to no surprise that the thus found typical eddy is in shape and form very similar to its constituents, a pair of counterrotating rolls with the centerlines about 60 wall-units apart spreading very slightly in downstream direction. The centerlines rise almost perpendicular from the wall at the upstream end to about $x_2^+ = 5$ and continue to rise linearly forming an angle of about 5 degrees with the wall. The centerlines leave the measurement domain $(x_2^+ = 40)$ about 350 wall-units downstream of their root at the wall, definite conclusions about how much larger the typcial eddy is cannot be drawn from our investigation.

We have to emphasize that the two centerlines of the typical eddy are by no means vorticity lines, the vorticity field being of rather complicated form even in the centerline planes, see Figure (51) and (52).

If the above typical eddy is superimposed on the mean velocity profile the resulting vorticity lines in a cross-sectional view resemble those of a horseshoe vortex. Because the typical eddy varies only gradually in streamwise direction no concentration of vortex lines occurs which would make this feature apparent to the experimentalist. Only at the downstream end of the typical eddy a horseshoe vortex will become visible.

Inside the boundary layer though individual eddies of the dominant mode occur in various size, strength and shape with inhomogeneities in the streamwise direction as evidenced by flow visualization studies, see Kline et.al. (1967) for example. Such local inhomogeneities might often resemble horseshoe vortices and it is at this point a matter of conjecture whether such inhomogeneities are always self-healing or often react in a self-enhancing way leading to the formation of separate indiviual horseshoe vortices.

As far as the here employed orthogonal decomposition scheme is concerned, structures of the elongated roller type and individual horseshoe vortices belong to the same class differing only in magnitude and phase-relation of its Fouriermodes. It is the extremely slow attenuation of the streamwise velocity fluctuation with increasing streamwise spacing which identifies the elongated roller type eddy as the most prevalent structure.

There are numerous experimental studies which in one way or other confirm our findings using methods different from those employed in this study.

Blackwelder and Eckelmann (1979) used a quadrant analysis on their measurements of the wall-gradient of the streamwise and spanwise velocity component. Measuring both velocity components simultaneously at two points, which were at the same streamwise location but separated in spanwise direction, they inferred the presence of counter-rotating streamwise vortices pumping fluid away from the wall and thus creating a low-speed streak in between them. These streamwise vortices were in the average 50 wall-units apart and had a streamwise extent of more than a thousand wall-units which they inferred from correlation measurements of the streamwise velocity component and motion pictures provided by Oldaker and Tiederman (1977). Utilizing the same detection scheme as already employed by Blackwelder and Kaplan (1978) the authors used a conditional averaging technique to associate the presence of the low-speed streaks with the classical bursting phenomenon. High-speed fluid coming in from the outer region randomly disturbs and even interrupts the pumping action of the streamwise vortices. Blackwelder and Kaplan (1976) had already found that on the average a strong inflexional profile of the streamwise velocity develops similar to an isolated two-dimensional free shear layer with subsequent oscillation and finally chaotic motion (break-up).

Head and Bandyopadhyay (1981) concluded from their flow visualization and hot-wire experiments on a zero-pressure gradient turbulent boundary layer that the large scale structure encompassing the entire boundary layer can be described as a random ensemble of horseshoe vortices at low and hair-pin vortices a high Reynolds numbers. These vortices always originate at and growing out from the wall and the spanwise spacing of their legs being draged along parallel to the wall is about 100 wall-units independent of Reynolds number. Looking at the near-wall region they found evidence of elongated, counter-rotating streamwise vortex motion and they speculate that these vortices might be the origin of their hairpins.

Smith and Schwartz (1983) used a unique two-camera video flow visualization system observing counter-rotating vortices in the near-wall region of a turbulent boundary layer. They generated "time-lines" by means of pulsed hydrogen bubble wires lying parallel to the wall and perpendicular to the mean flow. The bubble lines were followed in simultaneous top and head-on view showing clearly the three-dimensional distortion of the "time-lines" corresponding to the action of counter-rotating rolls pumping slow-speed fluid away from the wall. They did not have enough data support to quantify any average scales of the motion.

We would like to conclude this chapter by mentioning the work of Clark and Markland (1971). They conducted a hydrogen bubble wire flow visualization experiment in the near-wall region of an open water channel. Their observations lead them to propose as the

dominant structure pairs of counter-rotating, streamwise oriented rolls with an average spacing of about 100 wall-units. At the upstream end these rolls started at about $y^+ = 7$ and formed an angle with the wall of 3 to 7 degrees having a total streamwise extend of 450 wall-units. They observed these structures travelling downstream and being progressively stretched until they decayed.

Chapter VII

RECOMMENDATIONS

In this chapter we would like to make some comments concerning the experimental as well as the analytical side of this study.

The evaluation of the velocity measurements was greatly hampered by two circumstances. The air-bubble problem in the facility as well as our decision to measure with uncalibrated hot-splitfilm probes required a much larger investment of time and computer resources than originally anticipated.

We did not specifically investigate the problem of probe interference. The experiences of Eckelmann (1978) indicate though that some attention should be devoted to this problem in any measurement of space-time correlation functions. Judging the accuracy of our results was futhermore hampered by the fact that we used (for economical reasons) the incompressibility condition to determine missing components of the correlation tensor, giving away the opportunity to use incompressibility as a consistency check on the measured data.

Concerning the application of Lumley's proper orthogonal decomposition scheme we like to raise three questions which we think should be addressed in future investigations. One is the influence of the cut-off of the measured domain at some chosen wall-distance.

-96-

How much would the eigenfunctions change quantitatively in the already investigated domain if the measurements were extended to larger wall-distances, apart from the trivial normalization ?

A second question is more fundamental in nature. In the present study we chose to decompose the fluctuating velocity field in terms of eigenfunctions associated with the correlation tensor of the fluctuating velocity components. Because these eigenfunctions are not orthogonal to the mean velocity profile a decomposition of the correlation tensor plus mean velocity profile will result in a different set of eigenfunctions. Its dominant eigenfunction will probably resemble strongly the picture we obtained by superimposing the typical eddy onto the mean velocity profile. But the sense of rotation would now be fixed because the streamwise velocity component of this new dominant eigenmode has to be always positive. Apart from this, the question arises of course, which set of eigenfunctions is dynamically more significant.

As the third problem we would like to address the inclusion of time as a additional independent variable. The decomposition procedure applied in this study amounts to investigating an ensemble of statistical realizations in which each member can be interpreted as a single snapshot taken of the three dimensional instantaneous flow field. Because of the found similarity of all Fouriermodes of the dominant eigenmode it is highly probable that the temporal development of the dominant eigenmode can be fully described in terms of the already found Fourier-modes.

REFERENCES

Bakewell,H.P., 1967 <u>Viscous</u> <u>Sublayer</u> <u>and</u> <u>Adjacent</u> <u>Wall</u> <u>Region</u> <u>in</u> <u>Turbulent</u> <u>Pipe</u> <u>Flow</u>, The Physics of Fluids, Vol.10-9, pp 1880-1889.

Blackwelder,R.F., and Eckelmann,H., 1979 <u>Streamwise</u> <u>Vortices</u> <u>Associated</u> <u>with</u> <u>the</u> <u>Bursting</u> <u>Phenomenon</u>. Journal of Fluid Mechanics, Vol.94-3, pp 577-594.

Blackwelder,R.F., and Kaplan,R.E., 1976 <u>On</u> <u>the</u> <u>Wall</u> <u>Structure</u> <u>of</u> <u>the</u> <u>Turbulent</u> <u>Boundary</u> <u>Layer</u>. Journal of Fluid Mechanics, Vol.76-1, pp 89-112.

Blinco,P.H. and Sandborn,V.A., 1973 <u>Use</u> <u>of</u> <u>the</u> <u>Split-film</u> <u>Sensor</u> <u>to</u> <u>Measure</u> <u>Turbulence</u> <u>in</u> <u>Water</u> <u>Near</u> <u>a</u> <u>Wall</u>, 3. Symposium on Turbulence in Liquids, University of Missouri-Rolla 1973, pp 403-413.

Brodkey,R.S., 1978 <u>Flow</u> <u>Visualization</u> <u>and</u> <u>Simultaneous</u> <u>Anemometry</u> <u>Studies</u> <u>of</u> <u>Turbulent</u> <u>Shear</u> <u>Flows</u>. AFOSR/Lehigh University Workshop, Bethlehem PA , November 1978

Clark,J.A., 1968 <u>A</u> <u>Study</u> <u>of</u> <u>Incompressible</u> <u>Turbulent</u> <u>Boundary</u> <u>Layers</u> <u>in</u> <u>Channel</u> <u>Flow</u>, ASME-Transaction, Journal of Basic Engineering, vol. 90-2, pp 455-468.

Clark,J.A., and Markland,E., 1971 <u>Flow</u> <u>Visualization</u> <u>in</u> <u>Turbulent</u> <u>Boundary</u> <u>Layers</u>. Journal of the Hydraulics Division, ASCE , HY-10 , pp 1653-1663.

Comte-Bellot,G., 1963 <u>Contribution</u> <u>a</u> <u>l'Etude</u> <u>de</u> <u>la</u> <u>Turbulence</u> <u>de</u> <u>Conduite</u>, Ph.D. Thesis, L'Universite' de Grenoble.

Corino,E.R., and Brodkey,R.S., 1969 <u>A</u> <u>Visual</u> <u>Investigation</u> <u>of</u> <u>the</u> <u>Wall</u> <u>Region</u> <u>in</u> <u>Turbulent</u> <u>Flow</u>. Journal of Fluid Mechanics, Vol.37-1, pp 1-30.

Eckelmann,H., 1978 <u>The</u> <u>Structure</u> <u>of</u> <u>Turbulence</u> <u>in</u> <u>the</u> <u>Near-Wall</u> <u>Region</u>, AFOSR/Lehigh University Workshop, Bethlehem PA , November 1978

Goldshtik,M.A., 1982 <u>Structural</u> <u>Turbulence</u>, Institute of Thermophysics, Novosibirsk 1982.

Hasselmann,K., Munk,W., and MacDonald,G., 1962 Bispectra of Ocean Waves, Proceedings of Symposium of Timeseries Analysis, Brown University, pp 125-139.

Head,M.R., and Bandyopadhyay,P., 1981 New Aspects of Turbulent Boundary Layer Structure. Journal of Fluid Mechanics, Vol.107, pp 297-338.

Hussain,A.K.M.F., 1983 Coherent Structures - Reality and Myth The Physics of Fluids, Vol.26-10, pp 2816-2850.

Kim,H.T., Kline,S.J., and Reynolds,W.C., 1971 The Production of Turbulence Near a Smooth Wall in a Turbulent Boundary Layer. Journal of Fluid Mechanics, Vol.50-1, pp 133-160.

Kline,S.J., Reynolds,W.C., Schraub,F.A., and Runstadler,P.W. 1967 The Structure of Turbulent Boundary Layers. Journal of Fluid Mechanics, Vol.30, pp 741-773.

Kreplin,H.-P., and Eckelmann,H., 1979 Behavior of the Three Fluctuating Velocity Components in the Wall-region of a Turbulent Channel Flow, The Physics of Fluids, Vol.22-7, pp 1233-1239.

Kutateladze,S.S., and Khabakhpasheva,E.M., 1977 Experimental Investigation of the Structure of Near-wall Turbulence and Viscous Sublayer, Symposium on Turbulent Shear Flows, The Pennsylvania State University, pp 17.13-17.22.

Laufer,J.L., 1954 The Structure of Turbulence in Fully Developed Pipe Flow, NACA-Report 1174, 1954 Vol.40.

Lemmerman,L.A., 1976 Extracted Large Eddy Structure of Flat-Plate Turbulent Boundary Layer. Ph.D. thesis, University of Texas at Arlington, December 1976.

Lumley,J.L., 1967 The Structure of Inhomogeneous Turbulent Flows, Atmospheric Turbulence and Radio Wave Probagation, Moscow 1967.

Lumley,J.L., 1970 Stochastic Tools in Turbulence, Academic Press, 1970.

Moin,P., 1984 Probing Turbulence via Large Eddy Simulation, AIAA 22. Aerospace Science Meeting, Reno Nevada.

Oldaker,D.K., and Tiederman,W.G., 1977 Spatial Structure of the Viscous Sublayer in Drag-Reducing Channel Flows. The Physics of Fluids, Vol.20-10, pp S133-S144.

Olin,J.G., and Kiland,R.B., 1970 Split-film Anemometer Sensors for Three-dimensional Velocity Vector Measurements, Symposium on Aircraft Wake Turbulence, Seattle Washington, Sept. 1970.

Otnes,R.K., 1968 An Elementary Design Procedure for Digital Filters, IEEE Trans. on Audio and Electroacoustic, Vol. AU-16 No.3, pp 330-335.

Payne,F.R., 1966 Large Eddy Structure of a Turbulent Wake, Ph.D. Thesis, The Pennsylvania State University.

Rao,K.N., Narasimha,R. and Narayanan,M.A., 1971 The Bursting Phenomenon in a Turbulent Boundary Layer. Journal of Fluid Mechanics, Vol.48, pp 339-353.

Rice,S.O., 1944 Mathematical Analysis of Random Noise, Bell System Technical Journal, Vol.23 , 1944 , pp. 282-332.

Rosenblatt,M., 1966 Computation and Interpretation of k-th Order Spectra, Spectral Analysis of Timeseries. Wiley 1966, pp 153-188.

Sabot,J., and Comte-Bellot,G., 1976 Intermittency of Coherent Structures in the Core-Region of Fully Developed Pipe Flow. Journal of Fluid Mechanics, Vol.74-4, pp 767-796.

Schubauer,G.B., 1954 Turbulent Processes as Observed in a Boundary Layer and Pipe, Journal of Applied Physics, Vol.25 No.1, pp 188-196.

Smith,C.R., 1984 A Synthesized Model of the Near-Wall Behavior in Turbulent Boundary Layers. Proceeding of the 8th Symposium on Turbulence, University of Missouri-Rolla, 1984.

Smith,C.R., and Schwartz,S.P., 1983 Observation of Streamwise Rotation in the Near-Wall Region of a Turbulent Boundary Layer. The Physics of Fluids, Vol.26-3, pp 641-652.

Ueda,H., and Hinze,J.O., 1975 Fine-Structure Turbulence in the Wall-Region of a Turbulent Boundary Layer, Journal of Fluid Mechanics, vol.67 , pp 125-142.

Wallace,J.M., 1982 On the Structure of Bounded Turbulent Shear Flow - A Personal View. Developments in theoretical and applied mechanics. Volume XI, edited by Chung and Karr.

Wallace,J.M., Eckelmann,H., and Brodkey,R.S., 1972 The Wall-region in Turbulent Shear Flow, Journal of Fluid Mechanics, vol.54-1 , pp 39-48.

TABLE 1

Operating conditions of experimental facility

Working Fluid		Glycerine, 2.2% Water
Operating Temperature	T	34.85 ±0.1°C
Fluid Density	ρ	1246 kg/m^3
Pipe Diameter	D	0.285 m/sec
Mean Velocity	U_{mean}	6.63m/sec
Reynolds Number	Re	8750
Wall Shear Stress	τ_w	177 N/m^2
Friction Velocity	U_τ	0.377 m/sec
Viscous Length	$l_\tau = \nu/U_\tau$	0.538 mm

TABLE 2

Physical properties of glycerine at 34.85°C

Kinematic Viscosity	ν	202.5*10^{-6} m^2/sec
Fluid Density	ρ	1246 kg/m^3
Specific Heat Capacity	c_p	2430 Nm/(kg °C)
Thermal Conductivity	λ	0.280 N/(sec °C)
Thermal Diffusivity	α	0.25*10^{-8} m^2/sec
Prandtl-Number	Pr	2340

TABLE 3

Physical data of typical hot-splitfilm sensor

Sensor Diameter	D_s	0.153 mm
Length of Hot-film	L_s	0.254 mm
Thickness of Hot-film		0.001 mm
Electric Resistance	R	6-8 Ohm
Temp. Gradient of R		$1/R * \partial R / \partial T = 0.002\ 1/°C$
Substrate Material		Fused Quartz
Density of Substrate	ρ_s	2100 kg/m^3
Heat capacity	C_{ps}	$1.65 * 10^6$ Nm/(m^3 °C)
Thermal Conductivity	λ_s	1.38 W/(m °C)
Thermal Diffusivity	α_s	$8.36 * 10^{-7}$ m^2/sec

TABLE 4

Comparison for second order central moments

	$(u'/u\tau)/y^+$ $y^+=0$	$(u'/u\tau)$ max	Location of max	$u'/u\tau$ $y^+=40$	$(w'/u\tau)/y^+$ $y^+=0$	$w'/u\tau$ $y^+=4$
present (1985) Re=8750	0.325	2.9	16	2.34	0.161	1.20
Bakewell (1967) Re=8700	0.30	2.6	15	1.64	-	-
Clark (1968) Re=15200	0.40	3.3	13.5	2.40	0.2	-
Kreplin (1979) Re=7700	0.25	2.85	13	-	0.065	1.20
Kutateladze(1977) Re=21000	0.30	2.78	17.7	2.60	0.14	-
Laufer (1954) Re=5000	0.30	2.60	17	2.41	-	1.25
Ueda (1975) Re=11450	0.28	2.65	16	2.10	-	-

TABLE 5

Comparison for third order central moments

	$S(y^+)$ $y^+=0$	Location of S=0	$S(y^+)$ $y^+=40$
present	0.90	14.3	-0.40
Ueda	0.80	16.7	-0.40
Kreplin	1.00	12	-0.50

TABLE 6

Comparison for fourth order central moments

	K_u $y^+=0$	K_u min	Location of K_u/min	K_u $y^+=40$	K_w $y^+=0$	K_w $y^+=40$
present	4.0	2.24	12	2.8	6.	3.25
Kreplin	4.5	2.25	12	2.9	5.5	3.

TABLE 7

Magnitudes of negative eigenvalues

For each wave-number the sum of the negative eigenvalues
is divided by the sum of all eigenvalues.

K_3	K_1 -->> 0.	.0003	.0005	.0008	.001	.0013	.0015	.002	.003
0.0000	0.00	0.00	-0.01	-0.03	-0.09	-0.41	-0.86	-1.15	-0.93
0.0005	0.00	0.00	-0.01	-0.03	-0.08	-0.33	-0.68	-0.92	-0.78
0.0010	0.00	0.00	-0.01	-0.03	-0.06	-0.18	-0.35	-0.49	-0.48
0.0020	0.00	0.00	-0.01	-0.03	-0.04	-0.06	-0.07	-0.07	-0.10
0.0030	0.00	0.00	-0.02	-0.05	-0.06	-0.05	-0.04	-0.02	-0.03
0.0040	-0.01	-0.01	-0.03	-0.05	-0.05	-0.04	-0.02	-0.01	-0.01
0.0050	-0.01	-0.01	-0.03	-0.04	-0.03	-0.02	-0.01	0.00	-0.01
0.0060	-0.01	-0.01	-0.02	-0.02	-0.02	-0.01	0.00	0.00	0.00
0.0070	0.00	-0.01	-0.02	-0.02	-0.01	-0.01	0.00	0.00	0.00
0.0080	-0.01	-0.01	-0.02	-0.02	-0.02	-0.01	-0.01	0.00	-0.01
0.0090	-0.01	-0.01	-0.03	-0.04	-0.04	-0.02	-0.01	-0.01	-0.01
0.0100	-0.01	-0.02	-0.04	-0.06	-0.05	-0.04	-0.02	-0.01	-0.01
0.0110	-0.02	-0.04	-0.07	-0.08	-0.07	-0.05	-0.03	-0.01	-0.01
0.0120	-0.04	-0.06	-0.10	-0.12	-0.10	-0.07	-0.04	-0.02	-0.02
0.0130	-0.06	-0.09	-0.15	-0.17	-0.13	-0.09	-0.06	-0.03	-0.02
0.0140	-0.09	-0.12	-0.20	-0.23	-0.17	-0.11	-0.08	-0.04	-0.03
0.0150	-0.11	-0.15	-0.26	-0.29	-0.21	-0.14	-0.09	-0.05	-0.04
0.0160	-0.13	-0.18	-0.31	-0.35	-0.24	-0.16	-0.11	-0.06	-0.06

TABLE 8

Contributions to Reynolds stresses from first 3 eigenmodes

Streamwise velocity component, $< u_1^2 >$

Y+	total	(1)	(1)+(2)	(1)..(3)
1.25	0.143	0.069	0.100	0.125
2.50	0.563	0.291	0.388	0.489
5.00	2.039	1.228	1.597	1.856
9.99	5.379	4.156	4.878	5.272
19.95	6.457	6.010	6.195	6.337
39.75	4.056	2.482	3.826	4.029

Wall-normal velocity component, $< u_2^2 >$

Y+	total	(1)	(1)+(2)	(1)..(3)
1.25	0.000	0.000	0.000	0.000
2.50	0.000	0.000	0.000	0.000
5.00	0.003	0.001	0.002	0.002
9.99	0.024	0.012	0.016	0.021
19.95	0.126	0.069	0.096	0.119
39.75	0.297	0.165	0.247	0.300

Spanwise velocity component, $< u_3^2 >$

Y+	total	(1)	(1)+(2)	(1)..(3)
1.25	0.019	0.010	0.012	0.015
2.50	0.069	0.035	0.042	0.052
5.00	0.219	0.114	0.134	0.163
9.99	0.516	0.288	0.319	0.388
19.95	0.747	0.392	0.463	0.605
39.75	0.739	0.209	0.318	0.457

Shearstress $< u_1 u_2 >$

Y+	total	(1)	(1)+(2)	(1)..(3)
1.25	-0.001	0.000	-0.001	-0.001
2.50	-0.006	-0.003	-0.004	-0.005
5.00	-0.045	-0.027	-0.034	-0.039
9.99	-0.231	-0.181	-0.196	-0.218
19.95	-0.540	-0.529	-0.525	-0.510
39.75	-0.491	-0.381	-0.518	-0.479
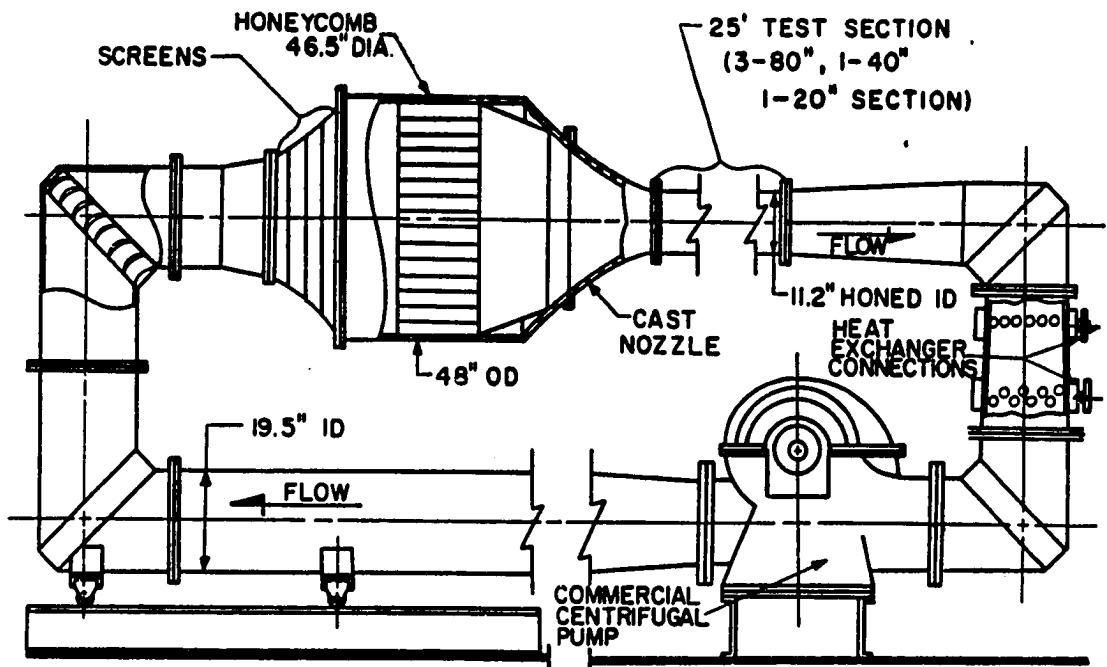
Figure 1: Schematic view of test facility.
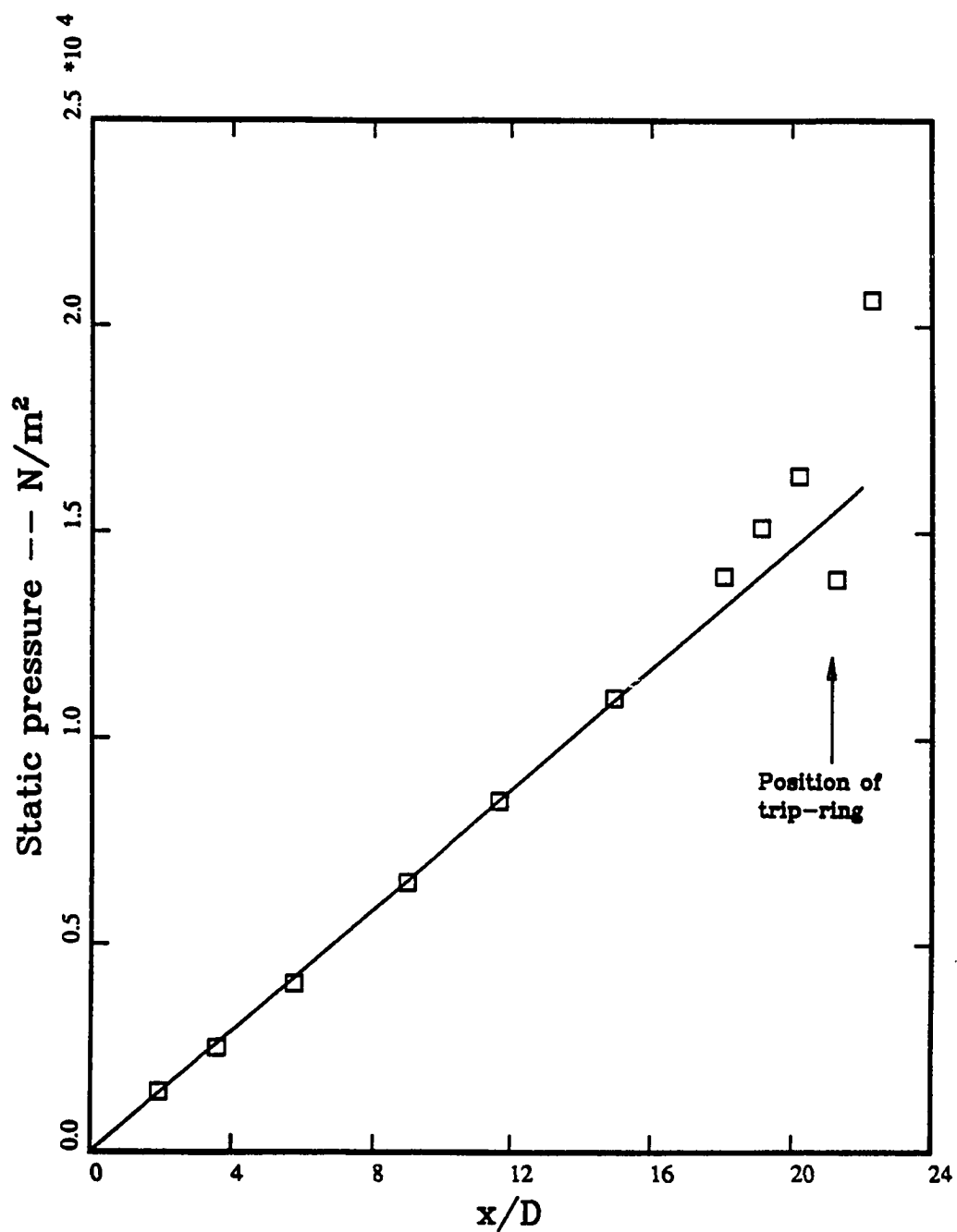
Figure 2: Pressure distribution upstream of
the test section (at origin)
D = pipe—diameter
Symbols=measured points
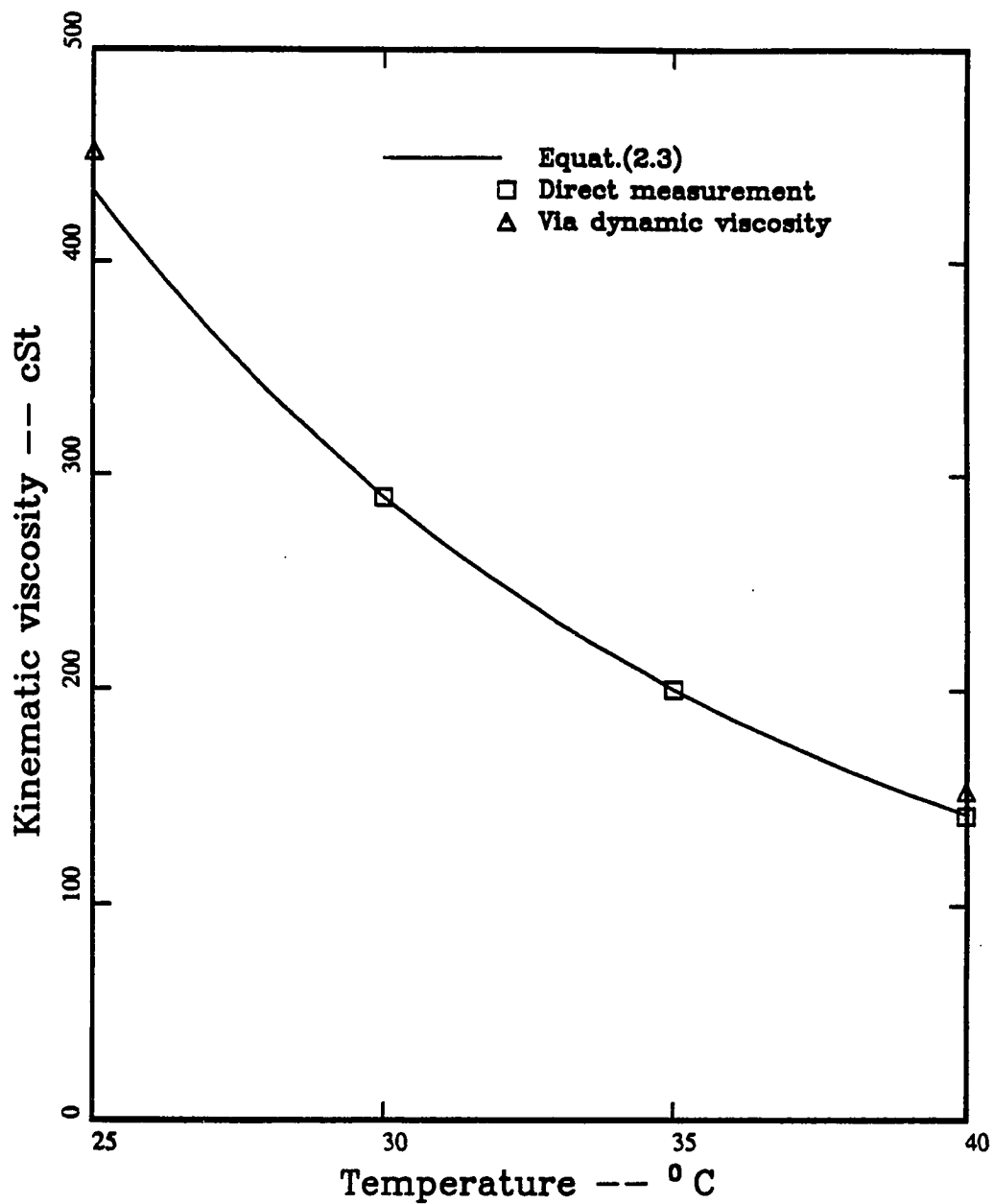
Figure 3: Kinematic viscosity of glycerine
as function of temperature.
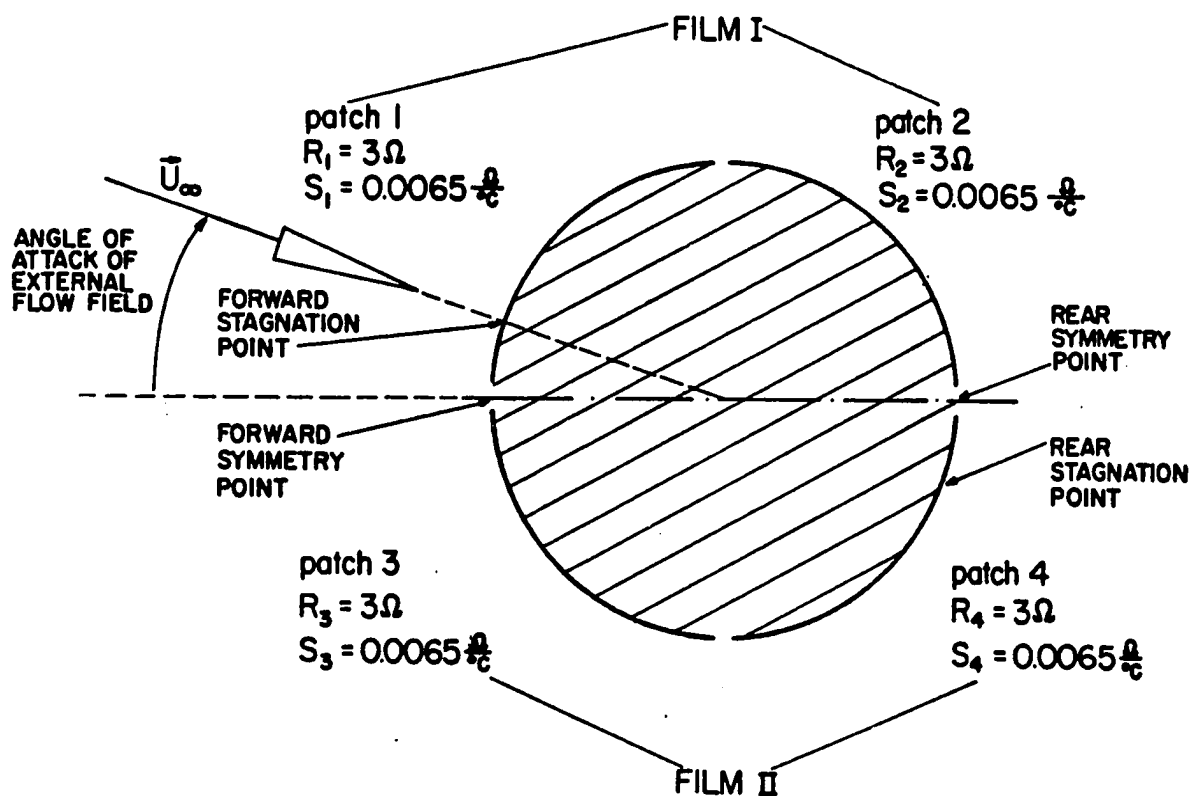
Figure 4: Cross-sectional view of a
hot split-film sensor.
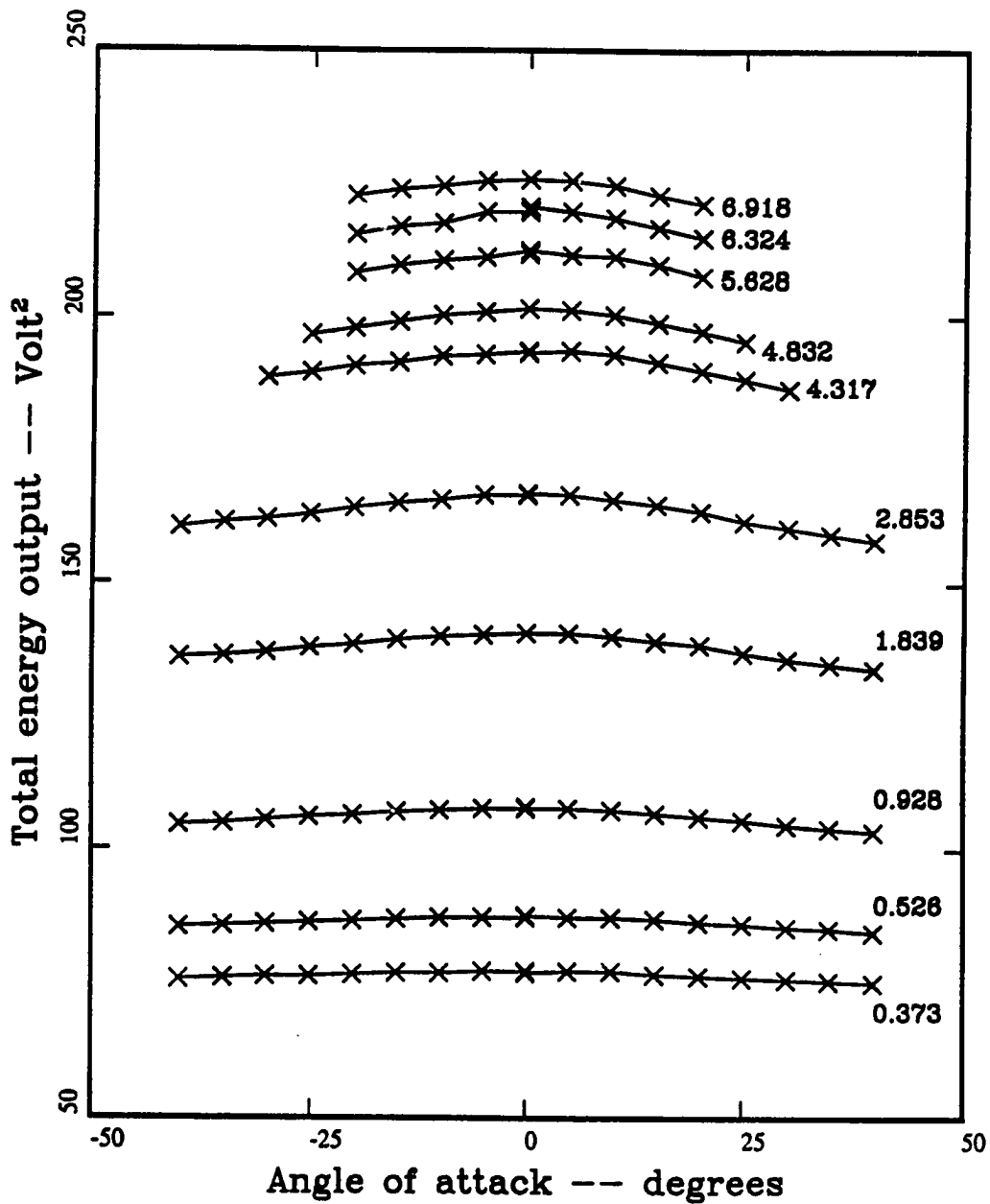
Figure 5: Total energy output of sensor versus angle of attack. Parameter is the effective velocity with values (m/sec) as indicated. × = measured values.
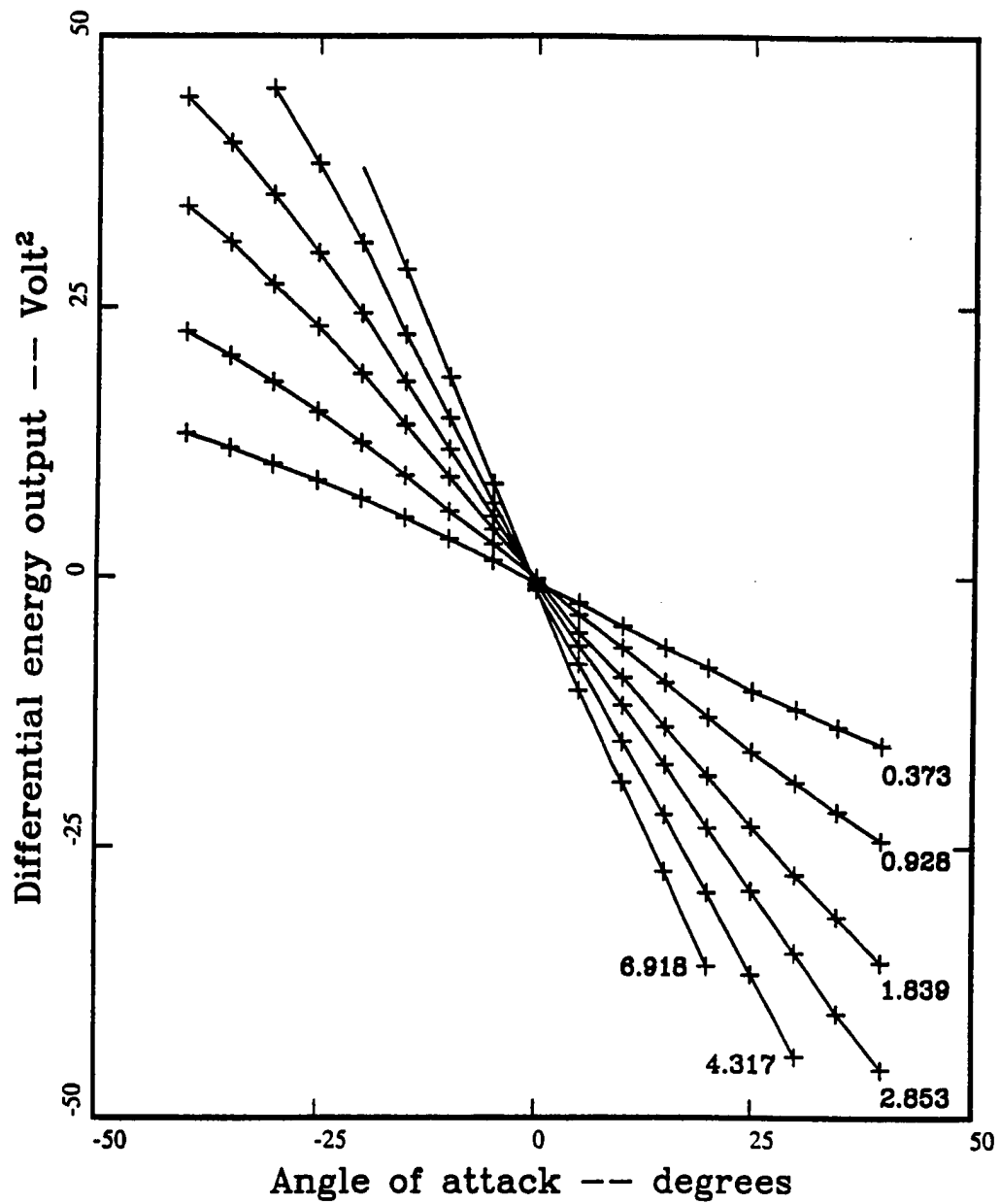
Figure 6: Differential energy output of sensor versus
angle of attack. Parameter is the
effective velocity with values (m/sec)
as indicated. + = measured values.
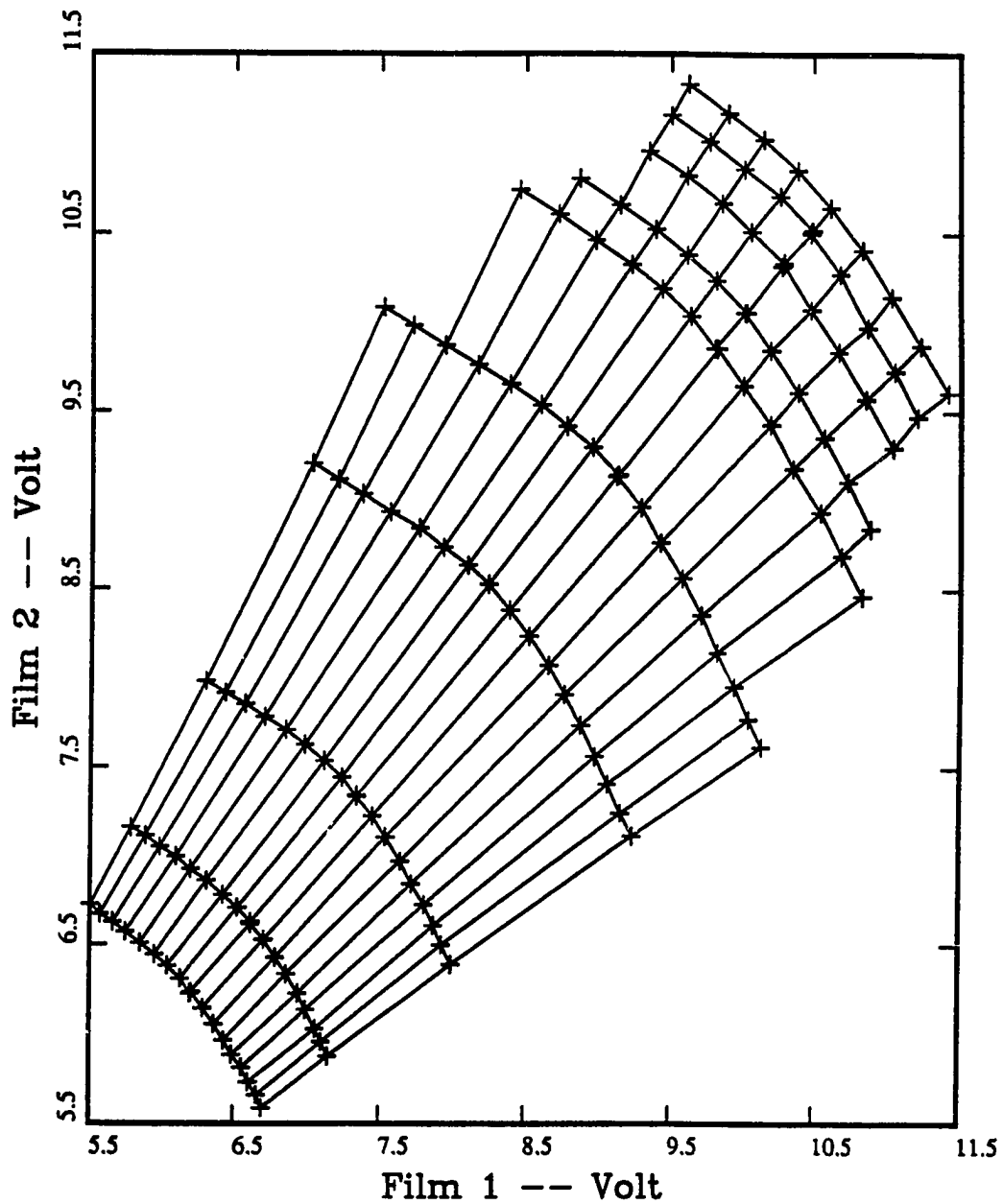
Figure 7: Energy output of both hot—films of
a single hot split—film sensor.
Radial lines = constant angle of attack
Circular lines = constant effective velocity
+ = measured points
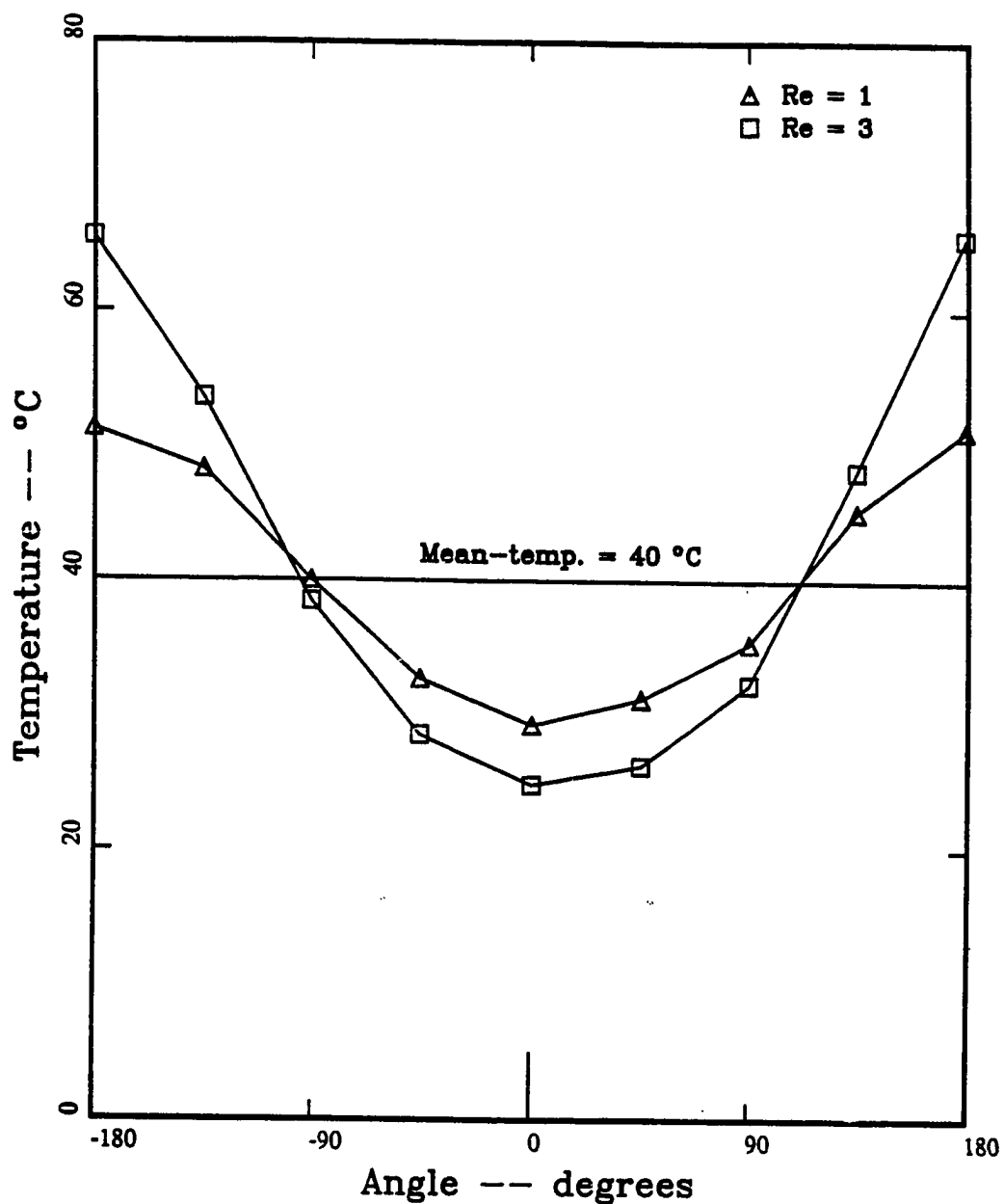
Figure 8: Circumferential steady-state temperature distribution around hot split-film sensor, obtained with 2-D computer model. Angle = 0 = forward stagnation point.
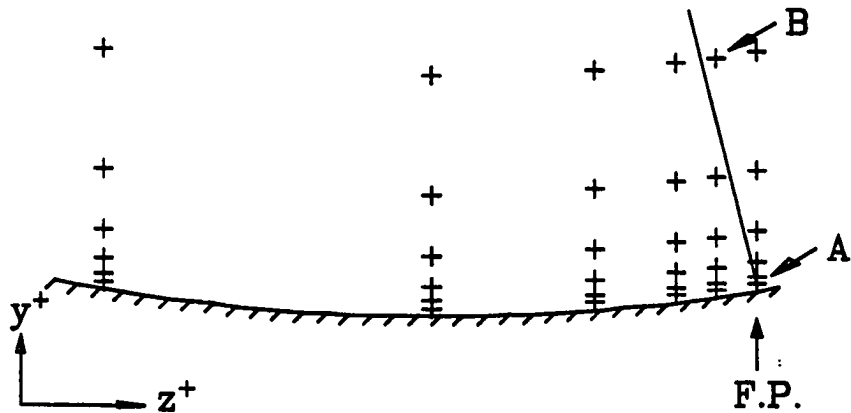
Figure 9: Probe positions in plane normal to flow and wall. The fixed probe assumes positions indicated by the crosses in the column pointed at by the arrow F.P. The movable probe assumes positions at all crosses.
In terms of inner variables the probe spacings are approximately:

$$y^+ : \quad 1.25 \quad 2.5 \quad 5.0 \quad 10. \quad 20. \quad 40.$$
$$z^+ : \quad 0 \quad 8.5 \quad 17 \quad 34 \quad 68 \quad 136$$

The plane of motion ot the movable probe is downstream of the line of motion of the fixed probe with spacings:

$$x^+: \quad 0 \quad 19 \quad 38 \quad 75 \quad 150 \quad 300 \quad 600$$
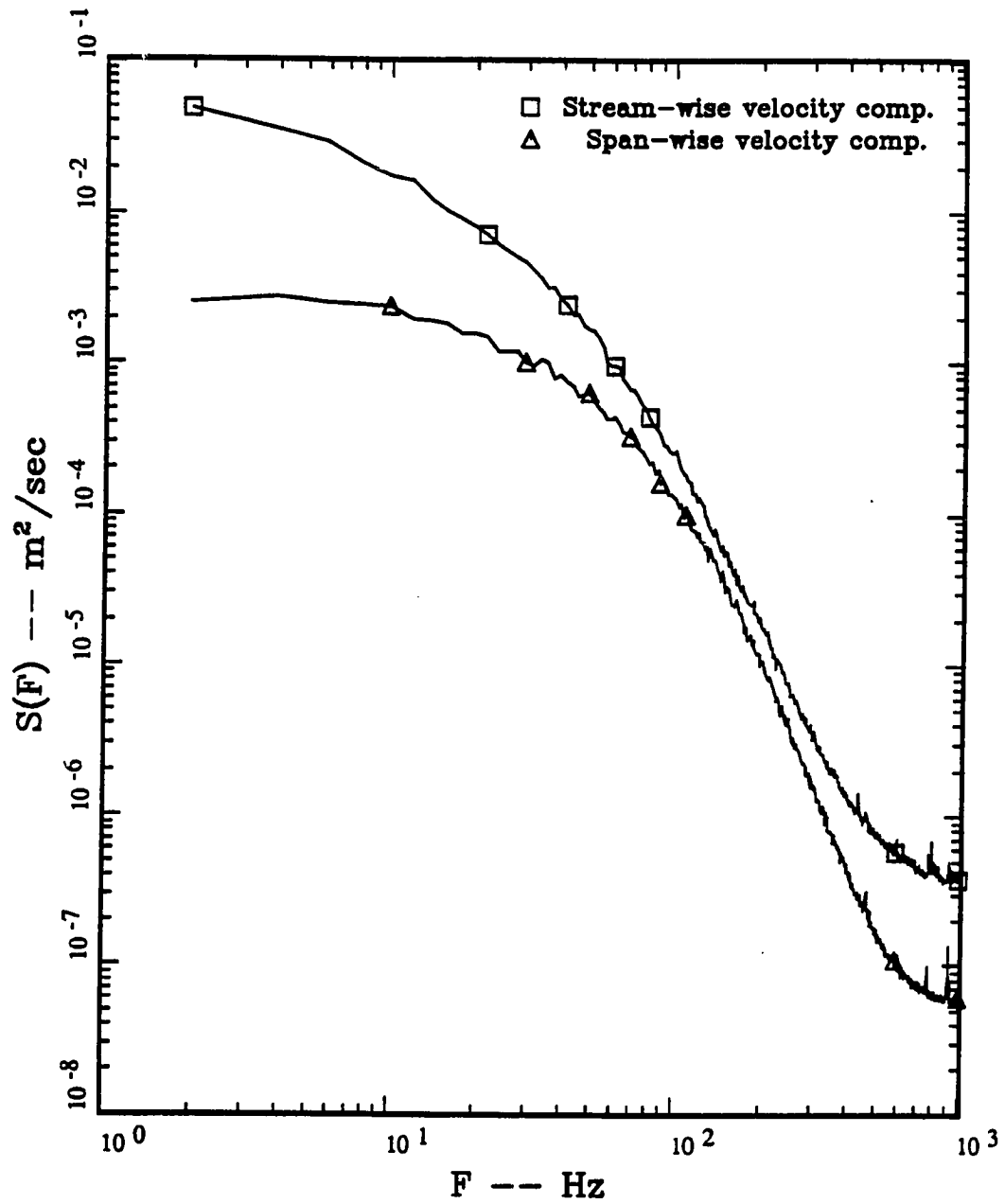
Figure 10: Power spectrum.
Full frequency content.
Wall-distance $y^+ = 20$.
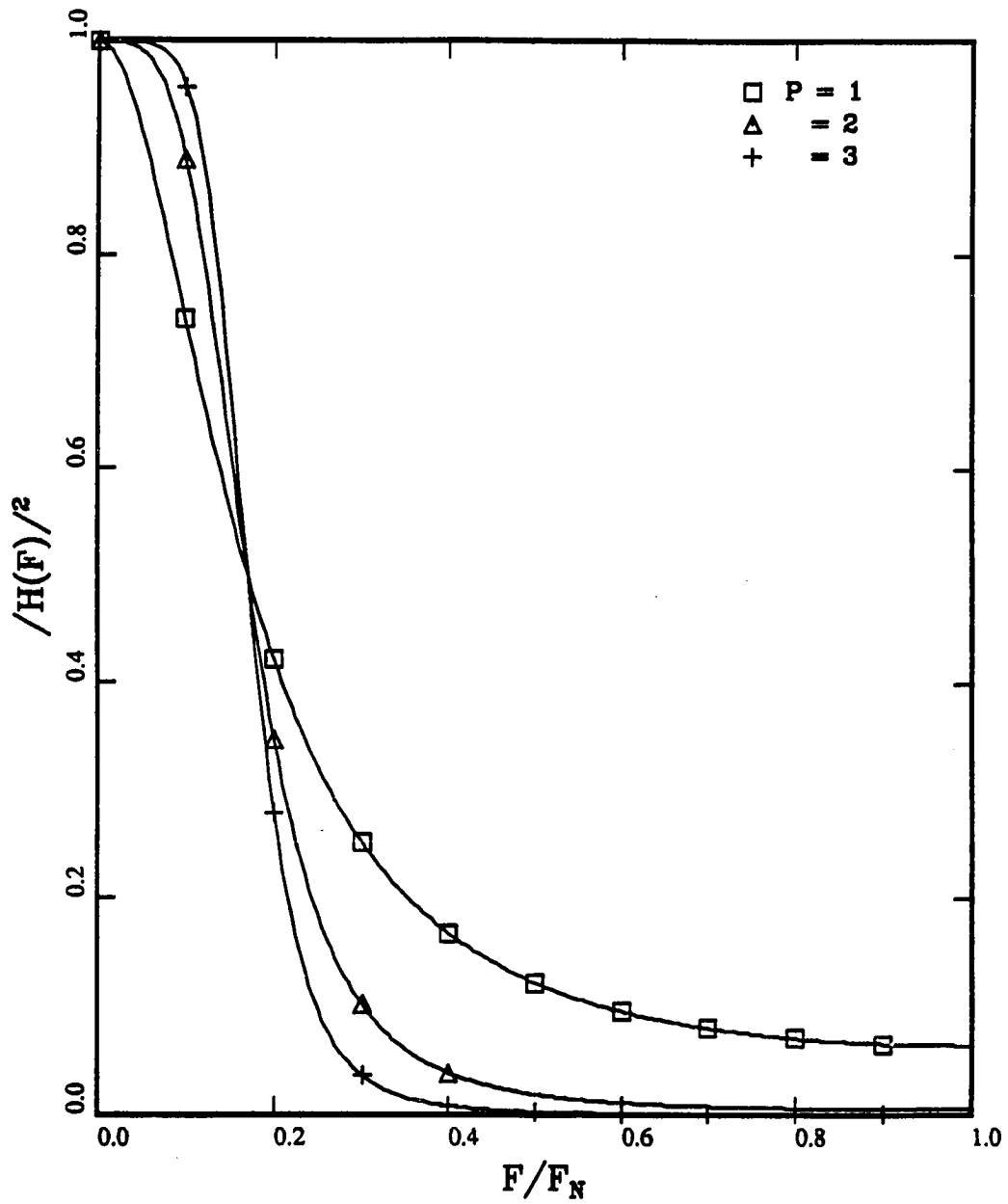
Figure 11: Square of frequency−transfer function
of sine−filter.
Half−power = cut−off frequency = 0.167
P = degree of filter, see equation (3.4).
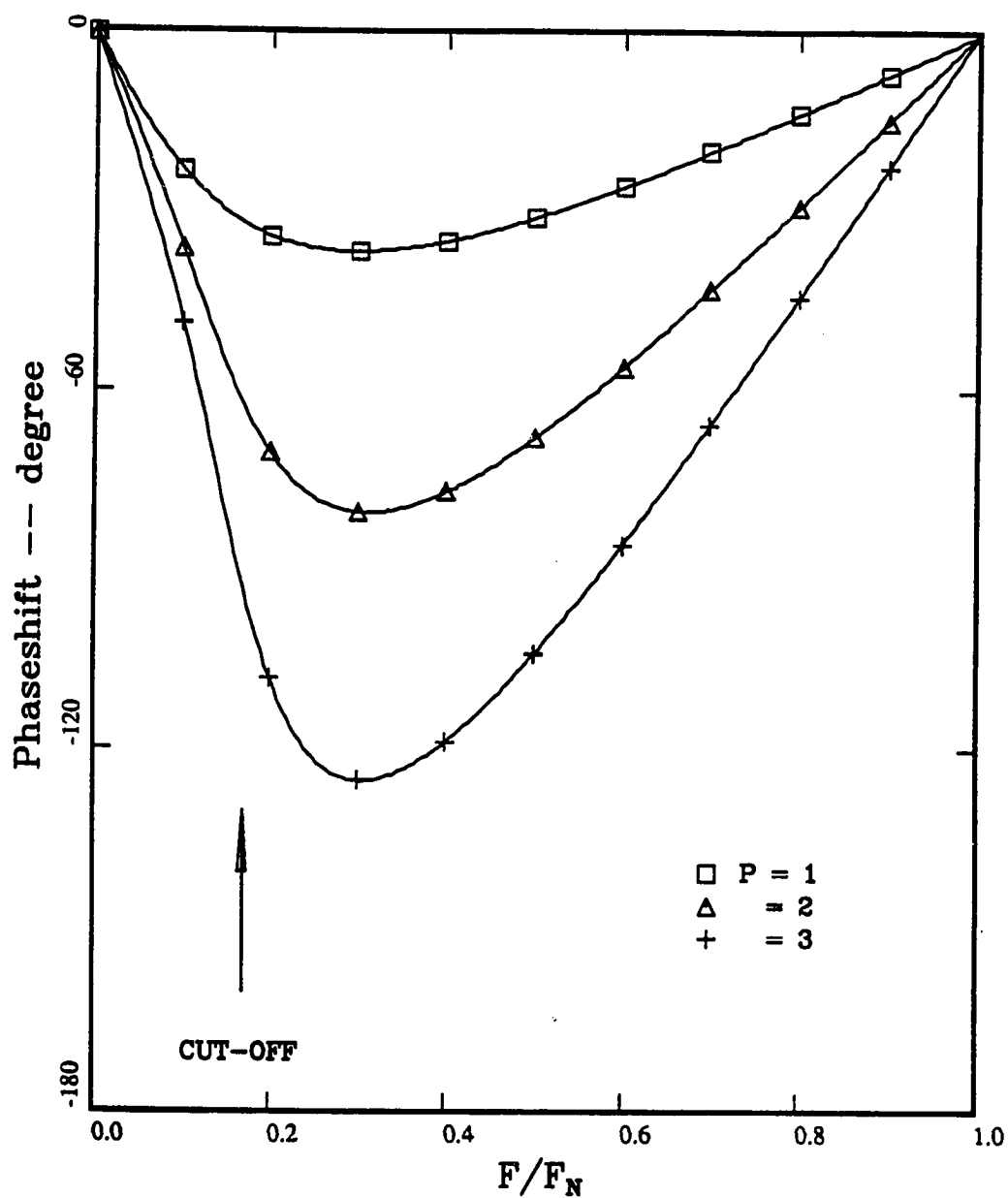
Figure 12: Phase-shift characteristics of sine-filter.
Half-power = cut-off frequency = 0.167
P = degree of filter, see equation (3.4).
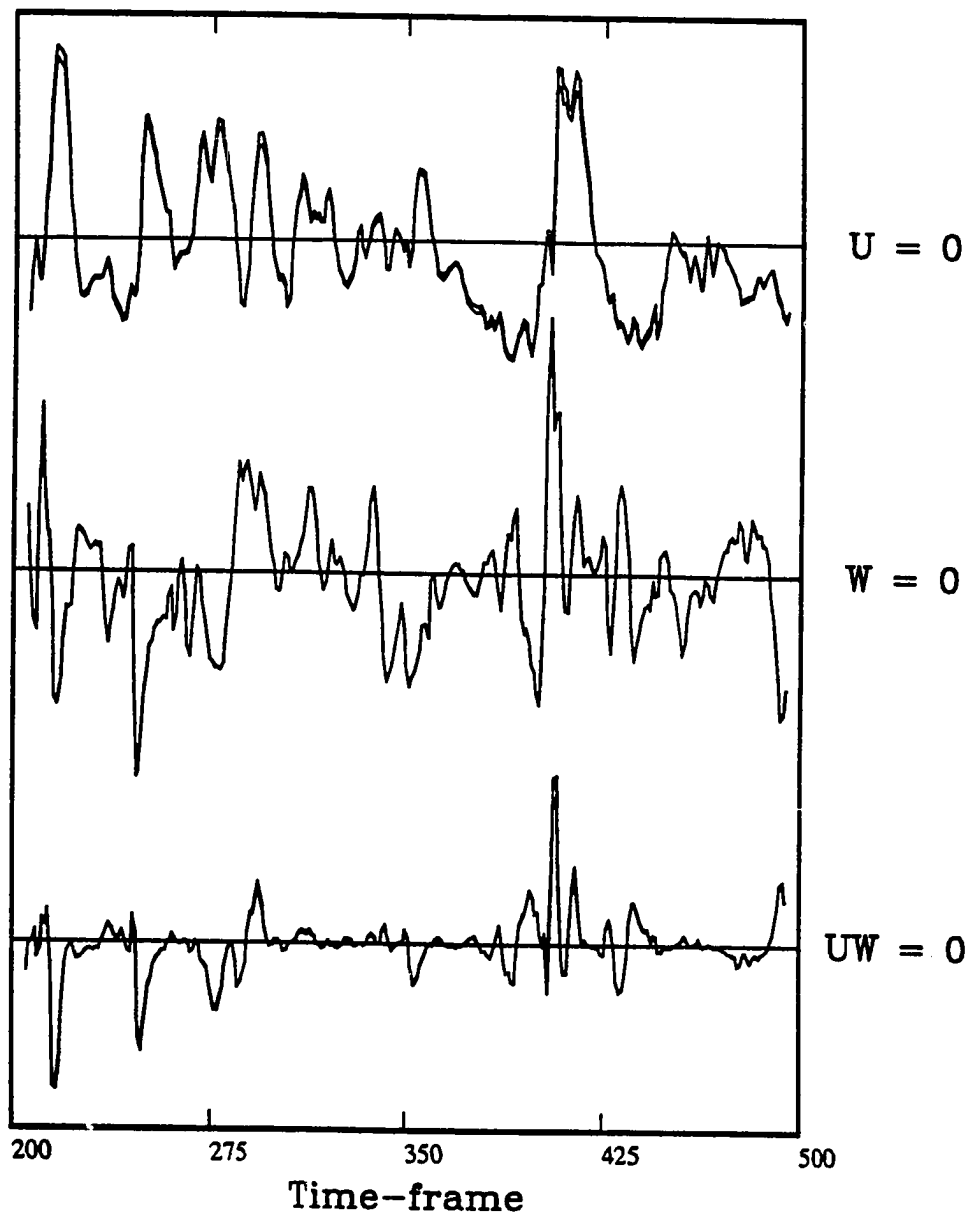
Figure 13: Comparison of time-series.
Inverse versus direct calibration.
U = streamwise, W = spanwise velocity.
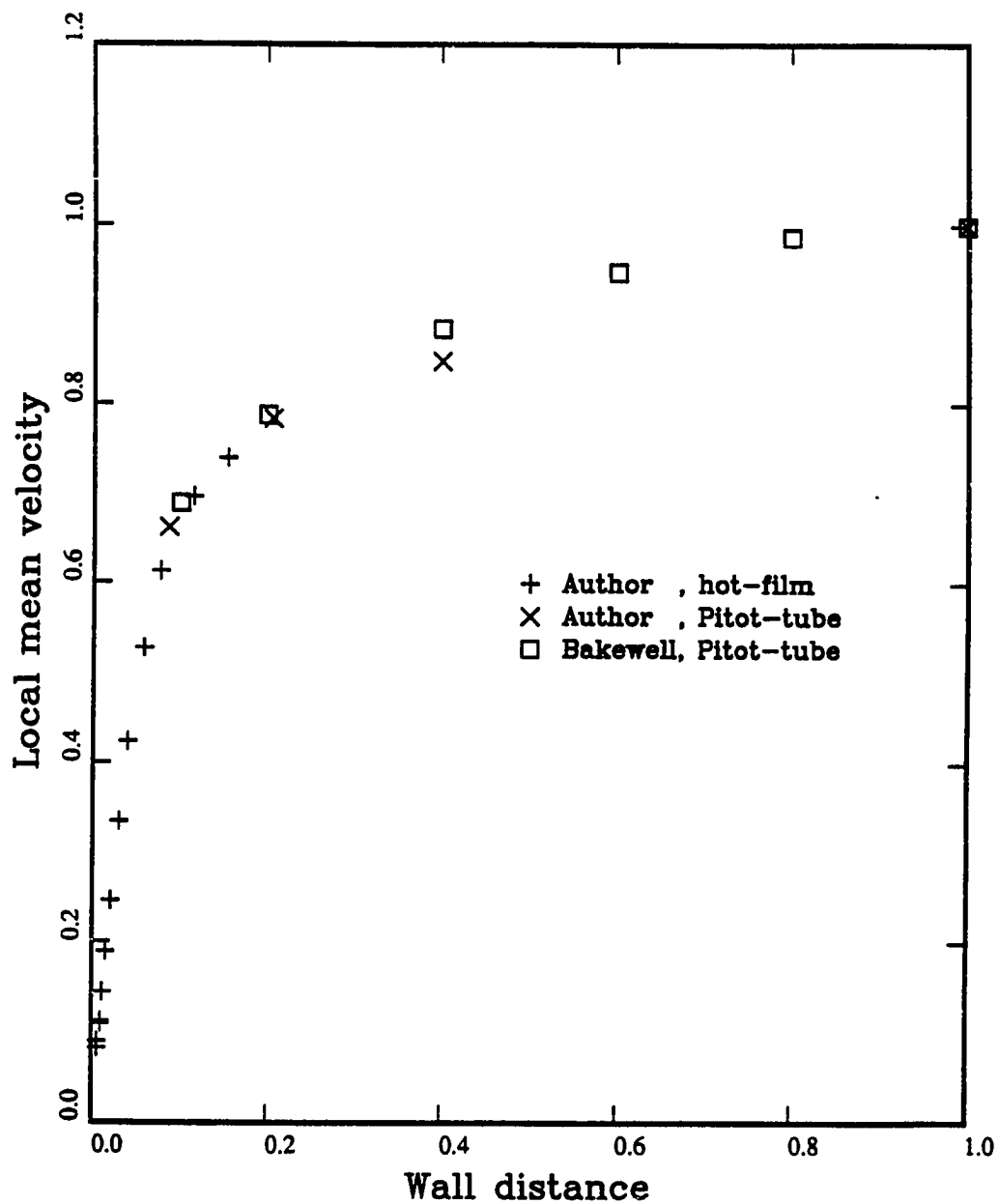
Figure 15: Mean velocity distribution across pipe. The velocity is normalized by the center line velocity = 8.06 m/sec, the wall distance by the pipe radius = 147.25 mm
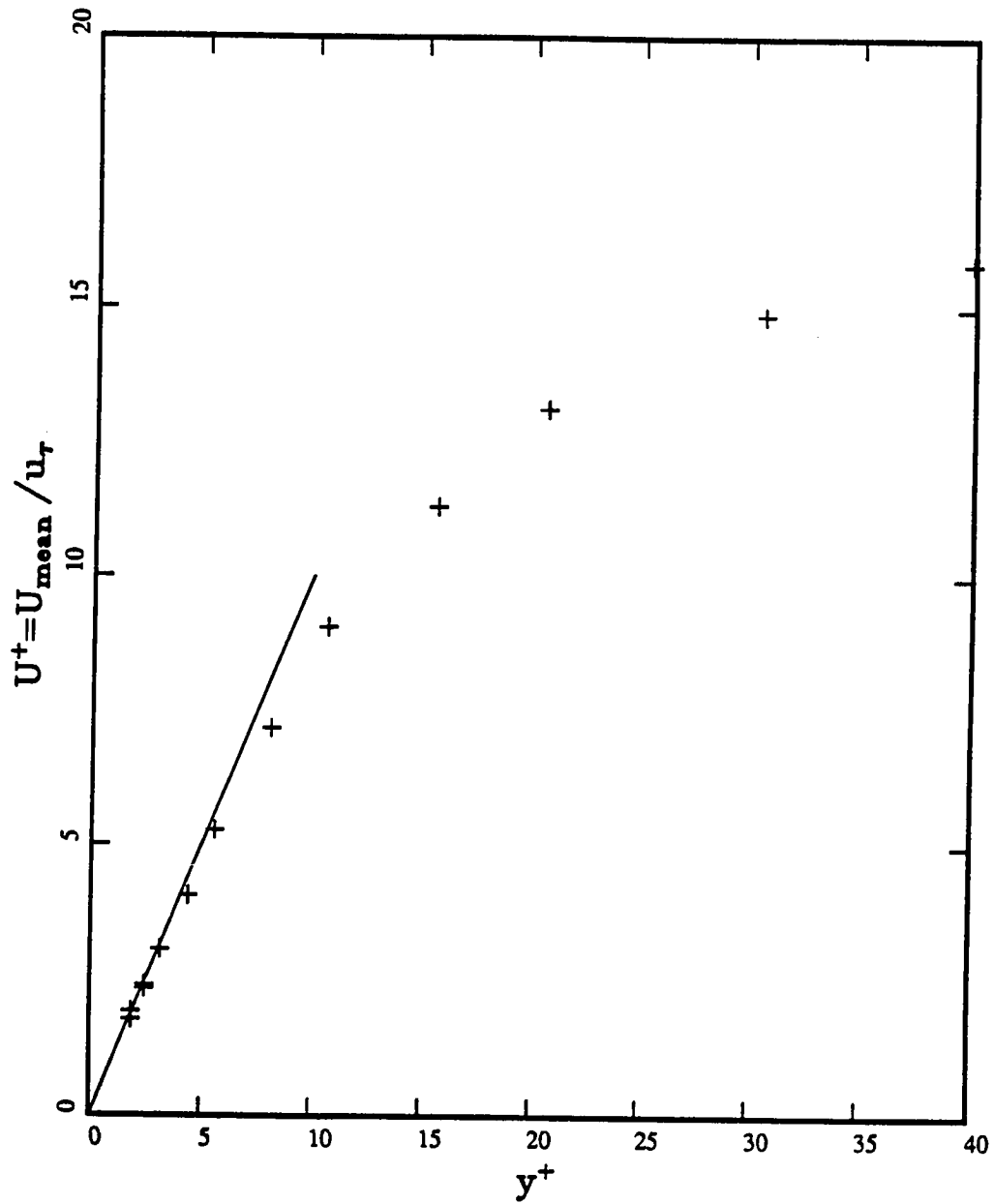
Figure 16: Mean velocity distribution in the near—wall region. Velocity and wall distance are normalized by inner variables. $U^+=y^+$ is entered for comparison.
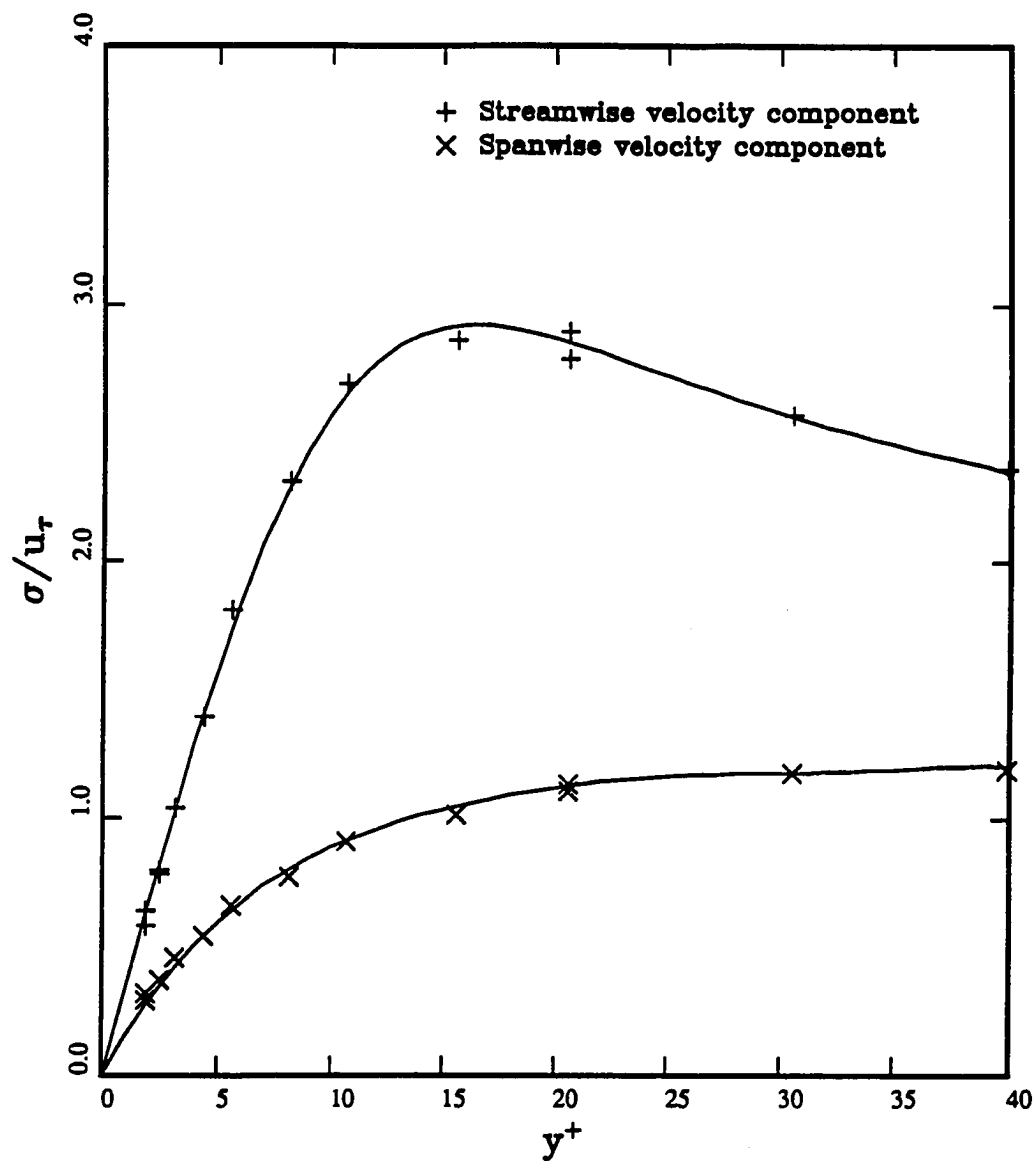
Figure 17: Standard deviations of velocity fluctuations as function of wall–distance.
Symbols represent measured values, the curves are least mean square fits used as input to the inverse calibaration scheme.
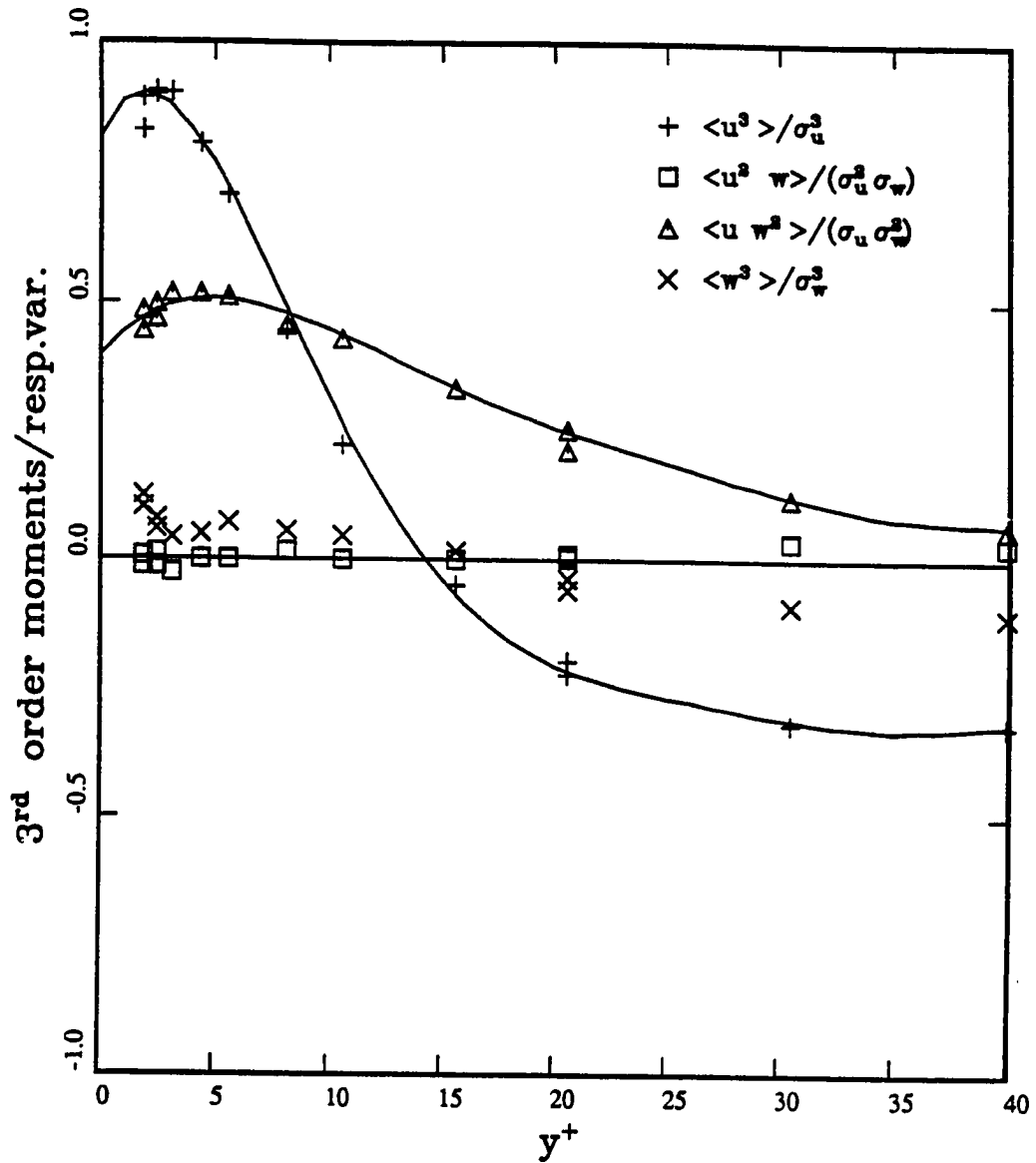
Figure 18: 3rd order moments of velocity fluctuations as function of wall–distance.
Symbols represent measured values, the curves are least mean square fits used as input to the inverse calibration scheme.
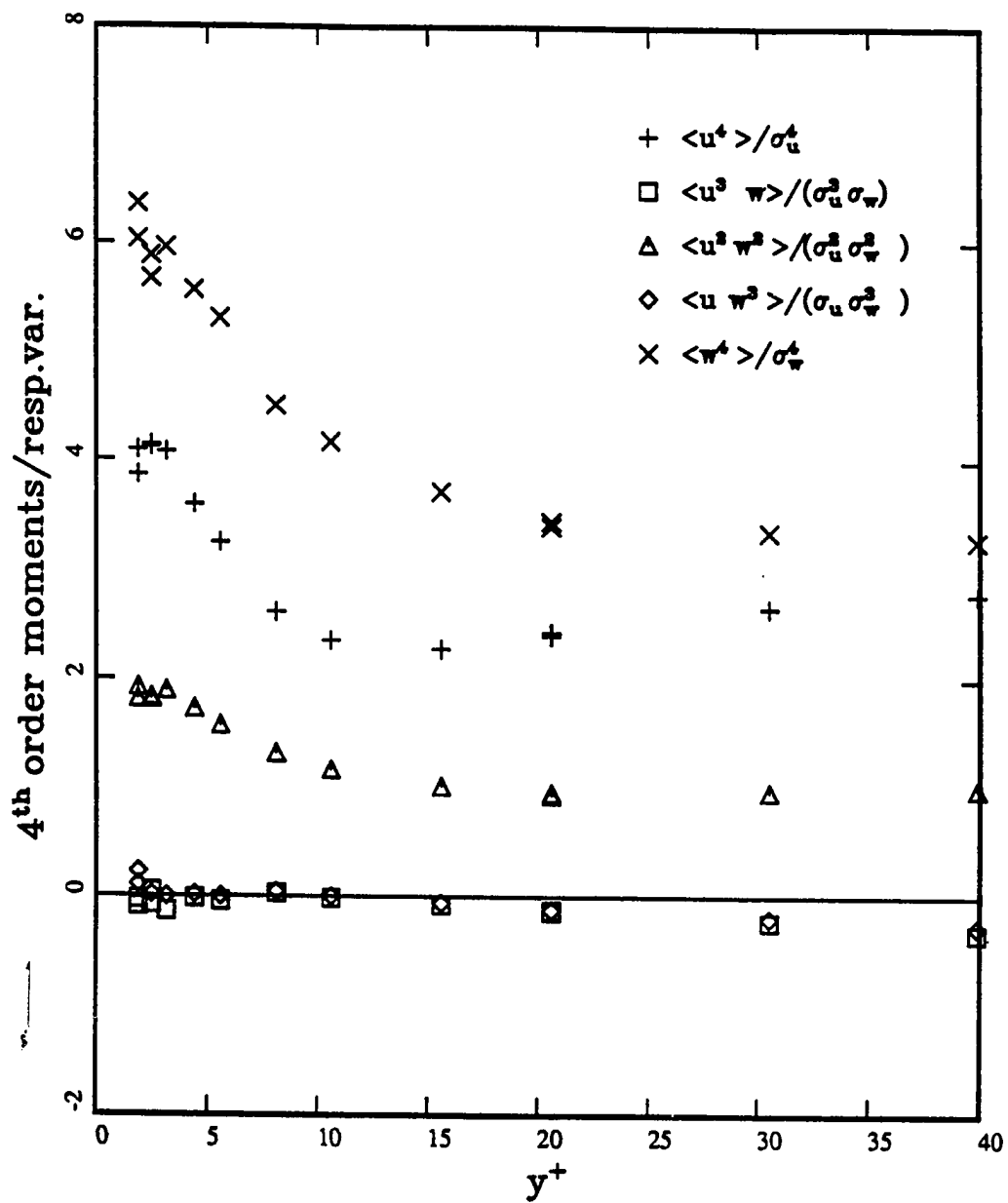
Figure 19: Fourth order central moments of the velocity fluctuations. Symbols represent measured values.
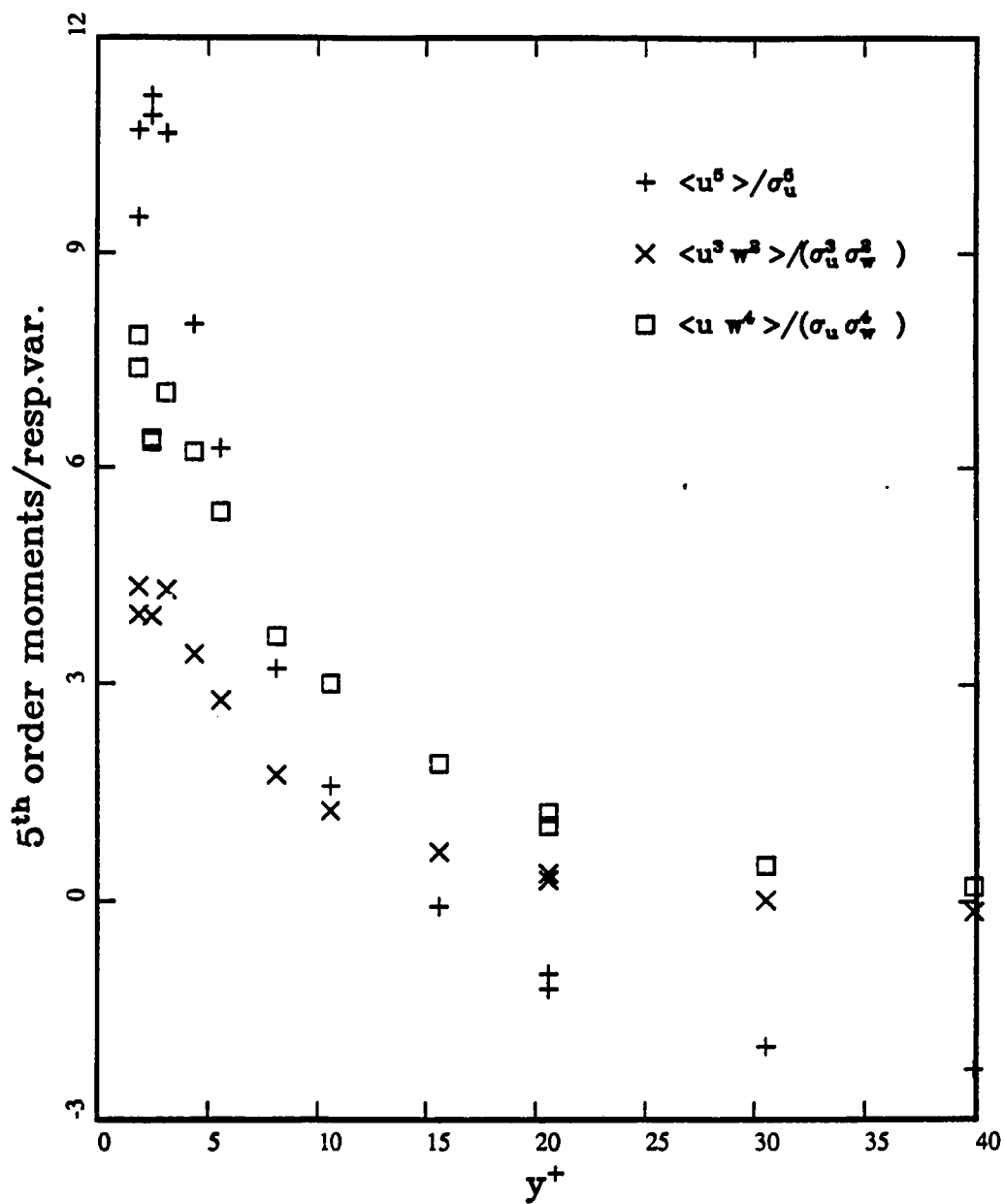
Figure 20: Fifth order central moments of the velocity fluctuations. Symbols represent measured values.
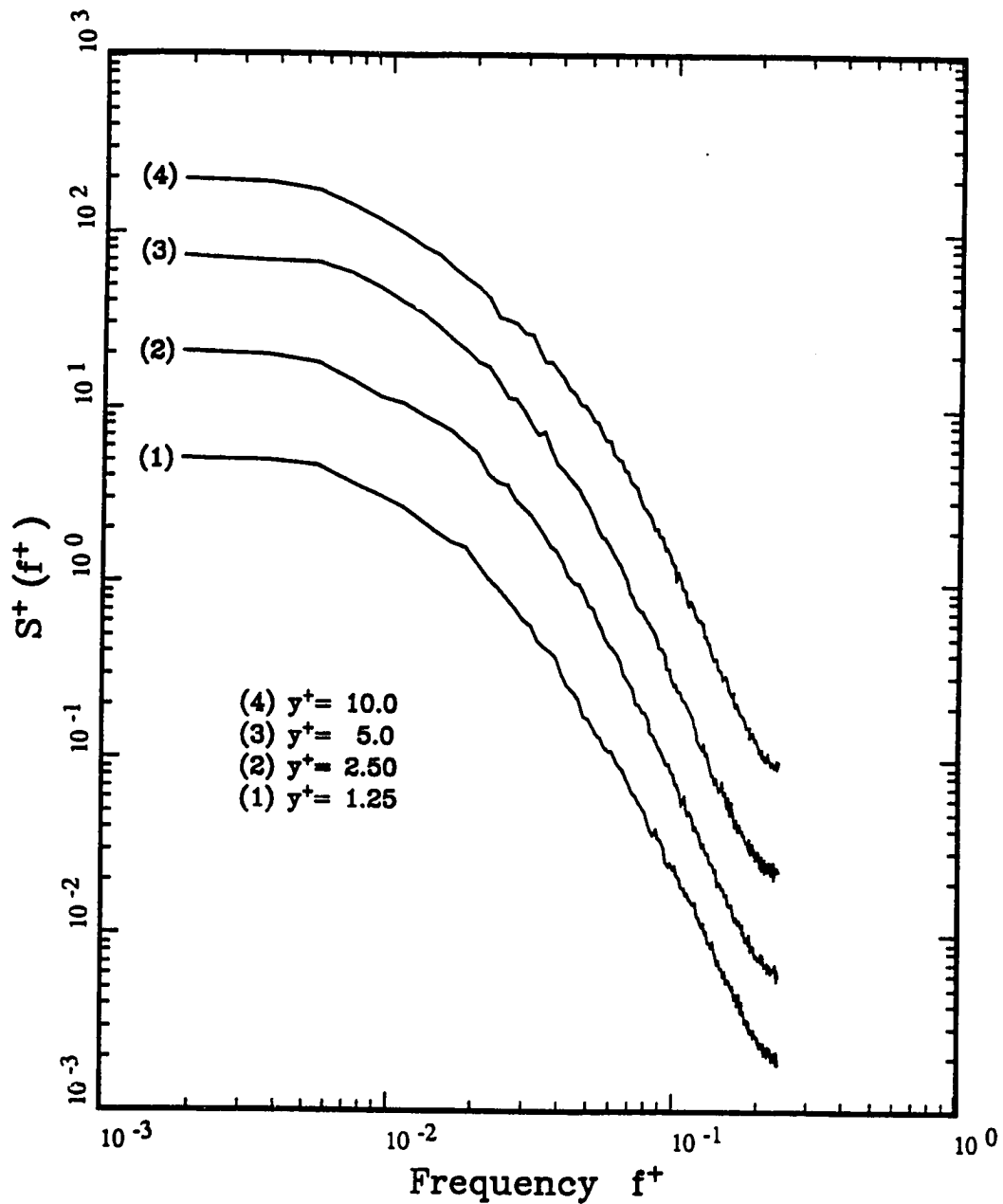
Figure 21: Two-sided power spectra of streamwise velocity component. Frequency and spectra are normalized by inner variables.
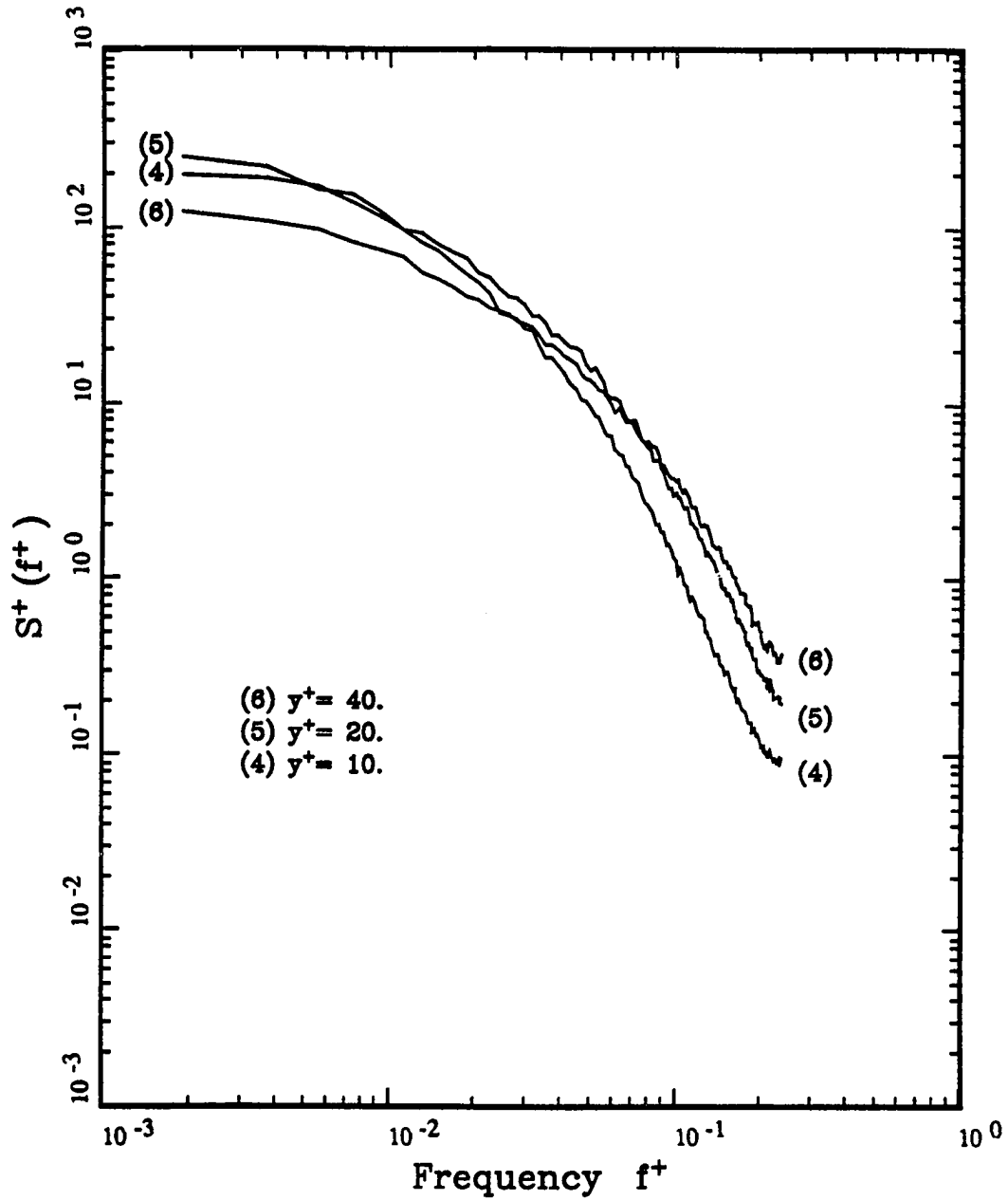
Figure 22: Two-sided power spectra of streamwise
velocity component. Frequency and spectra
are normalized by inner variables.
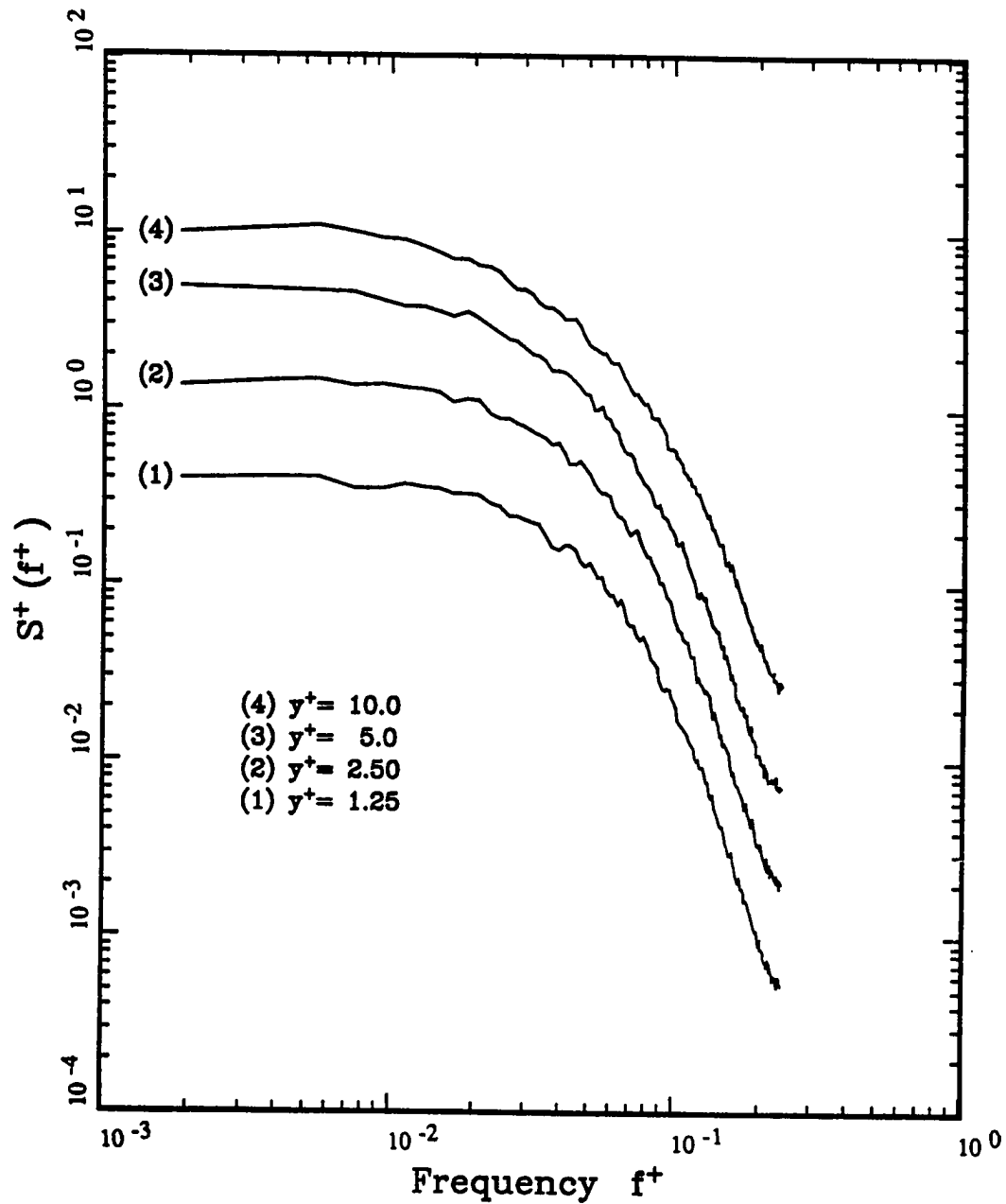
Figure 23: Two-sided power spectra of spanwise velocity component. Frequency and spectra are normalized by inner variables.
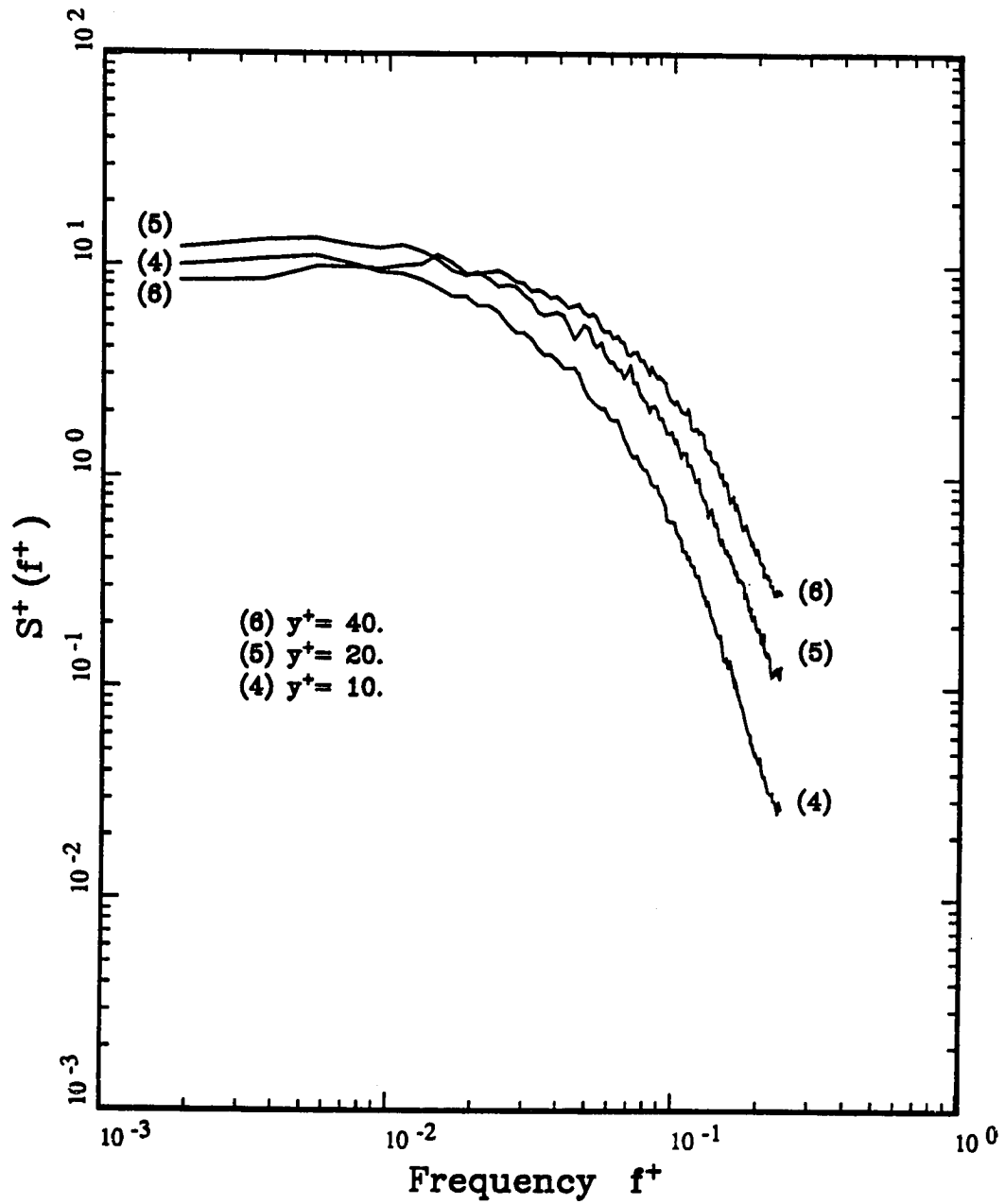
Figure 24: Two—sided power spectra of spanwise velocity component. Frequency and spectra are normalized by inner variables.
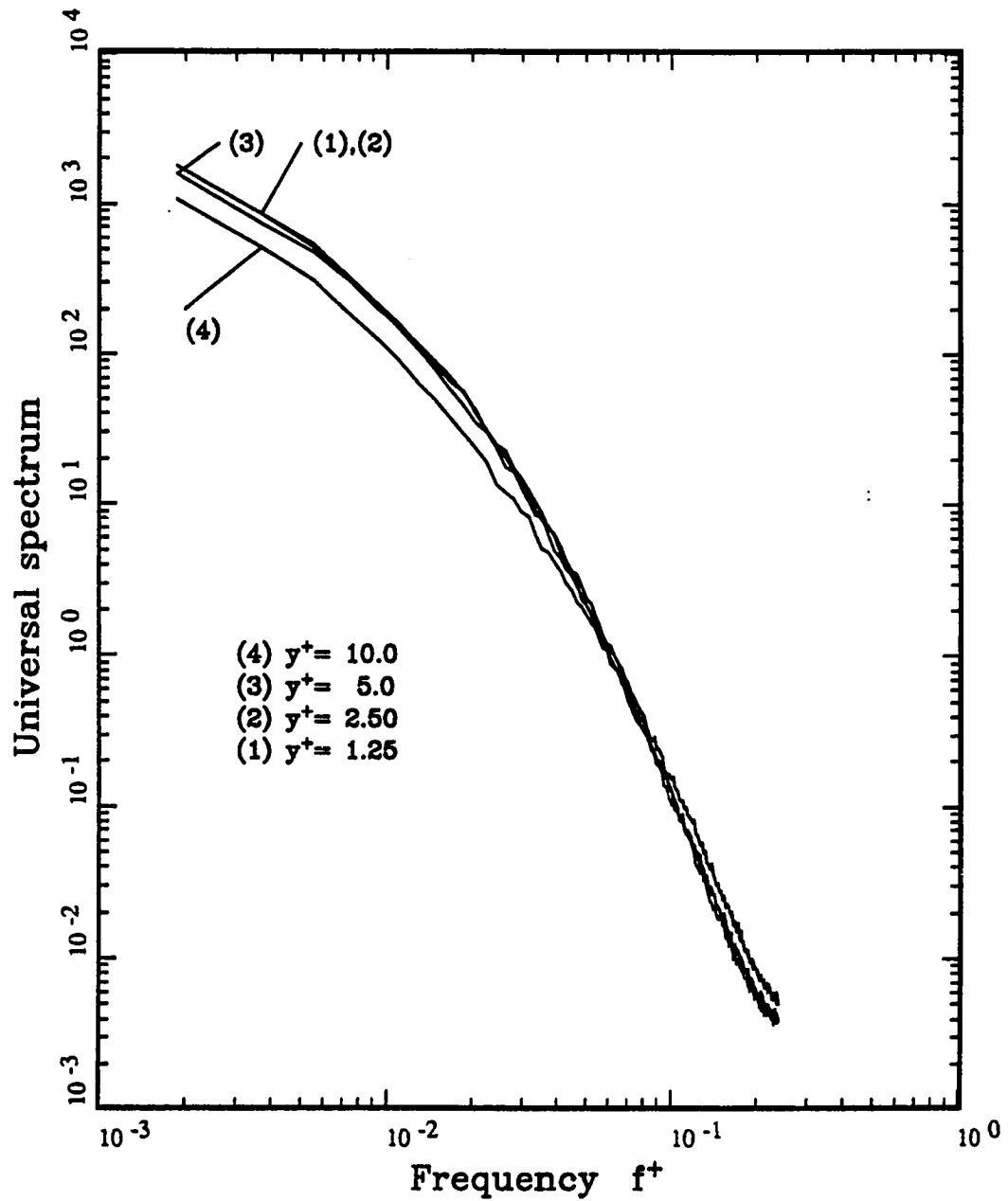
Figure 25: Universal power spectrum of streamwise velocity component in the viscous sublayer.
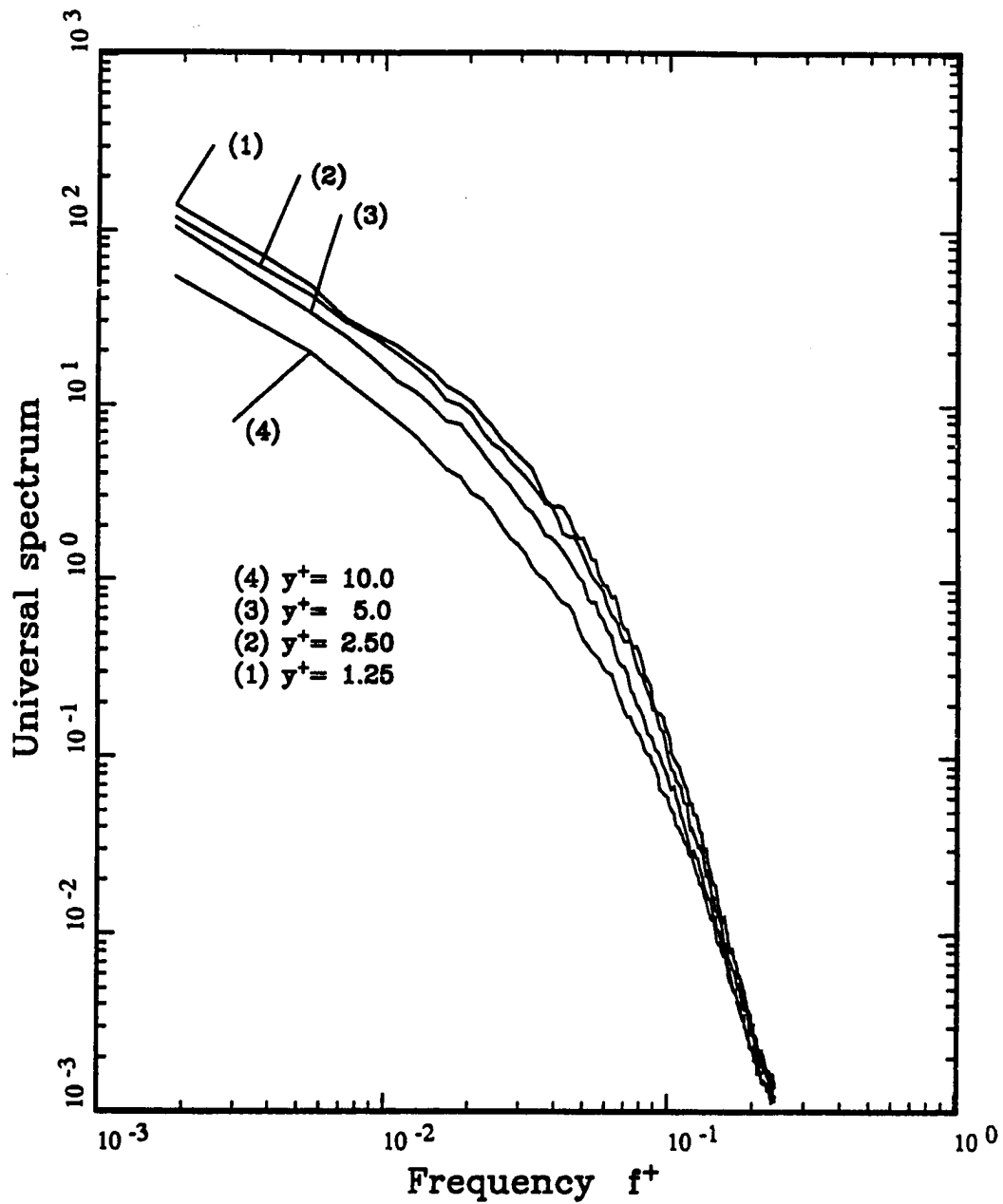
Figure 26: Universal power spectrum of spanwise velocity component in the viscous sublayer.
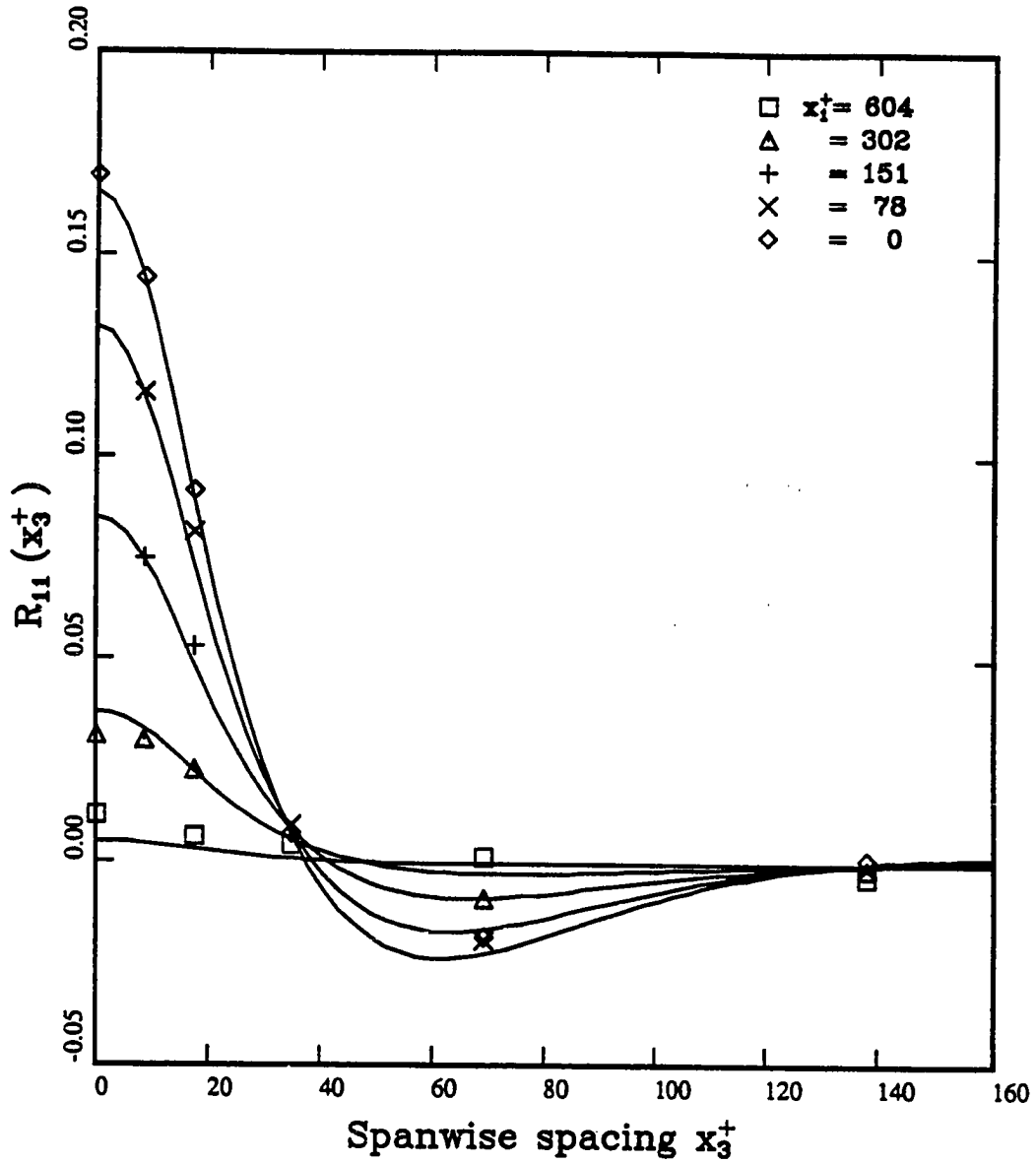
Figure 27: Correlation functions of streamwise velocity components at zero time—lag. Both probes at $y^+= 1.25$.
Comparison of measured data (symbols) with analytical approximation.
Parameter: $x_i^+=$ streamwise spacing.
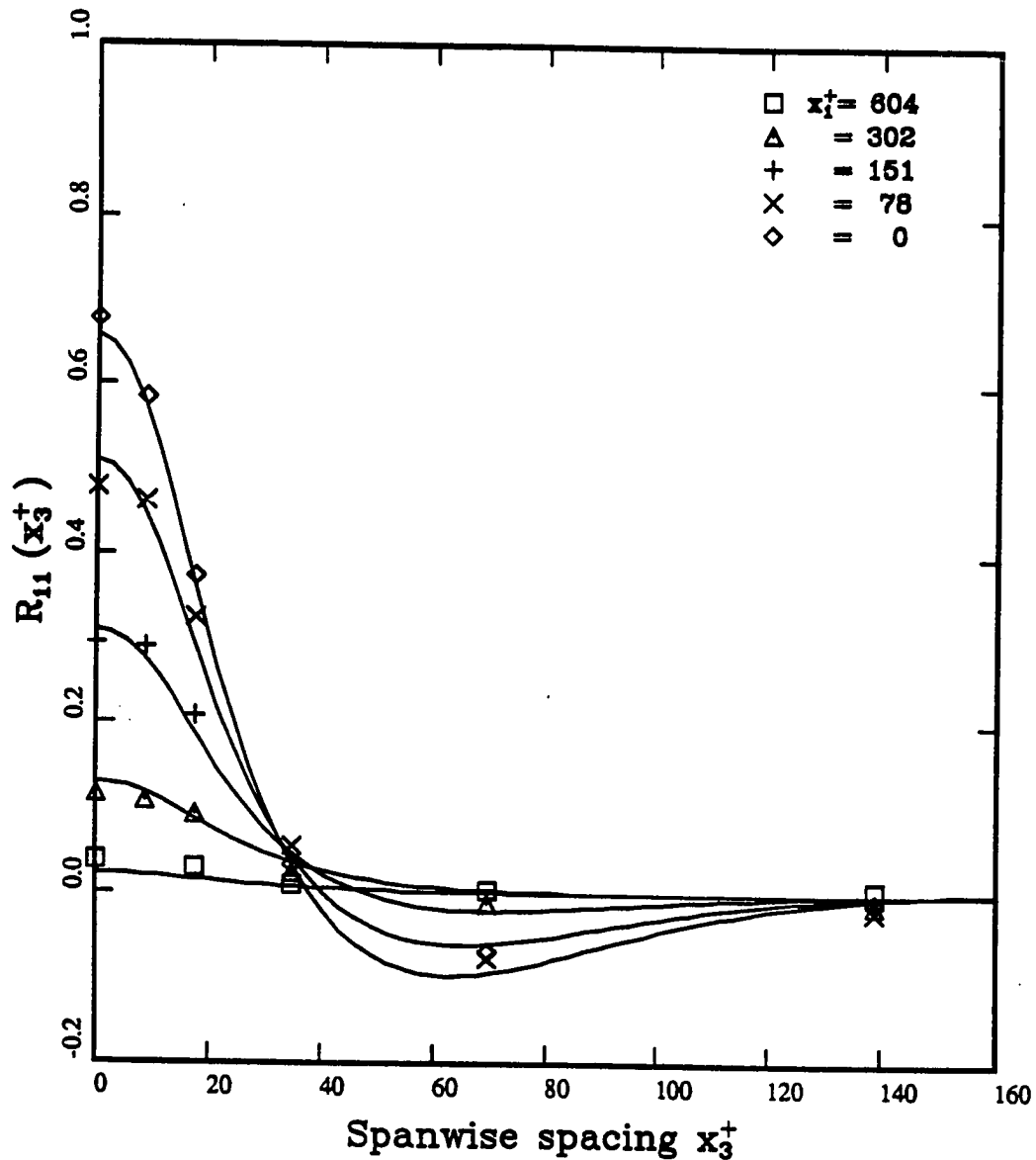
Figure 28: Correlation functions of streamwise velocity
components at zero time—lag. Both probes
at $y^+= 2.50$.
Comparison of measured data (symbols)
with analytical approximation.
Parameter: $x_1^+=$ streamwise spacing.
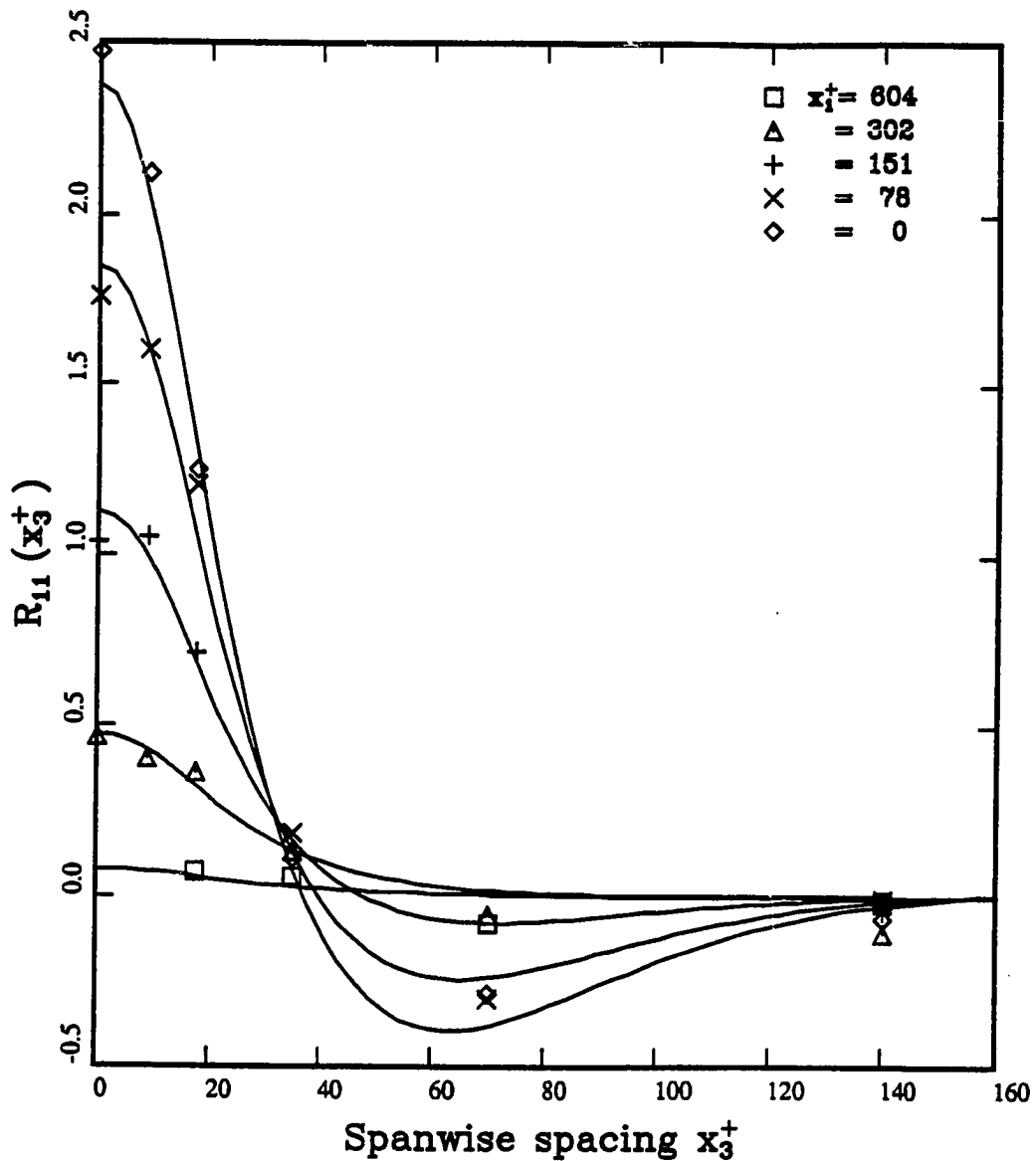
Figure 29: Correlation functions of streamwise velocity components at zero time—lag. Both probes at $y^+= 5.0$.

Comparison of measured data (symbols) with analytical approximation.

Parameter: $x_1^+=$ streamwise spacing.
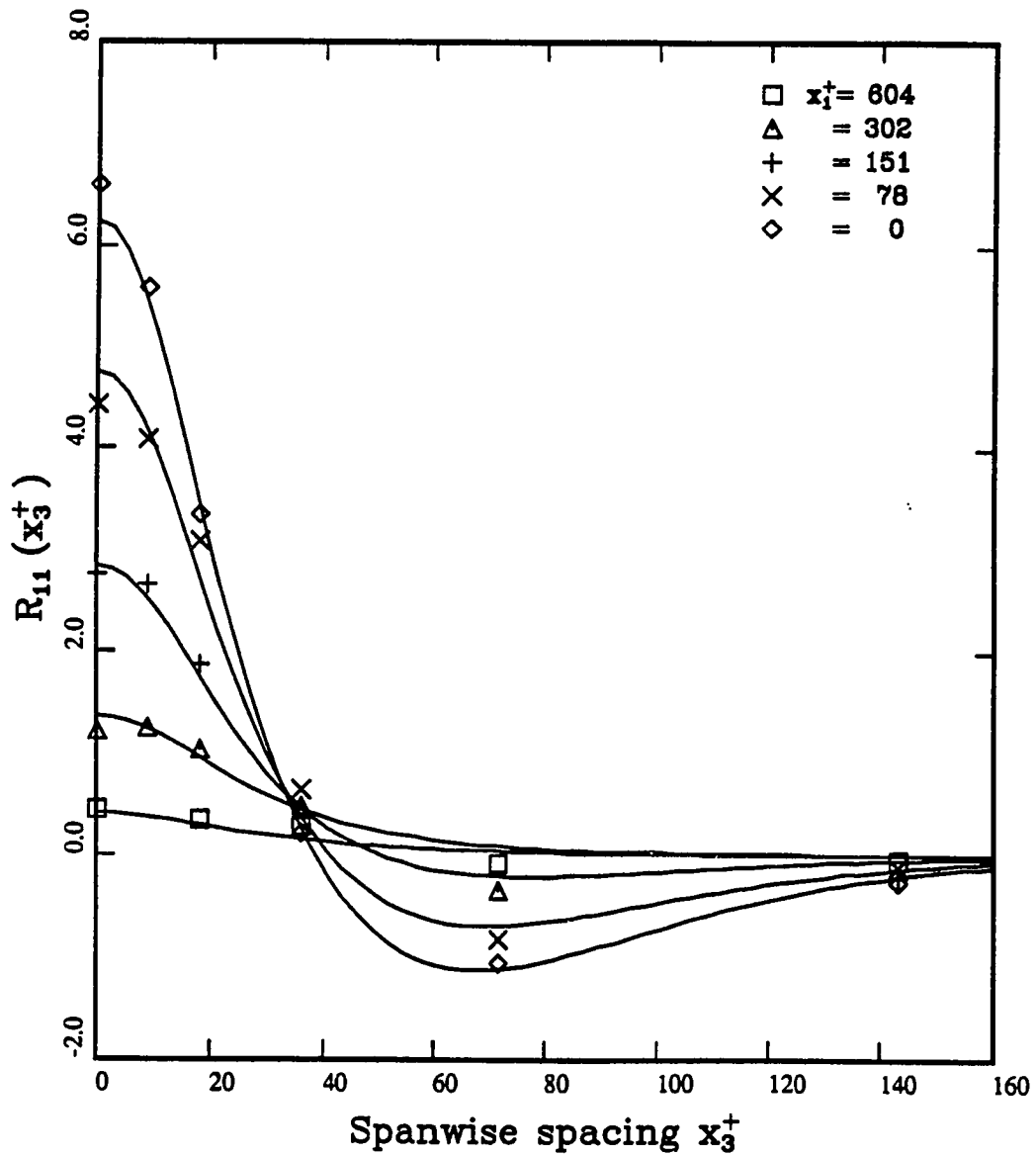
Figure 30: Correlation functions of streamwise velocity
components at zero time−lag. Both probes
at $y^+= 10$.
Comparison of measured data (symbols)
with analytical approximation.
Parameter: $x_1^+=$ streamwise spacing.
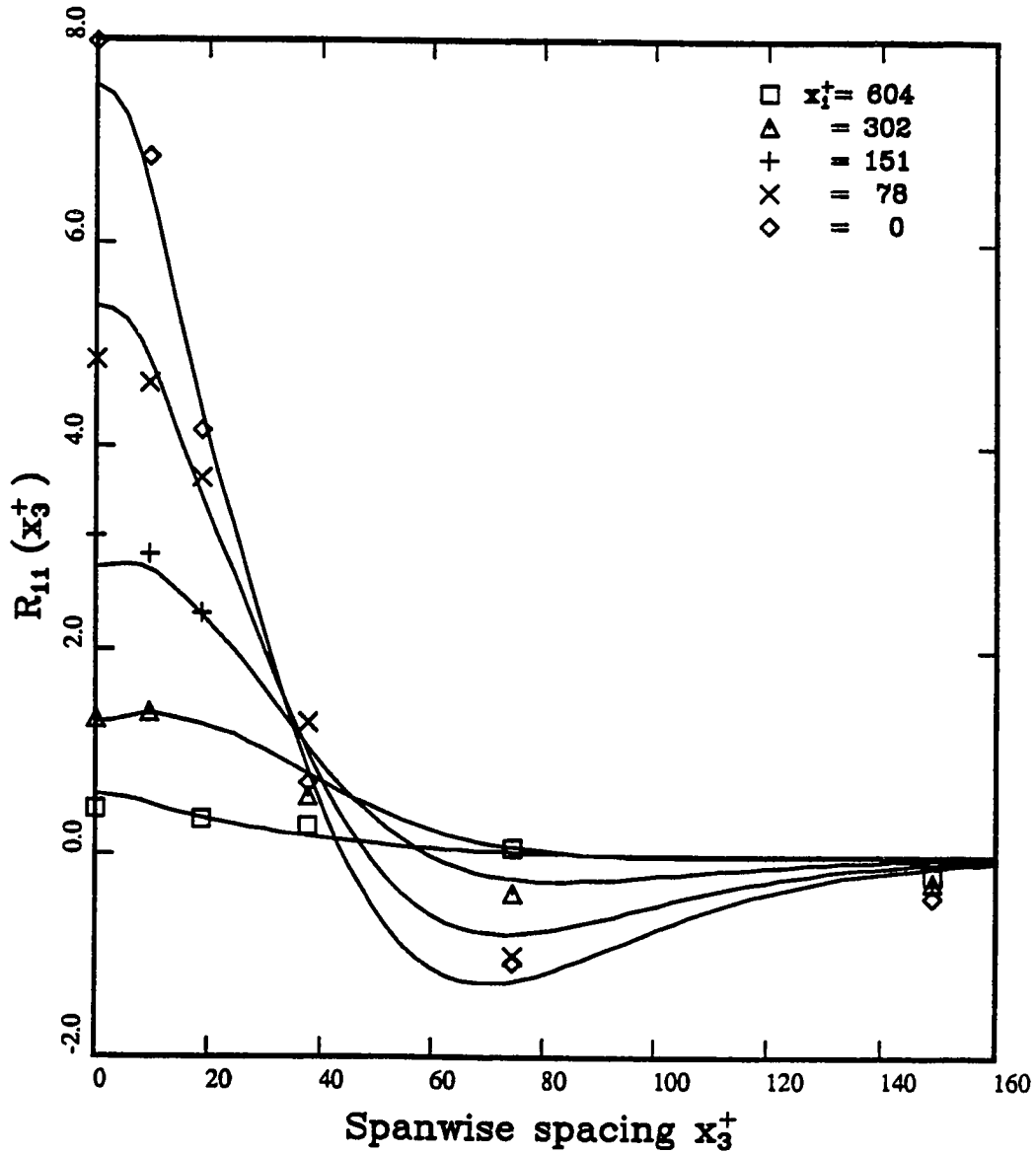
Figure 31: Correlation functions of streamwise velocity
components at zero time-lag. Both probes
at $y^+= 20$.
Comparison of measured data (symbols)
with analytical approximation.
Parameter: $x_i^+=$ streamwise spacing.
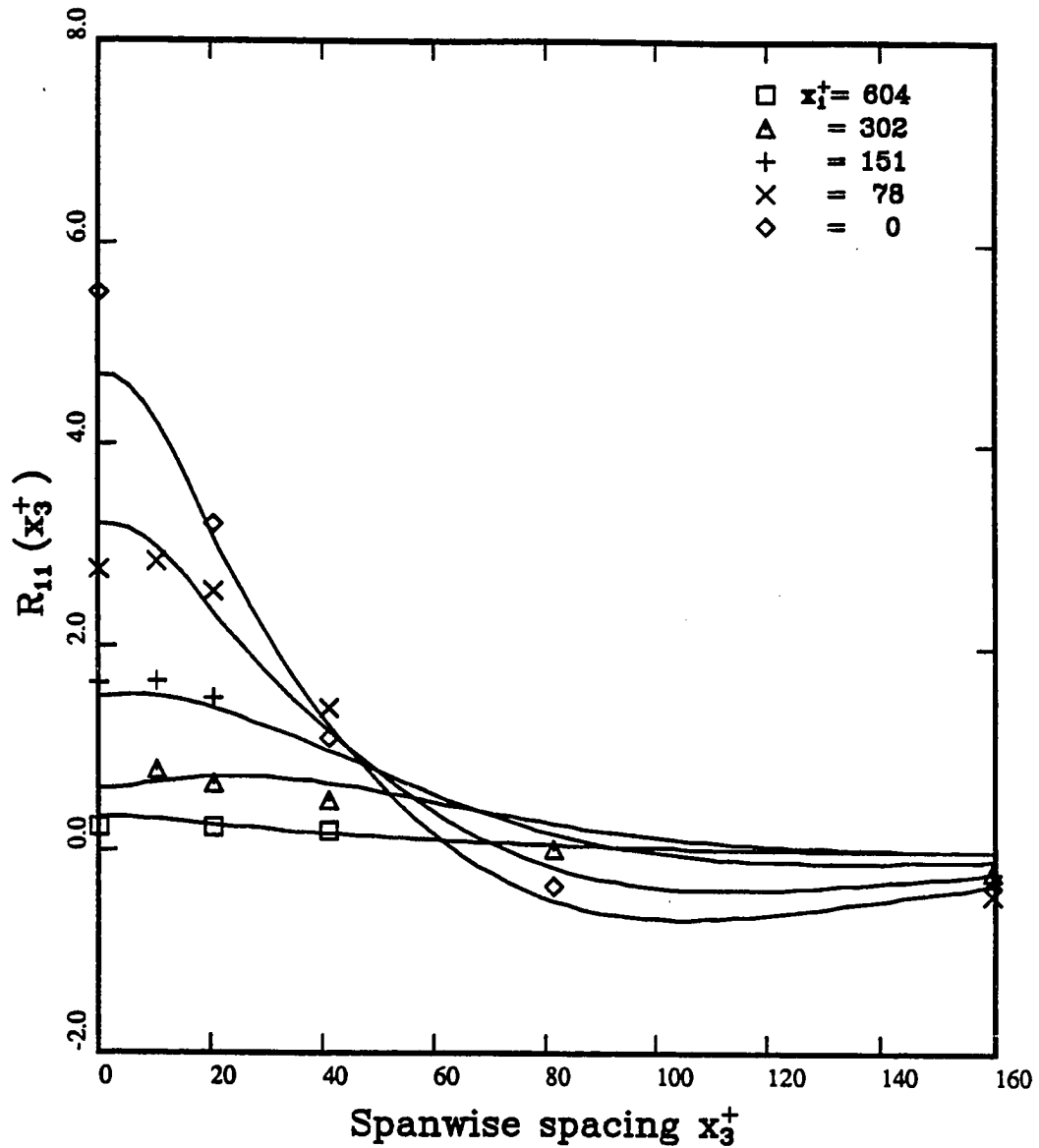
Figure 32: Correlation functions of streamwise velocity components at zero time−lag. Both probes at $y^+ = 40$.
Comparison of measured data (symbols) with analytical approximation.
Parameter: $x_i^+ =$ streamwise spacing.
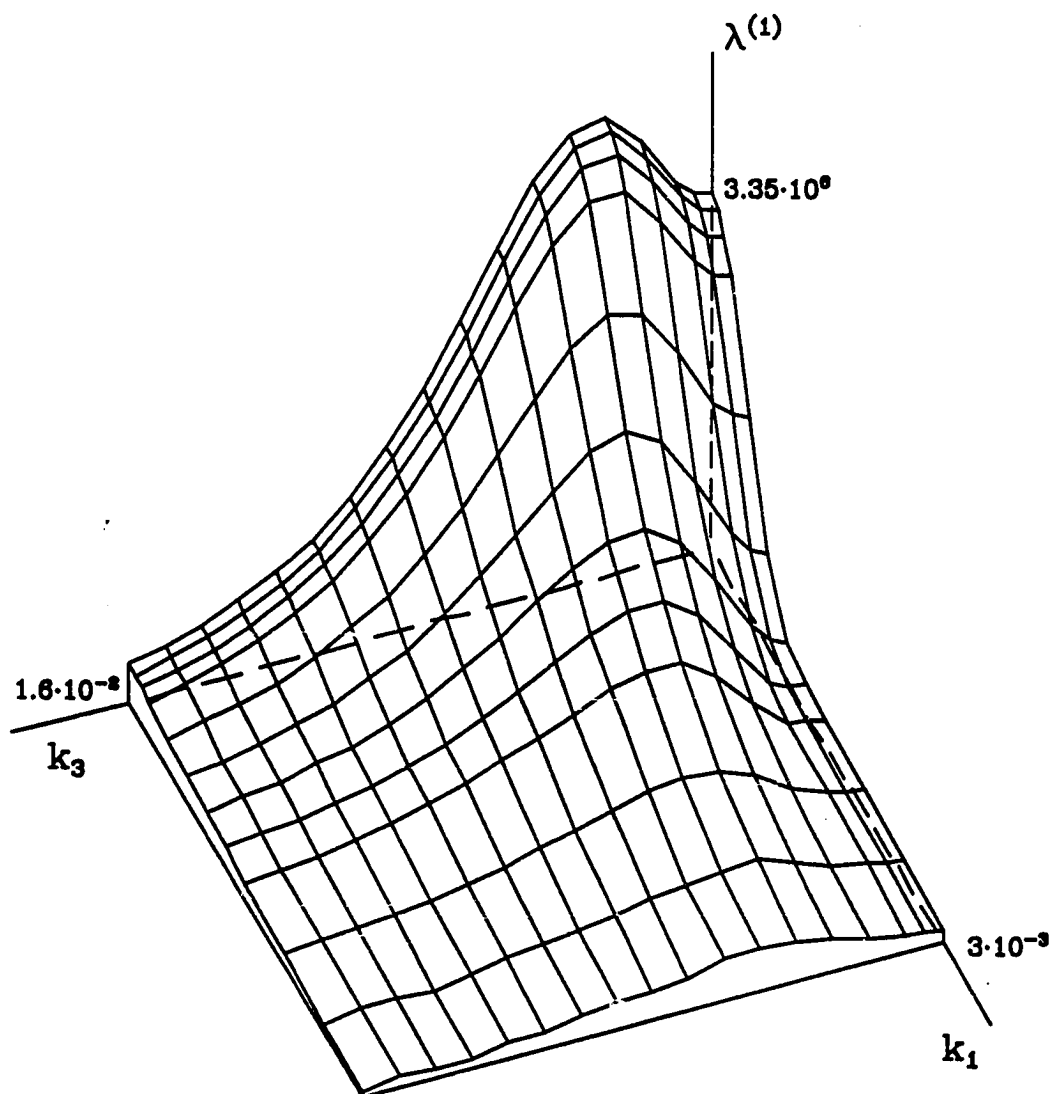
Figure 33: Dominant eigenvalue as function
of the streamwise wave−number k_1
and spanwise wave−number k_3.
$\lambda^{(1)}$ is even in k_1 and k_3.
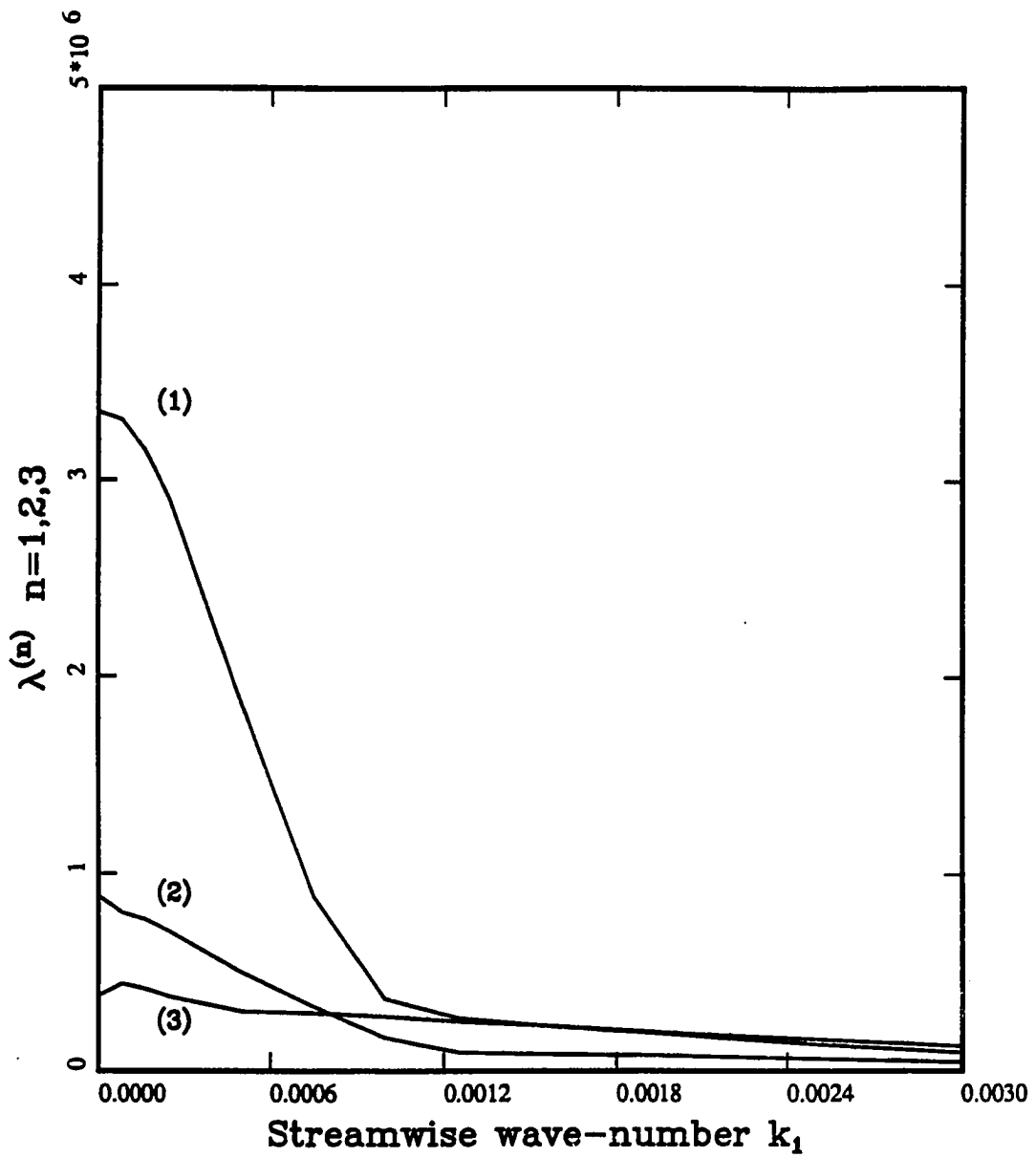
Figure 34: First three eigenvalues as function of
streamwise wave-number. All variables
are normalized by inner variables.
Spanwise wave-number: $k_3=0$.
Note the cross-over between 2. and 3.
eigenvalue.
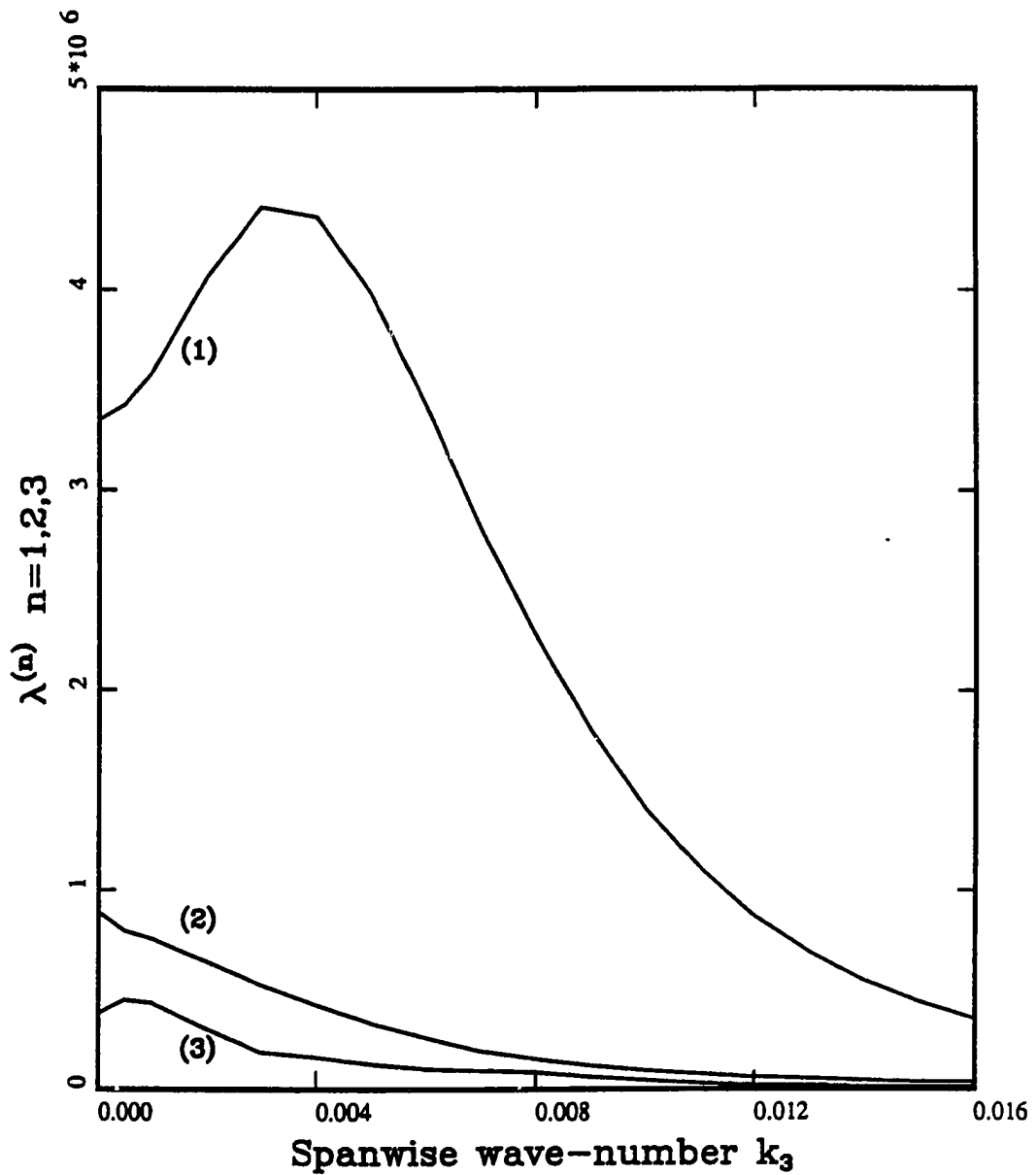
Figure 35: First three eigenvalues as function of spanwise wave-number. All variables are normalized by inner variables. Streamwise wave-number: $k_1 = 0$.
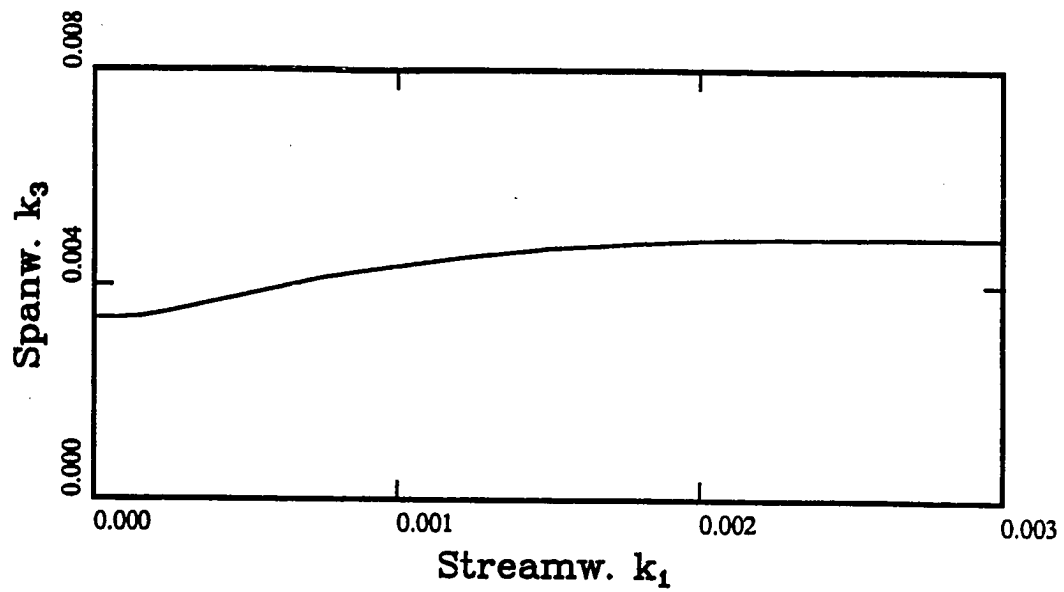
Figure 36: Trace of $k_3 = func(k_1)$ for which $\lambda^{(1)}$ is maximal.
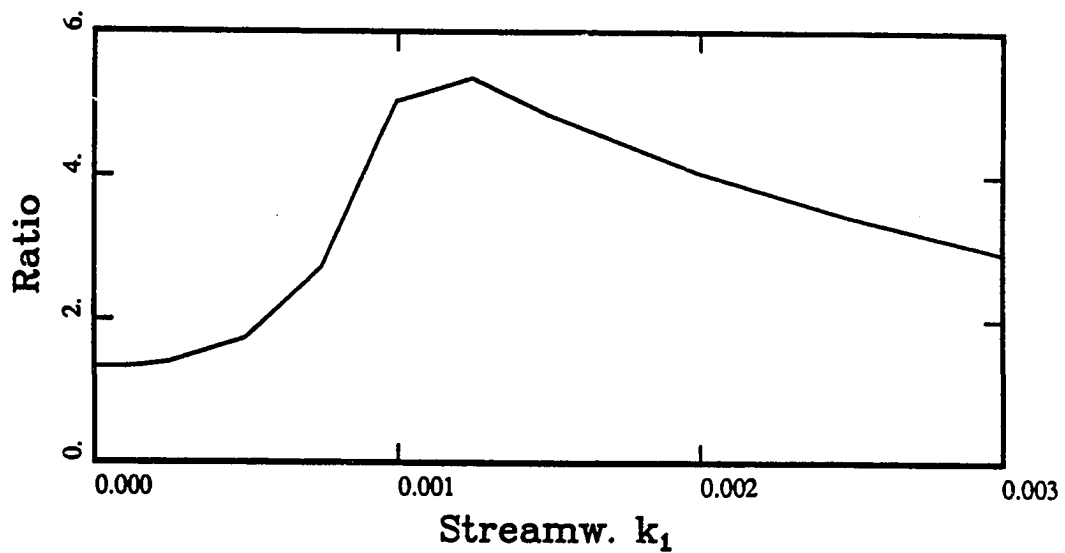
Figure 37: Ratio of maximum $\lambda^{(1)}$ to its value at $k_3 = 0$.
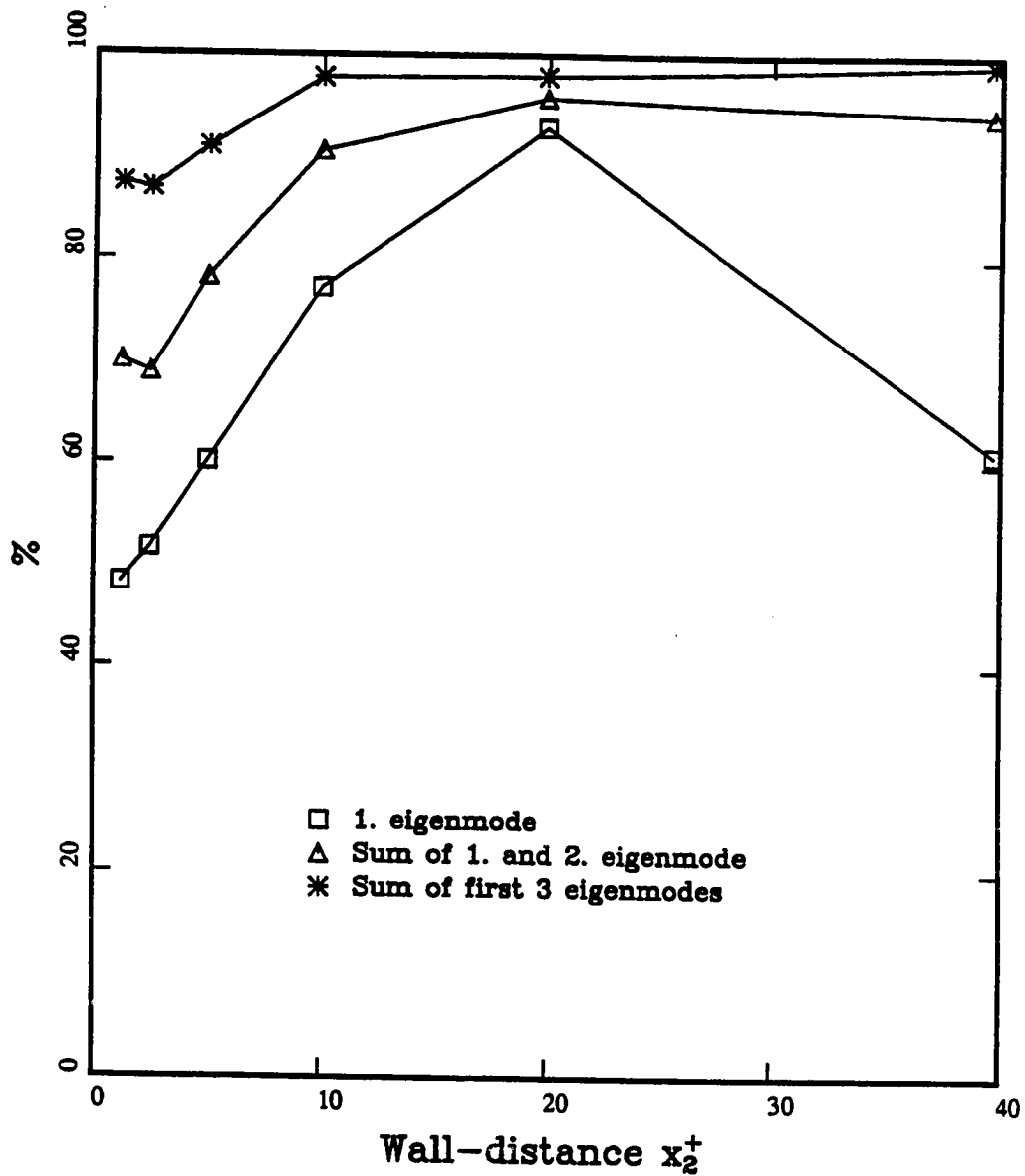
Figure 38: Contributions of first three eigenmodes to variance of streamwise velocity fluctuations. 100% equals contributions of all eigenfunctions from all wave-numbers investigated.
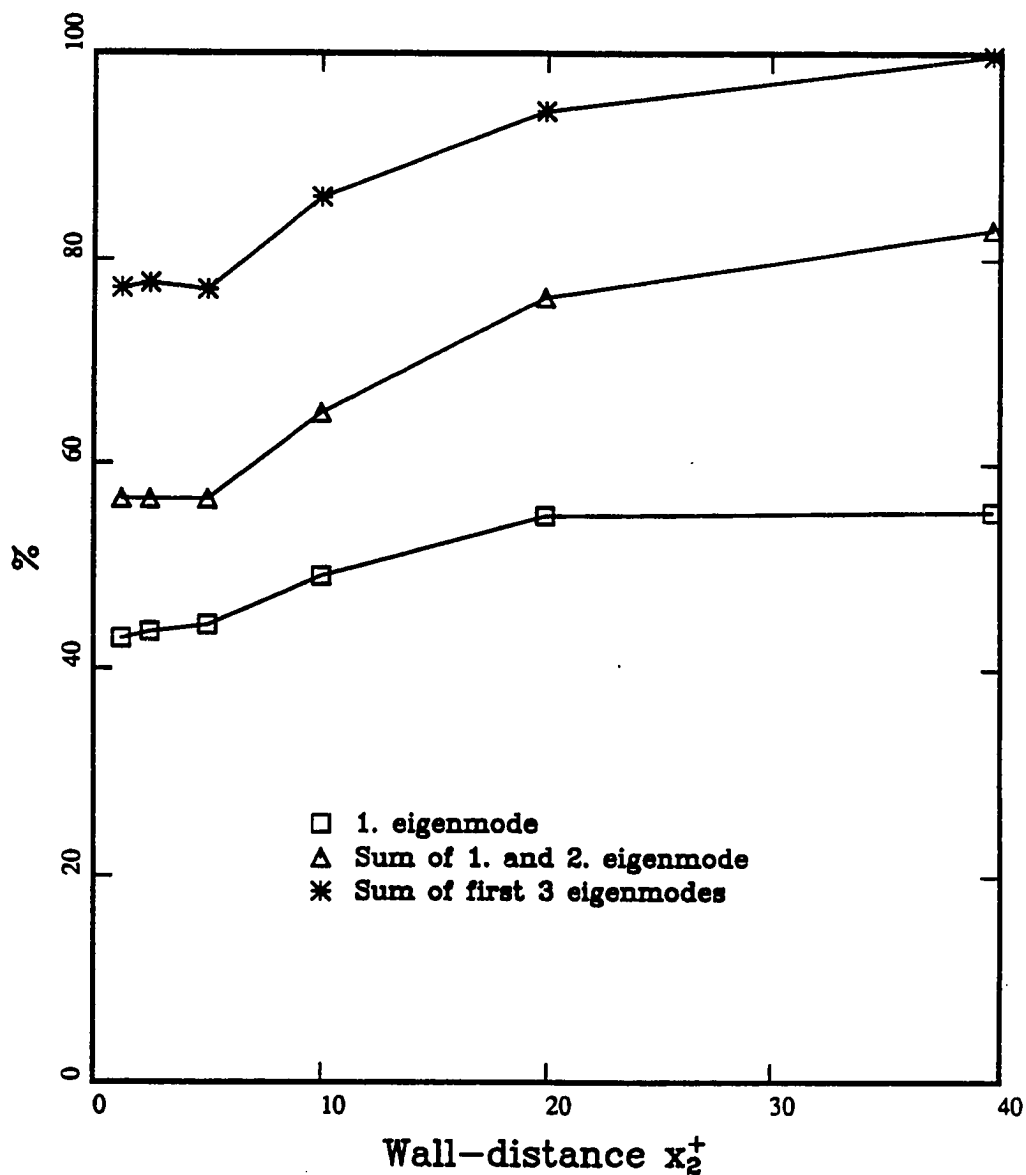
Figure 39: Contributions of first three eigenmodes to variance of wall−normal velocity fluctuations. 100% equals contributions of all eigenfunctions from all wave−numbers investigated.
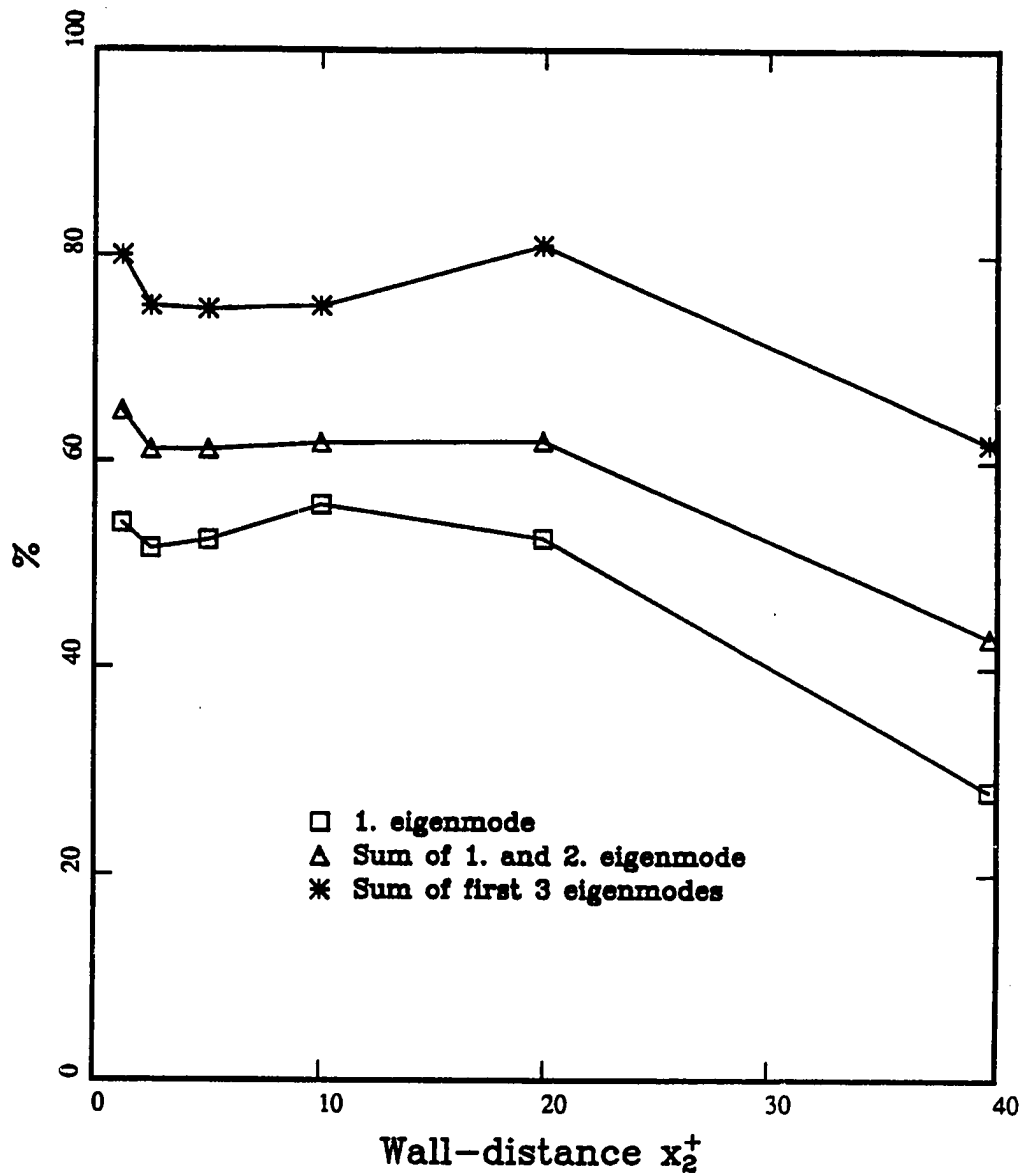
Figure 40: Contributions of first three eigenmodes to variance of spanwise velocity fluctuations. 100% equals contributions of all eigenfunctions from all wave-numbers investigated.
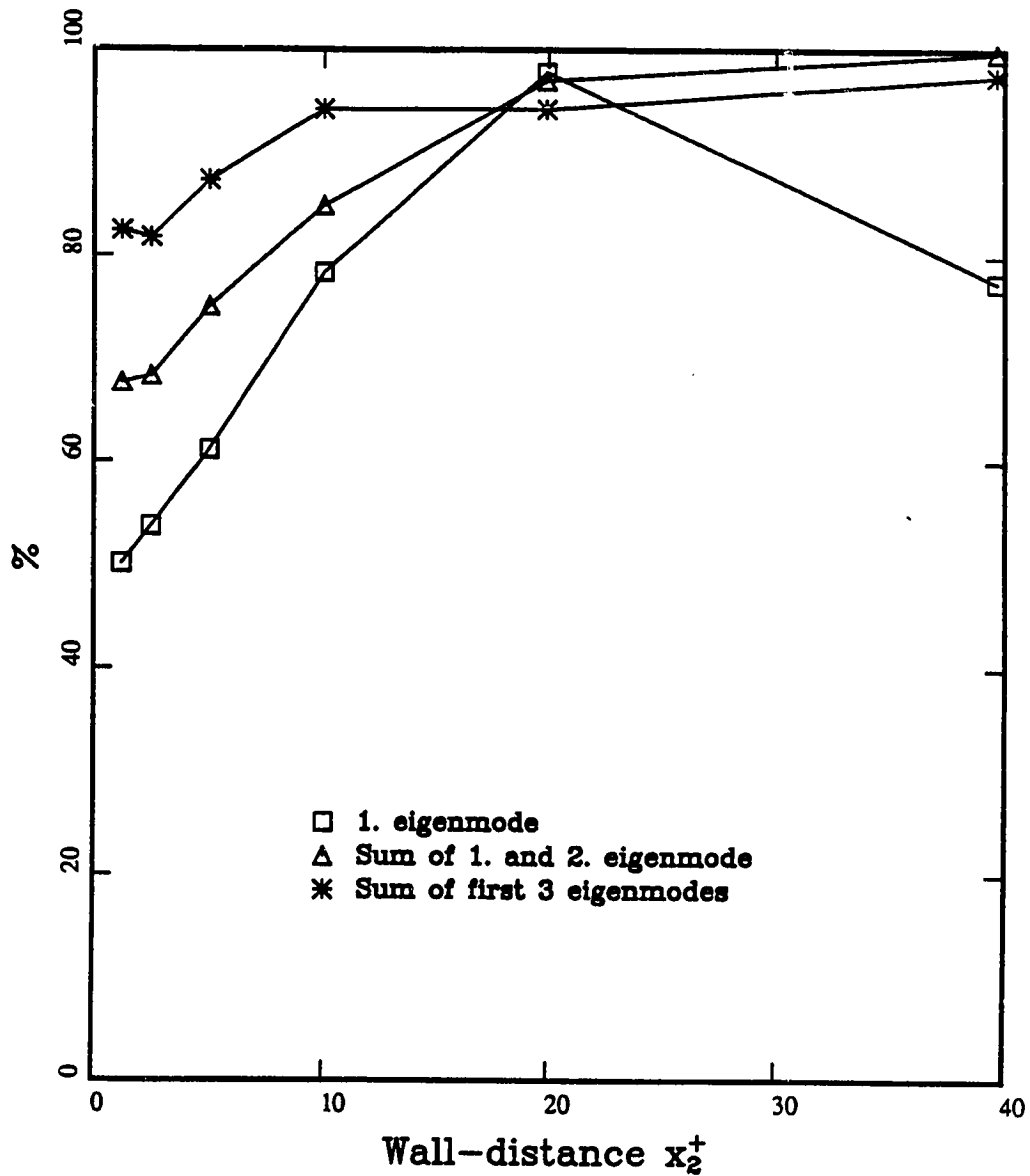
Figure 41: Contributions of first three eigenmodes
to Reynolds shear stress. 100% equals
contributions of all eigenfunctions from all
wave–numbers investigated.
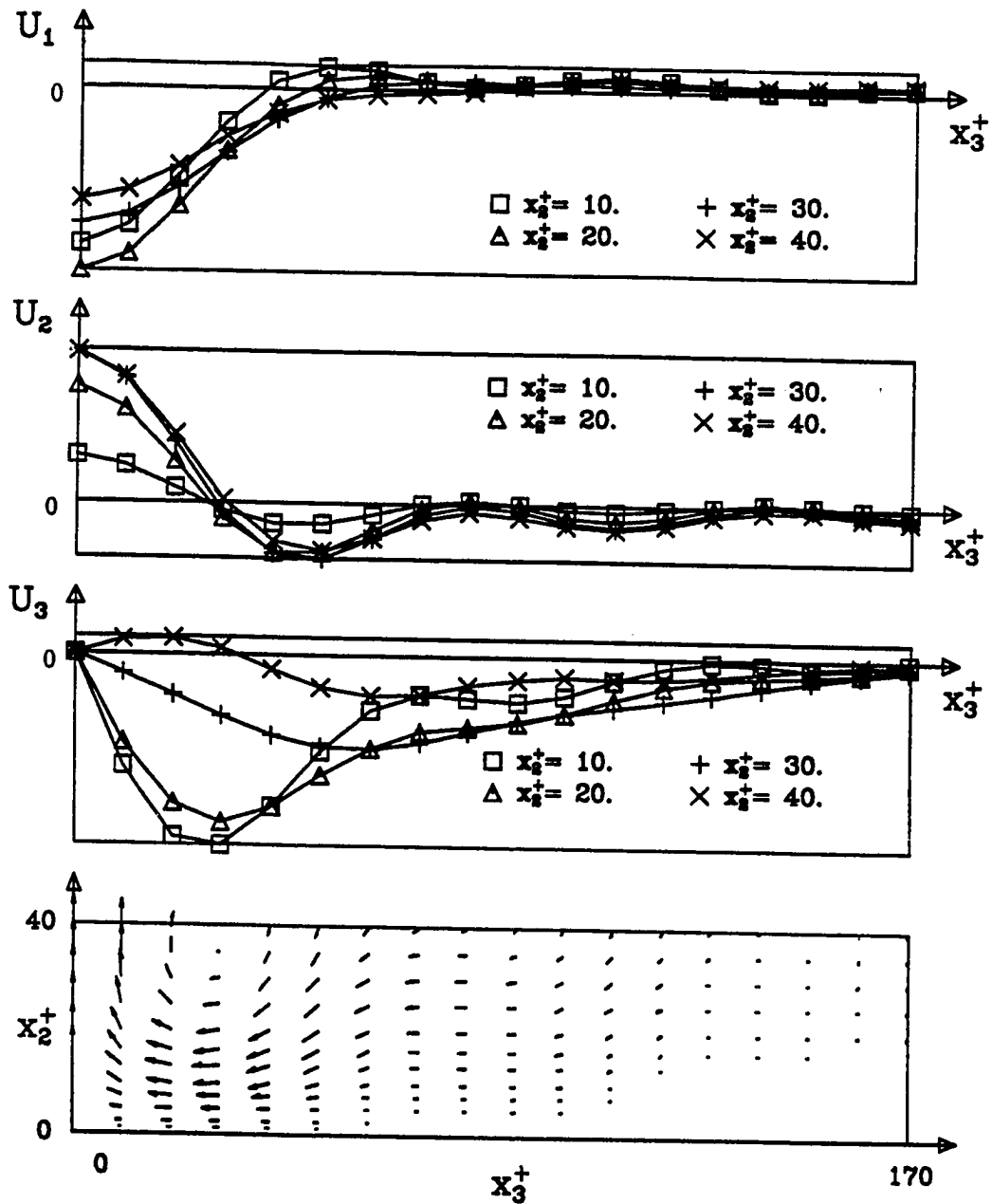
Figure 42: Velocity components of integrated typical eddy and vectorial plot of the flow field. x_2^+=streamwise,x_3^+=spanwise coord.
Streamwise velocity: U_1 -17.42 .. 2.24
Wall−normal velocity: U_2 -0.83 .. 2.15
Spanwise velocity: U_3 -1.69 .. 0.14
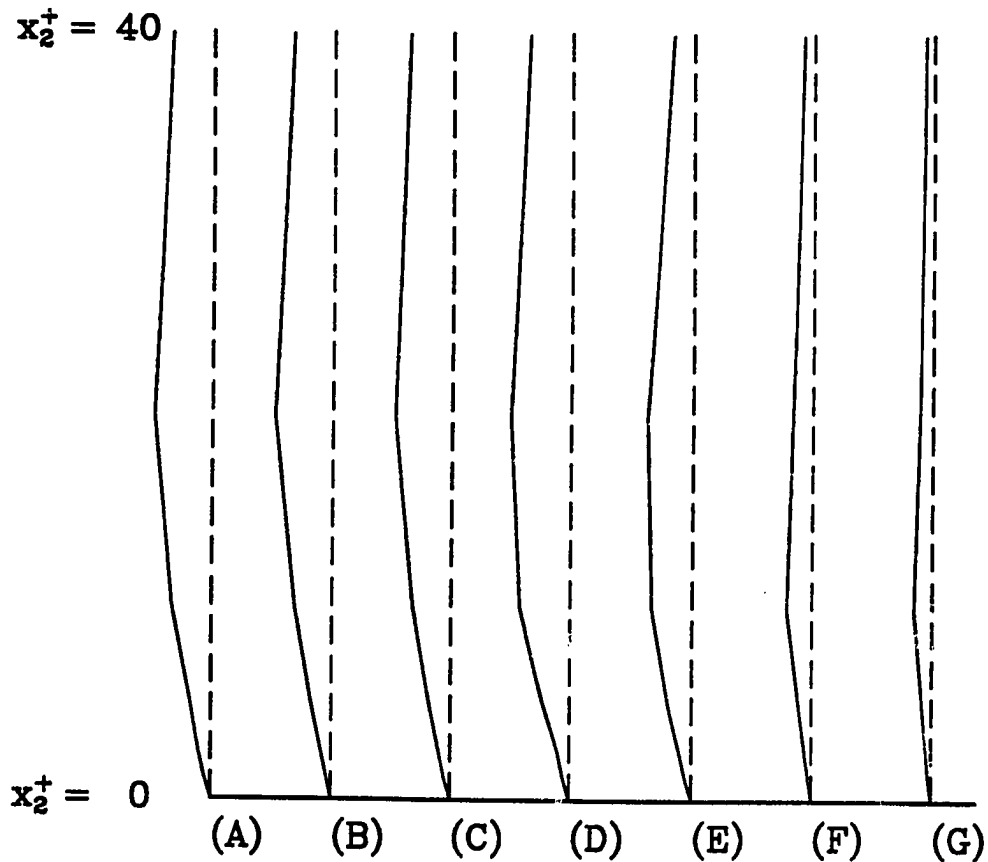
Figure 43: Streamwise component of eigenfunction weighted by square root of eigenvalue as function of the wall distance x_2^+.
At $x_2^+ = 0$ each eigenfunction is zero.
Streamwise wave-number $k_1 = 0$.
Parameter is the spanwise wave-number k_3:

(A) 0.   (B) 5.0E-4   (C) 1.0E-3
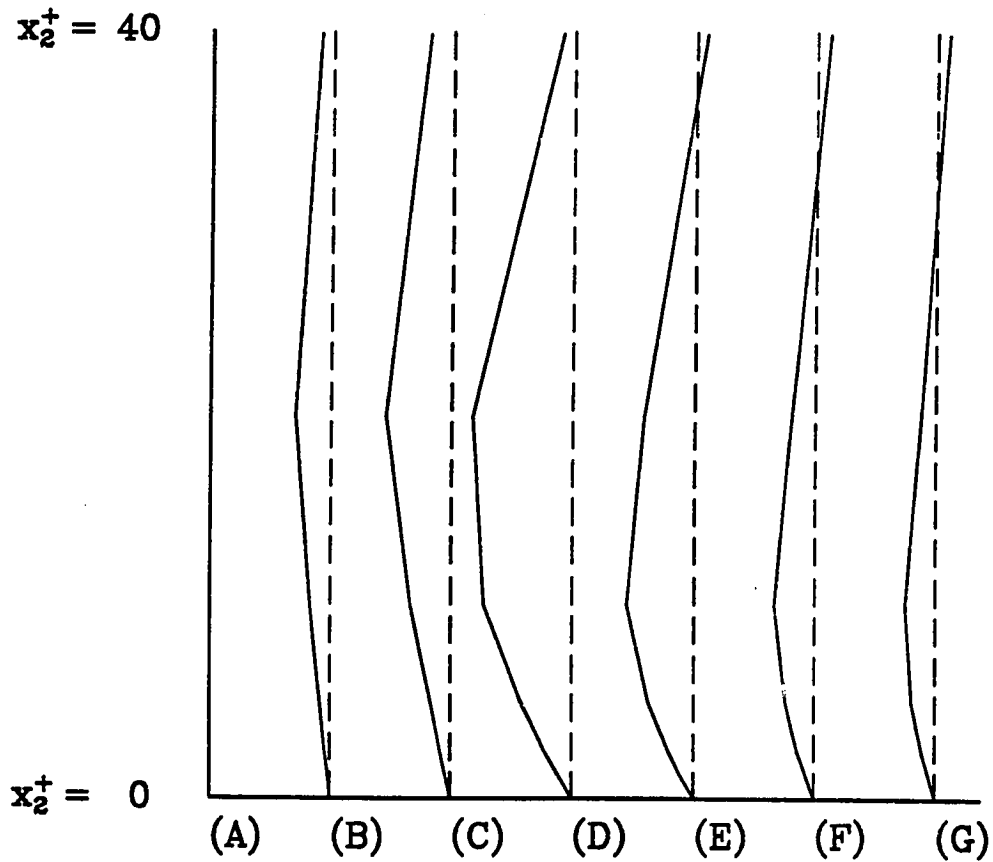
(D) 4.0E-3   (E) 8.0E-3   (F) 1.3E-2

(G) 1.6E-2

$x_2^+ = 40$

$x_2^+ = 0$

(A) (B) (C) (D) (E) (F) (G)
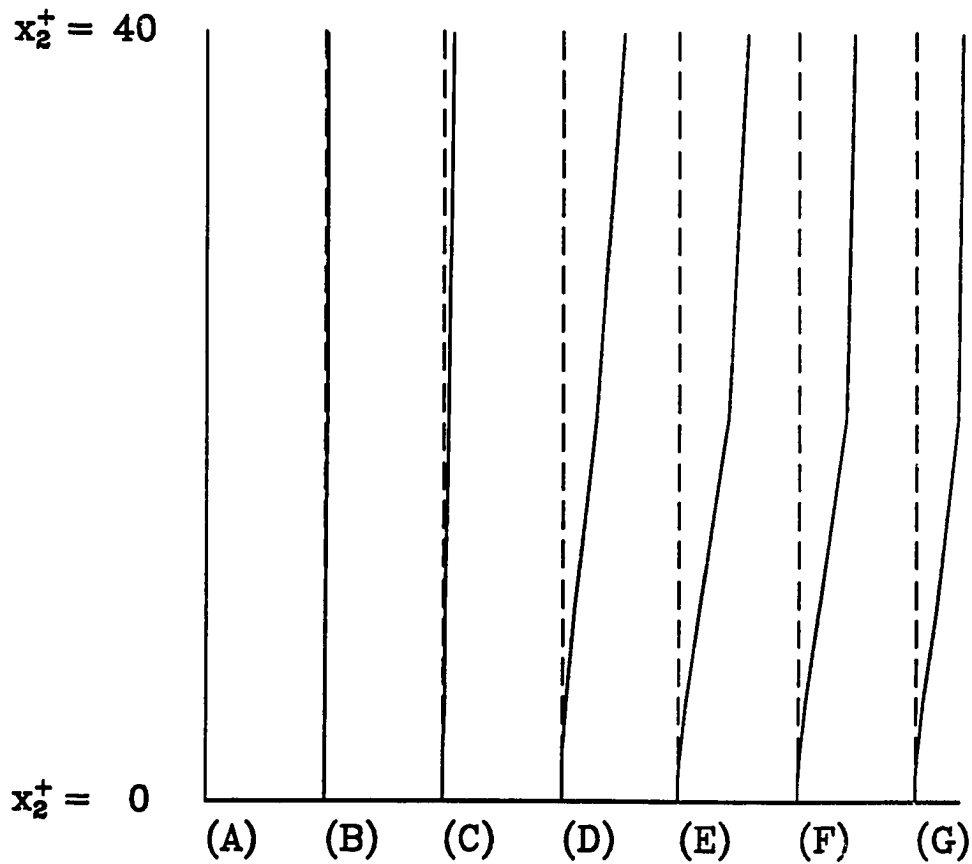
Figure 44: Wall—normal component of eigenfunction weighted by square root of eigenvalue as function of the wall distance x_2^+.
At $x_2^+ = 0$ each eigenfunction is zero.
Streamwise wave—number $k_1 = 0$.
Parameter is the spanwise wave—number k_3:

(A) 0. (B) 5.0E—4 (C) 1.0E—3

(D) 4.0E—3 (E) 8.0E—3 (F) 1.3E—2

(G) 1.6E—2

$x_2^+ = 40$

$x_2^+ = 0$

(A) (B) (C) (D) (E) (F) (G)

Figure 45: Spanwise component of eigenfunction
weighted by square root of eigenvalue as
function of the wall distance x_2^+ .
At $x_2^+ = 0$ each eigenfunction is zero.
Streamwise wave-number $k_1 = 0$.
Parameter is the spanwise wave-number k_3:

(A) 0.   (B) 5.0E-4   (C) 1.0E-3

(D) 4.0E-3   (E) 8.0E-3   (F) 1.3E-2

(G) 1.6E-2
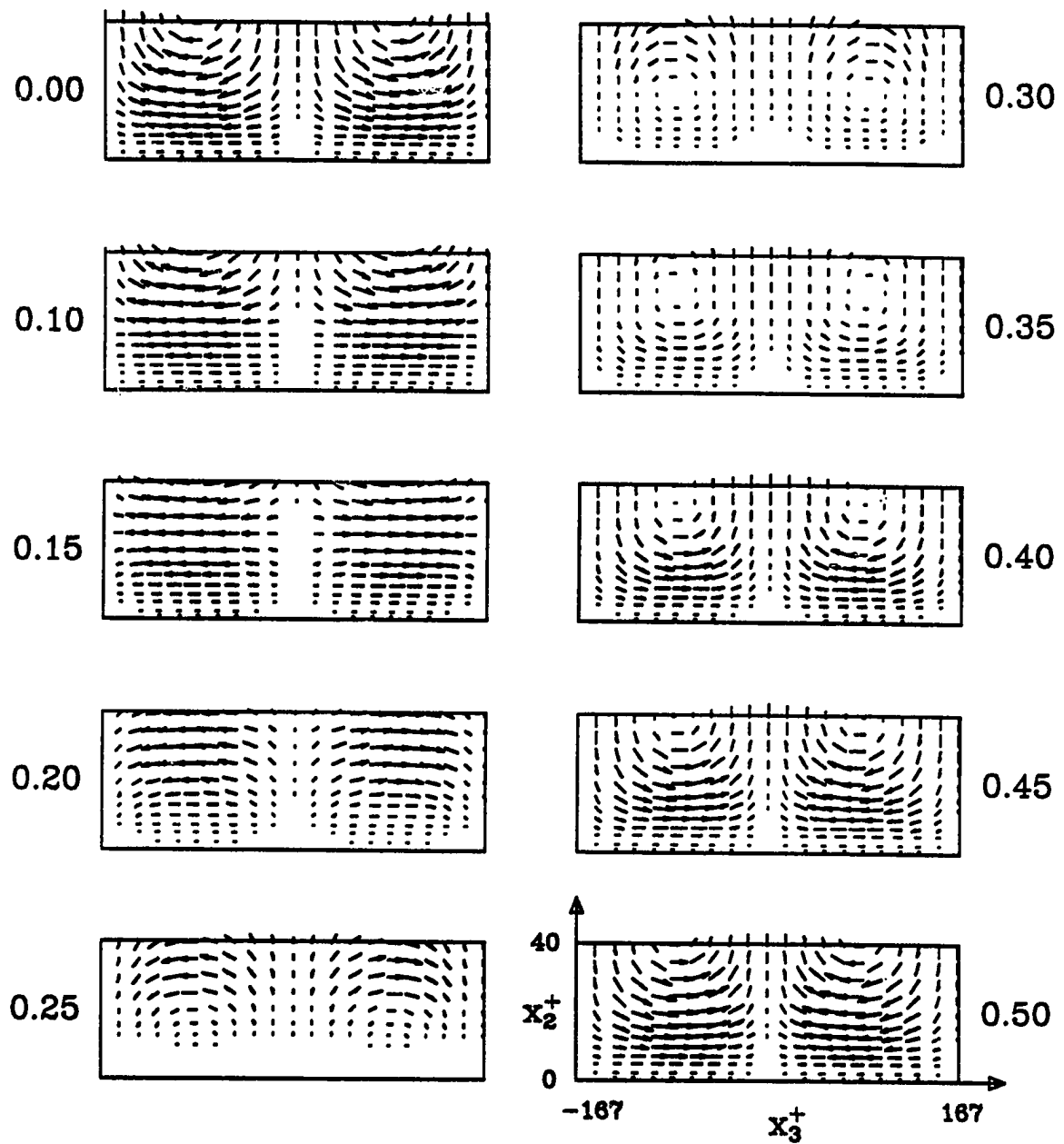
Figure 46: Example for universal Fouriermode with
$k_1=7.5E-4$, $k_3=3.E-3$.
Cross−sectional cuts at k_1x_1 as indicated
for each graph. Wall−normal and spanwise
extent are given in bottom right graph only.
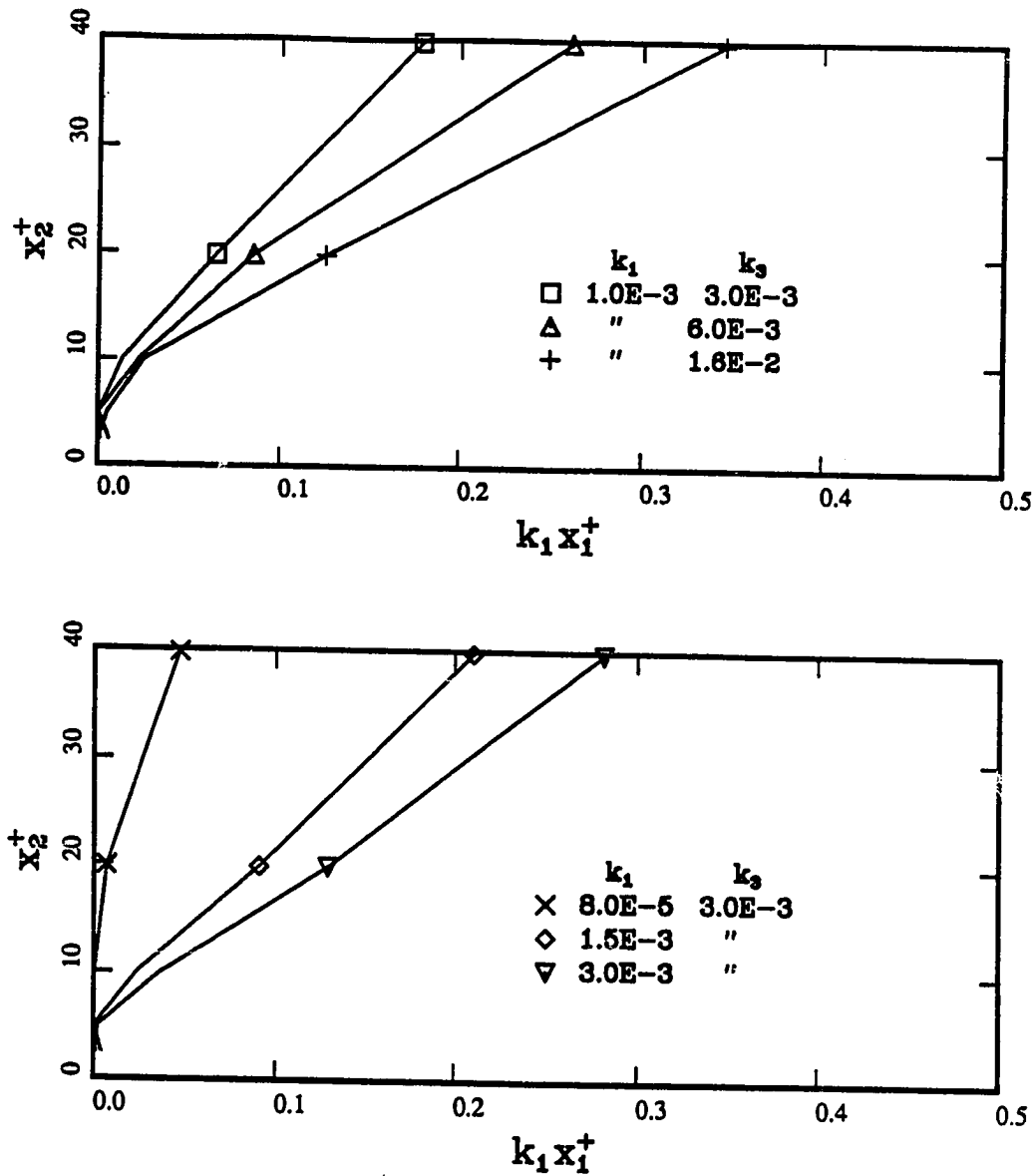
Figure 47: Location of zero spanwise velocity in the planes $k_3x_3^+=\pm1/4$.

The centerlines start perpendicular to the wall. The centerlines of the next downstream pair of rolls (opposite sense of rotation) rise at $k_1x_1^+=0.5$.
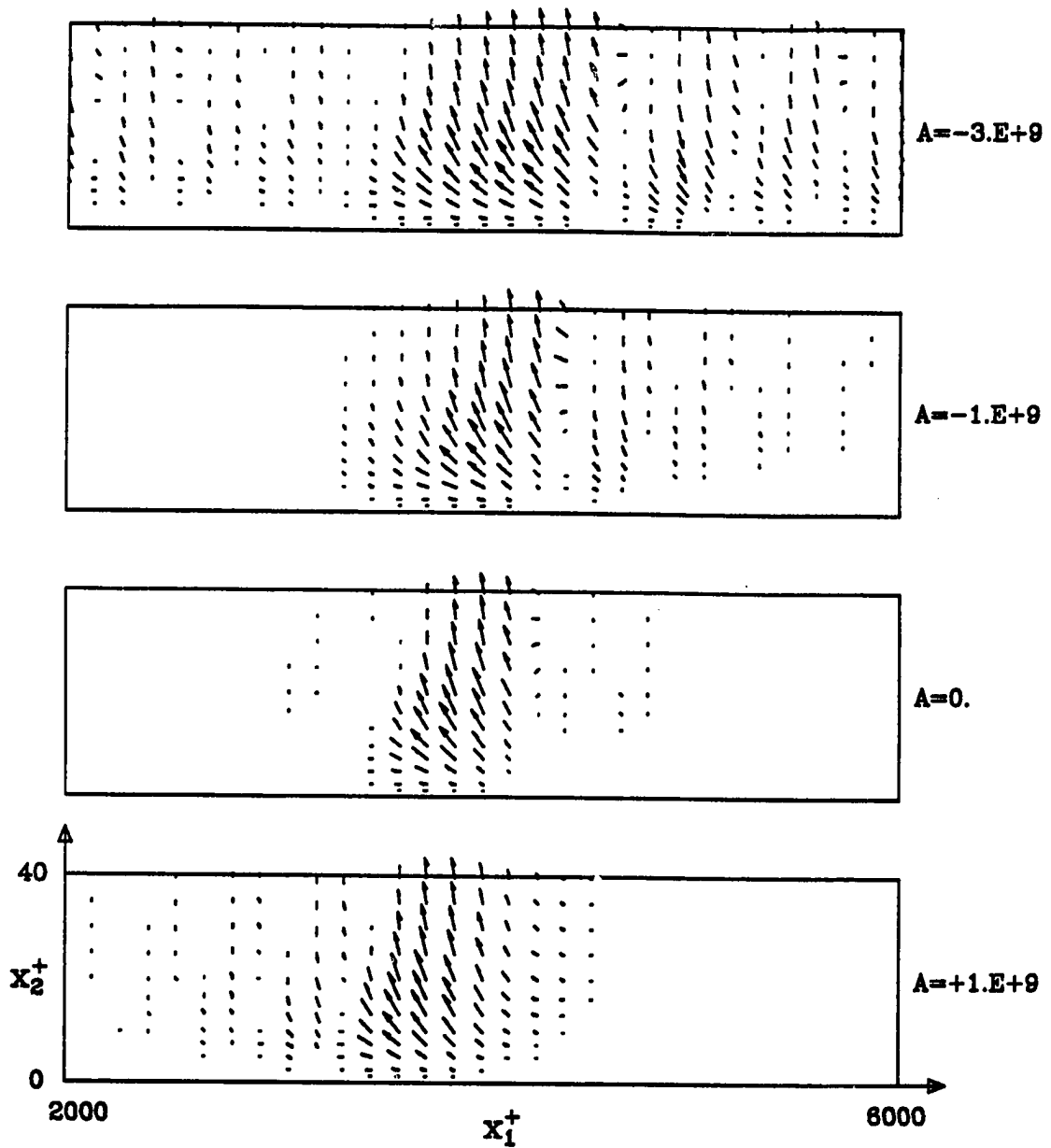
$x_1^+=$ streamwise coordinate.

$x_2^+=$ wall−normal coordinate.

Figure 48: Variation of velocity field of typical eddy in
in plane of symmetry with changes in phase—
shift as indicated by parameter A next
to each graph. A=0.= zero phase—shift.
Δx_l^+=4000= period of the lowest non—zero
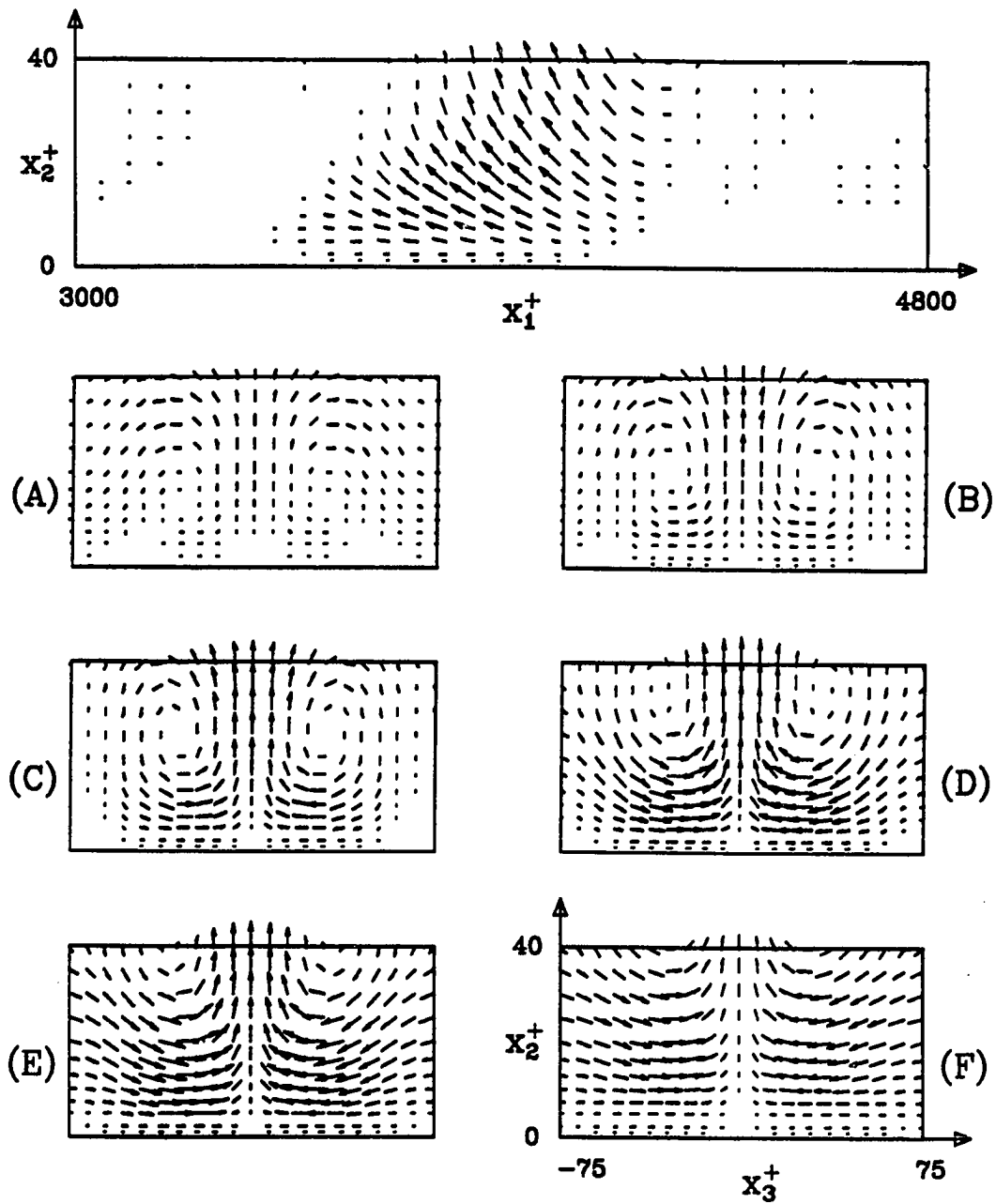streamwise wave—number.

Figure 49: Velocity field of typical eddy (zero phase—shift) in symmetry plane and various cross—sectional cuts, looking downstream. Values of their downstream position x_1^+ :

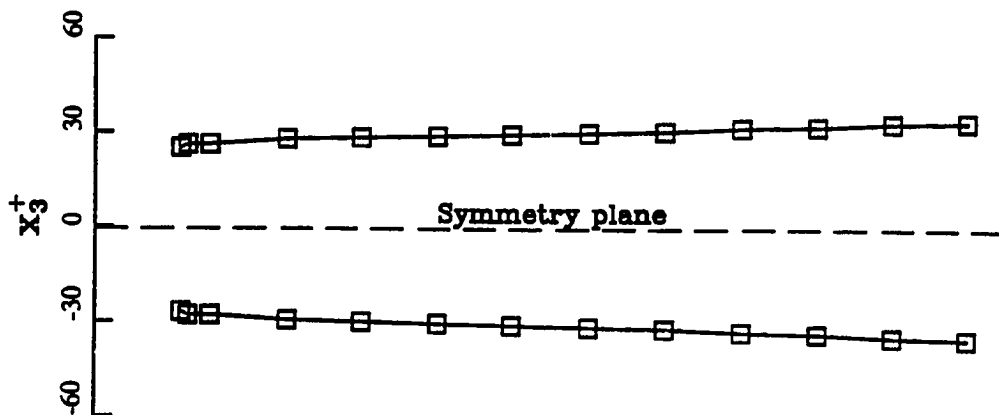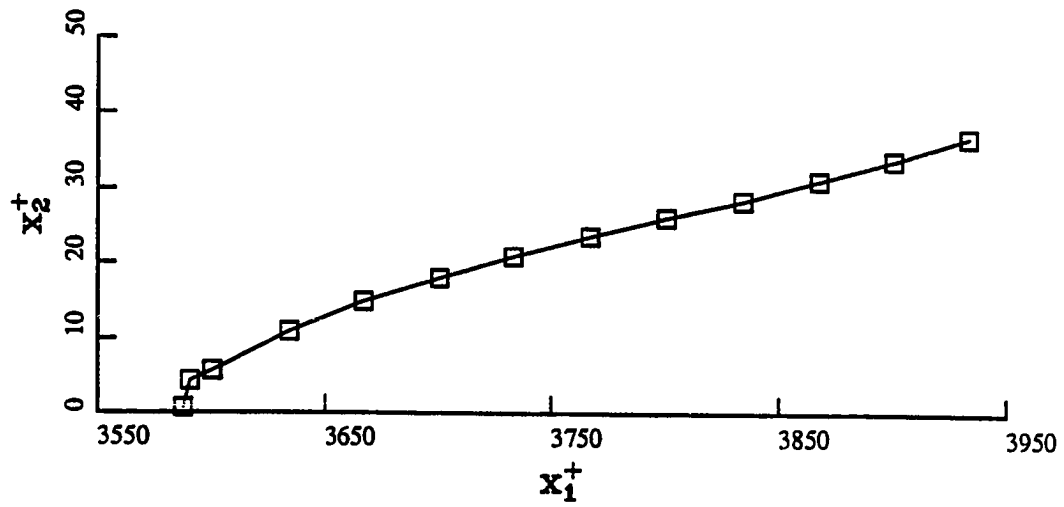|					
(A)	3660	(B)	3720	(C)	3780
(D)	3900	(E)	4020	(F)	4140

Figure 50: Centerline $(F_2=F_3=0)$ of typical eddy in side and top view.
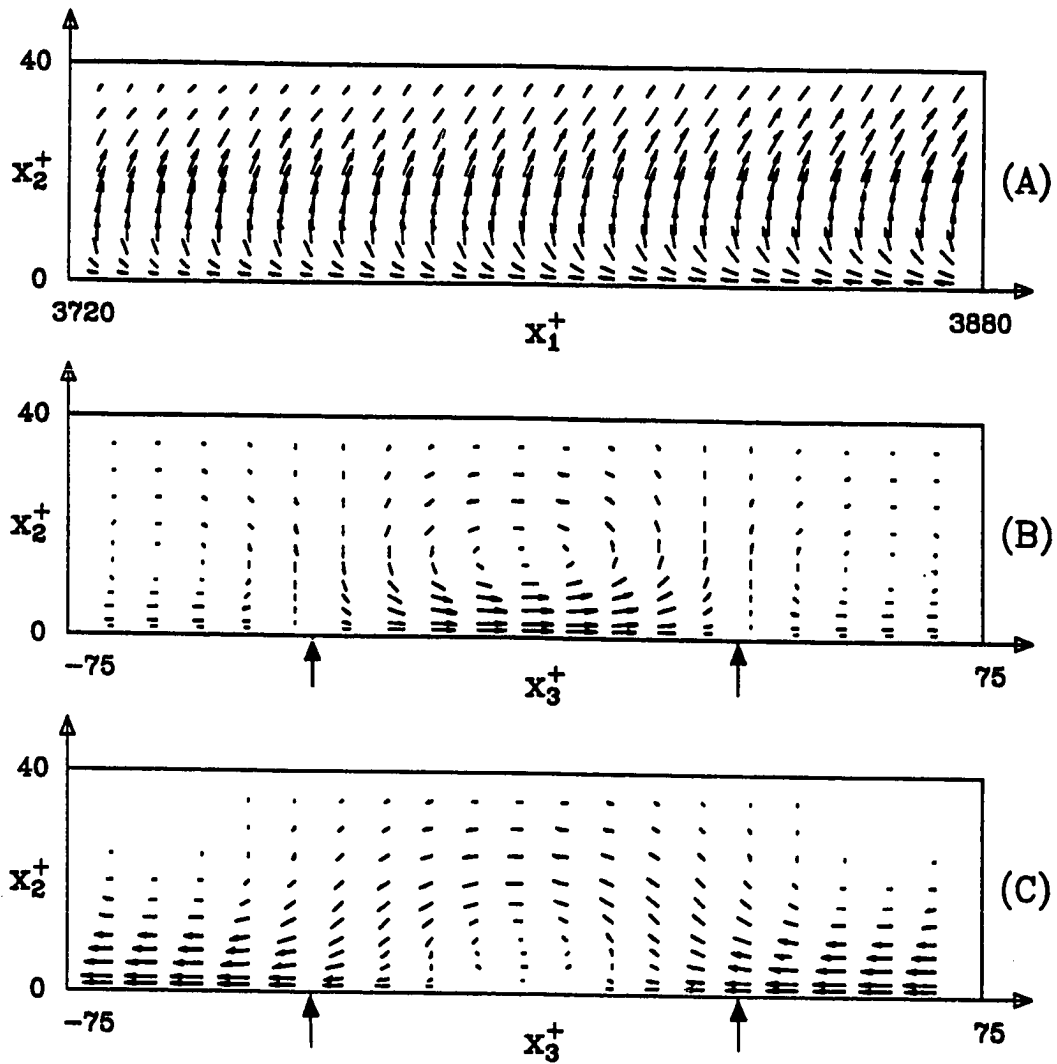
Figure 51: Vorticity field of typical eddy .

(A) Side view in plane of center—line, x_3^+=30.0
Maximum vortex stretching by mean—velocity occurs for x_2^+>15.

(B) Cross—sectional view, x_1^+= 3800
In the symmetry plane between the 2 rolls (x_3^+=0) the streamwise and wall—normal vorticity are zero (no vortex stretching).
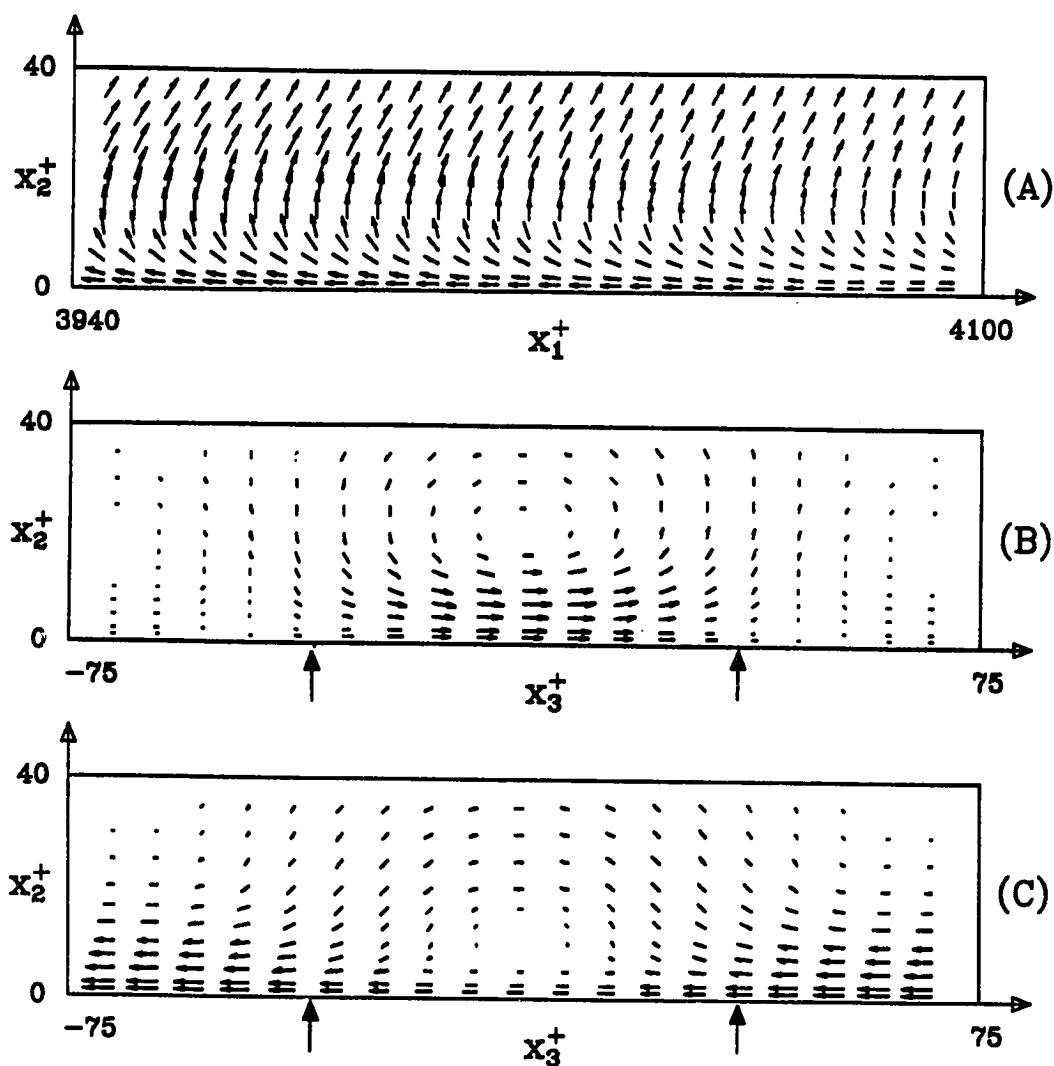
(C) Same as (B) with vorticity of mean—velocity added.

Figure 52: Vorticity field of typical eddy .

(A) Side view in plane of center-line, x_3^+=30.0
Maximum vortex stretching by mean-velocity occurs for x_2^+>20.

(B) Cross-sectional view, x_1^+= 4020
In the symmetry plane between the 2 rolls (x_3^+=0) the streamwise and wall-normal vorticity are zero (no vortex stretching).

(C) Same as (B) with vorticity of mean-velocity added.

Appendix

PROGRAMS AND CONVENTIONS

In order to facilitate future usage of the measured and analyzed data we would like to give a short overview of available magnetic tapes, programs and of conventions used during the analysis of the data.

Data files which contain a time series of voltage or velocity signals or spectra have as part of their file name a unique 4-digit number referred to as run number. This run number designates a particular experiment with the probes located at specified positions inside the tunnel. File PROB POSM contains the association between run number and positions of the probes; you may look into this file with the editor or use program SEARCH. This program explains also how to decipher the position code in file PROB POSM.

The original voltage time series of the hot-film anemometer (digitized at 2000 Hz) are available on magnetic tapes called ZIGxxx, with xxx being a three digit number from 000 to 116. The data are organized in files, one for each of all the assumed probe positions in the tunnel. These data can be transferred to disk by program A2 on a file by file basis. During the transfer a quality analysis is performed and individual parts of a file can be excluded from transfer. In addition we used this program to low-pass filter and compress the data (skipping time-steps).

-157-

A program called RAT transfers these data to tapes called RATxx (xx=00,02...48). Individual segments of poor data quality could be excluded from transfer and simple statistics of the resulting voltage time series were calculated.

These statistics were incorporated by program A5 to convert the voltage time series into velocity (m/sec) signals which are directly analyzed. The resulting spectra were written first to disk and then transferred to magnetic tapes. All cross-spectra can be found on the tapes A5S12A and A5S12C and spectra pertaining to each probe individually on the tapes A5SPA and A5SPB. The spectra of these four tapes can be transferred back to disk by the utility program TC on a file by file basis or directly accessed by an arbitrary program using the tape-handler package TH2.

An example for this is the program TZ1 which we used to perform the inverse Fourier-transform (subroutine CF) to obtain from the spectra the correlation tensor at zero time lag. Subroutine CF performs the operation:

$$R(m*\Delta\tau) = \sum_{-N}^{+N} S(n*\Delta f) \ \exp(+2\pi imn/N) \ * \ \Delta f$$

with $\Delta\tau = 1./(N*\Delta f)$

S(f) is here the 2-sided cross-spectrum (complex-valued) given in the spectral files as function of the cyclic frequency for f=n*Δf, n=0,N. Subroutine CF evaluates the correlation function R(τ) for τ=m*Δτ, m=-N,+N. The physical units of the correlation function are (m/sec)^2.

The values of the cross-correlation tensor at zero time lag (only those components based on the two wall-parallel velocity components) as calculated by program TZ1 are stored in file TZ1 DAT.

This data file can be read by program TZ2 which normalizes the correlation function by the friction velocity and determines the coefficients of a curve fit for the correlation tensor at fixed wall-distance of each of the two probes. See chapter 5.2 for the precise functional form describing each component of the correlation tensor as function of the streamwise and spanwise spacing. Note how in

$$R_{ij}(x_2 \; x_2' \; x_1\text{-}x_1' \; x_3\text{-}x_3') = \langle u_i(x_1 \; x_2 \; x_3) \; u_j(x_1' \; x_2' \; x_3') \rangle$$

the subscripts i and j and the arguments of the correlation tensor relate to the velocities measured with the probe at location (x_1, x_2, x_3) and (x_1', x_2', x_3'). All spatial coordinates are measured and used in all subsequent calculations in wall units in a right-handed coordinate system with x_1 pointing downstream and x_2 away from the wall. The unprimed location referred to the upstream and the primed to the downstream probe during evaluation of the measured data which were in above notation conducted at negative streamwise and lateral spacings. General symmetry principles allow then extension to positive spacings.

The coeffients of the various curve fits were written into file TZ2 DAT.

Program TZ3 reads this file entirely in order to solve the eigenvalue problem. The curve fits to the various components of the

correlation tensor are functions of which the double Fourier-transform with respect to the streamwise and spanwise spacing, defined in equation (4.11), could be taken analytically in general form. This resulted in functions for the spectral tensor with a set of coefficients related to the set of coefficients describing the correlation tensor. Program TZ3 evaluates these coefficients accordingly and then enters a loop at the top of which the user is asked to enter the values of the streamwise and spanwise wave-number at which he wants to solve the eigenvalue problem. TZ3 determines first the missing components of the correlation tensor using the incompressibility condition, equation (4.39). Differentiation is here approximated by that finite differencing which is exactly the inverse operation to the numerical integration scheme employed, see equation (4.36) and (4.37). Integration with respect to x_2^+, which is needed for solving the eigenvalue problem, equation (4.34), is performed using the trapezoidal method. Such a scheme is internally consistent in that the resulting eigenfunctions automatically satisfy the normalization condition, equation (4.13), if that integral is again evaluated by means of the trapezoidal integration method. Program TZ3 finally checks the bilinear representation of the spectral tensor, equation (4.14), before it prompts the user for another pair of streamwise and spanwise wave-number. The resulting eigenvalues and functions are written into files by TZ3. Solutions have been calculated for wide range of wave-numbers and are stored in file PHIEX DAT.
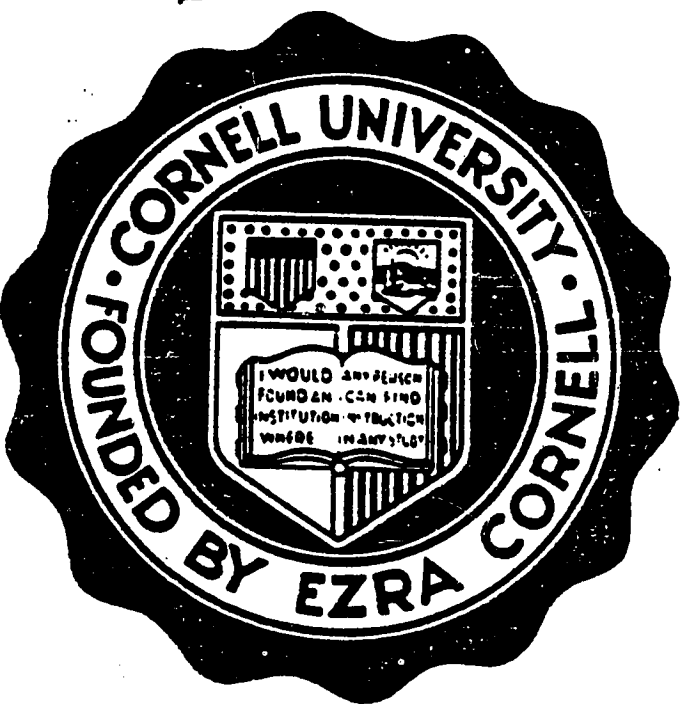
A variety of programs are available for plotting

a) the eigenvalues (LAMD3)

b) the velocity field of an individual composite

   Fourier-mode of the dominant eigenmode (TZ7)

c) the velocity field of the dominant eigenmode

   integrated in streamwise direction (TZ4)

d) the velocity and vorticity field of the typical eddy

   with specified phase-shift (TZ6).

All these programs use the subroutine GET to obtain the

eigenfunctions etc. from file PHIEX DAT.

END